JGR Space Physics

RESEARCH ARTICLE
10.1029/2019JA026800

Magnetic Field Observations on Cassini's Proximal Periapsis Passes: Planetary Period Oscillations and Mean Residual Fields

G. Provan[1], S. W. H. Cowley[1], T. J. Bradley[1], E. J. Bunce[1], G. J. Hunt[2], H. Cao[2,3,4], and M. K. Dougherty[2]

[1]Department of Physics and Astronomy, University of Leicester, Leicester, UK, [2]Blackett Laboratory, Imperial College London, London, UK, [3]Department of Earth and Planetary Science, Harvard University, Cambridge, MA, USA, [4]Division of Geological and Planetary Sciences, California Institute of Technology, California, USA

Key Points:
- We study magnetic data from Cassini proximal periapsis passes at Saturn to investigate planetary period oscillations (PPOs) and mean fields
- Dual north and south system PPO modulations are present from auroral to ring region field lines, with earlier phases in the inner region
- Outside of D ring field lines, mean azimuthal fields ~3–5 nT are "lagging" in form, continuous across ring and subauroral field lines

Correspondence to:
G. Provan,
gp31@le.ac.uk

Citation:
Provan, G., Cowley, S. W. H., Bradley, T. J., Bunce, E. J., Hunt, G. J., Cao, H., & Dougherty, M. K. (2019). Magnetic field observations on Cassini's proximal periapsis passes: Planetary period oscillations and mean residual fields. *Journal of Geophysical Research: Space Physics*, *124*, 8814–8864. https://doi.org/10.1029/2019JA026800

Received 3 APR 2019
Accepted 25 SEP 2019
Accepted article online 10 OCT 2019
Published online 19 NOV 2019

Abstract We analyze periapsis pass magnetic field data from the final 23 orbits of the Cassini spacecraft at Saturn, uniquely encompassing auroral, subauroral, ring region, and intra-ring field lines, to determine the planetary period oscillations (PPOs) and mean residual fields in these regions. Dual modulation by northern and southern PPO systems is found almost continuously, demonstrating for the first time the presence of PPOs on and inside ring region field lines. The azimuthal component displays the largest ~10–15nT PPO amplitudes on auroral field lines, falling across the subauroral region to ~3–5 nT on main ring field lines in the northern hemisphere, less in the southern hemisphere, while increasing to ~5–8 nT on D ring and intra-D ring field lines. Auroral and subauroral amplitudes mapped along field lines are in good agreement with previous analyses in regions of overlap. Colatitudinal and radial field oscillations generally have a half and a quarter the amplitude of the azimuthal component, respectively. Inner region oscillation phases are typically several tens of degrees "earlier" than those of outer subauroral and auroral regions. Mean residual poloidal fields (internal and ring current fields subtracted) show quasi-sinusoidal latitude variations of ~2.5nT amplitude, with radial and colatitudinal fields approximately in quadrature. Mean azimuthal fields peaking at ~15 nT are approximately symmetrical about the equator on and inside D ring field lines as previously reported, but are unexpectedly superposed on ~3–5nT "lagging" fields which extend continuously through the ring region onto subauroral field lines north and south.

1. Introduction

A major property of Saturn's magnetosphere which has received significant investigation during the Cassini mission is the modulations observed near Saturn's rotation period throughout the system, despite the perfect axisymmetry of the internal planetary magnetic field to within measurement uncertainty. The most recent analysis of the internal field shows, in particular, that the principal planetary dipole component is aligned with the spin axis to better than ~0.01° (Dougherty et al., 2018). Nevertheless, rotating modulations, termed "planetary period oscillations" (PPOs), have been ubiquitously observed in the magnetospheric magnetic field, plasma properties and structures, energetic ion and electron fluxes, related energetic neutral atom emissions, and plasma waves, together with auroral emissions at ultraviolet, infrared, and radio wavelengths (e.g., Andrews, Cowley, et al., 2010; Andrews et al., 2011; Arridge et al., 2011; Bader et al., 2018, 2019; Badman et al., 2012; Bradley, Cowley, Bunce, et al. (2018); Carbary et al., 2011; Carbary, 2017; Clarke, Andrews, Arridge, et al., 2010; Clarke, Andrews, Coates, et al., 2010; Cowley & Provan, 2017; Espinosa & Dougherty, 2000; Gurnett, Persoon, et al., 2009; Gurnett et al., 2011; Jackman et al., 2016; Lamy, 2011, 2017; Lamy et al., 2013; Nichols, Cecconi, et al., 2010; Nichols, Cowley, et al., 2010; Provan et al., 2012; Ramer et al., 2017; Southwood & Kivelson, 2007; Thomsen et al., 2017; Ye et al., 2010). Analysis of the auroral-related radio emissions, specifically of Saturn kilometric radiation (SKR), was the first to show that two such modulation systems are in fact simultaneously present, one associated with the northern polar hemisphere and the other with the southern polar hemisphere, in general having slightly differing periods (Gurnett, Lecacheux, et al., 2009; Kurth et al., 2008). Studies of these emissions were also the first to show that these periods vary slowly over Saturn's seasons, by up to ~±1% about a mean period of ~10.7 hr (Fischer et al., 2015; Galopeau & Lecacheux, 2000; Gurnett et al., 2010, 2011; Lamy, 2011, 2017; Ye et al., 2016). Overall, the Cassini orbital mission from July 2004 to September 2017 spanned just less than half a

Saturn year from postsolstice southern summer at the start of the mission (southern solstice occurred in October 2002), through vernal equinox in August 2009, and northern summer solstice in May 2017. The properties of the PPOs have also been extensively investigated over this interval using Cassini magnetic field data, as will be discussed further below.

Although much has been learned about the PPO phenomenon over the course of the Cassini mission, a significant gap in knowledge concerns their properties in the inner part of the Saturn system. Specifically, due to spacecraft hazard concerns, no observations were made during the main mission interval on field lines passing through Saturn's ring system, apart from one brief partial crossing during Saturn orbit insertion in July 2004 (Dougherty et al., 2005). On the final 22 full orbits of the Cassini mission during April–September 2017, however, the spacecraft at periapsis was targeted to pass through the narrow radial gap between the denser layers of the upper atmosphere and the inner edge of the innermost D ring at ~1.11 R_S, thus making a rapid ~1-hr pass across almost the full width of Saturn's ring-crossing field lines (Dougherty et al., 2018). (R_S is Saturn's 1-bar equatorial radius equal to 60,268 km.) The central purpose of this paper is thus to examine the magnetic field data from these passes for the presence of PPO field oscillations on and inside ring-crossing field lines. However, the same analysis also provides profiles of the mean residual fields (planetary, ring current, and PPO contributions removed) along these proximal periapsis trajectories. Here we show that PPO fields are indeed present on ring-crossing field lines, and we compare their properties, together with those of the residual fields, with those determined from previous analyses of fields observed on polar, auroral, and adjacent subauroral field lines. We thus begin by outlining in the following introductory subsections the results of previous analyses as they relate to the present study, thus also forming relevant background to our analysis methodology.

1.1. Determination of PPO Amplitudes, Phases, and Periods From Magnetic Field Data

We first discuss the determination of the amplitudes, phases, and periods of the two PPO systems from magnetic field data, this information forming an essential input to the study. These determinations have usually involved the selection of approximately one- to two-day intervals of "quiet" magnetospheric magnetic field data, either in the near-equatorial quasi-dipolar magnetosphere or in the polar region depending on spacecraft orbit properties, that are devoid of significant non-PPO ~10-hr field variations (due, e.g., to crossings of the ring current region or plasma sheet), and fitting rotating sinusoidal functions to each of the three field components to determine the amplitude and phase of the ~3–5 cycles of the field oscillation thereby observed (e.g., Andrews et al., 2008; Andrews, Coates, et al., 2010; Provan et al., 2009). Orbit-to-orbit analysis of the variations in phase, which are in general beat-modulated due to the simultaneous presence of the two PPO systems, then yields the phases versus time and hence periods of both northern and southern PPO systems (Andrews et al., 2012; Provan et al., 2011, 2013). The amplitudes of the two systems can then be determined from fits to the beat-modulated amplitude data.

Using these techniques, the properties of the two PPO systems have been determined from magnetic field data near-continuously throughout the Cassini mission (Andrews et al., 2012; Provan et al., 2013, 2016, 2018), with the exception of a few short (few-month) intervals when the properties of one or other system could not be discerned due to too low amplitude. The results show that the southern system was dominant during southern summer (factor of ~2.5 in amplitude) at the beginning of the Cassini mission, with the southern period ~10.8 hr longer than the northern ~10.6 hr. A complex, approximately five (Earth) year, interval of variable amplitudes and near-coalesced periods then occurred which spanned and followed equinox. Subsequently, the northern system became variably dominant during northern summer at the end of mission (amplitude factors of ~1.5 to >5), with the northern period ~10.8 hr longer than the southern ~10.7 hr. The results presented in this paper relate to the PPO properties in the latter interval, during the final approximately five months of the Cassini mission, for which the phases and periods were determined by Provan et al. (2018) from near-apoapsis nightside data on the same orbits for which the dayside periapsis pass data are analyzed here. These data also suggest a relatively modest north/south amplitude ratio of ~1.4 during this interval.

We note that overall comparison of the magnetic field results with those derived using SKR data cited above has generally shown good agreement (Andrews, Coates, et al., 2010; Andrews et al., 2012; Provan et al., 2014, 2016), though with a few intervals of discrepancy, particularly during the post-equinox interval of highly variable properties, that are attributable to limitations in interpretation of one or other data set (e.g.,

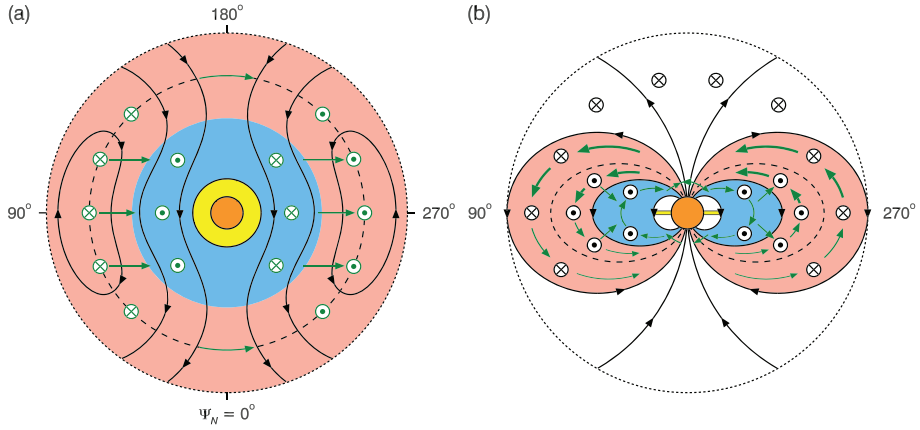

Figure 1. Sketches showing the form of the PPO-related perturbation fields and currents, specifically for the northern PPO system. Figure 1a shows a view looking down onto Saturn's equatorial plane from the north, where the solid orange circle represents the body of the planet and the yellow area the surrounding ring region. The outer black dotted circle represents the magnetopause on the dayside and the inner boundary of the tail region on the nightside. The PPO-related perturbation field lines projected onto the equatorial plane in this region are shown by the arrowed black lines, together with the phase or longitude system Ψ_N used to describe azimuthal position relative to the system. The outer red shaded area indicates the region of principal PPO-related field-aligned current flow extending in to ~10 R_S in the equatorial plane, containing the radius at ~15–20 R_S where the azimuthal perturbation field changes sign, shown by the dashed circle. The inner blue shaded area indicates the region of return field-aligned current flow. The current direction is indicated by the green symbols, where circled dots indicate northward directed field-aligned current flowing out of the plane of the diagram, circled crosses indicate southward directed field-aligned current flowing into the plane of the diagram, and green arrows represent cross-field currents flowing in the magnetospheric plasma. Figure 1b shows the perturbation fields and currents in the $\Psi_N = 90° - 270°$ meridian plane, where the arrowed black lines are field lines of the background magnetospheric field. The colored areas and dashed field lines correspond to Figure 1a. The perturbation fields are indicated by the black circled dots and crosses, where the circled dots indicate the quasi-uniform perturbation field pointing out of the plane of the diagram in the inner part of the system, while the circled crosses indicate the quasi-dipolar closure field pointing into the plane of the diagram in the outer part of the system extending over the north polar region. The field-aligned and field-perpendicular current flows are indicated by the green arrows.

Cowley & Provan, 2015, 2016; Provan et al., 2016). However, such differences do not complicate discussion of the PPO data during northern summer employed here, for which the magnetic field and SKR phases and periods have been shown to be in excellent agreement (Provan, Lamy, et al., 2019).

1.2. Overall Structure of the PPO Perturbation Fields and Currents

The second aspect of PPO-related magnetic field studies concerns the large-scale structure of the perturbation field, and hence of the associated electric currents. The nature of such studies clearly depends on the spacecraft orbit, whether near-equatorial or highly inclined, and the spatial regimes consequently traversed. During the Cassini mission four extended intervals of near-equatorial orbits were undertaken, beginning after orbit insertion in 2004. Data from the first two of these, in 2004–2006 and 2007, were employed to study the equatorial structure of the then-dominant southern PPO field and the north-south currents flowing through it (Andrews, Cowley, et al., 2010). These near-equatorial intervals were interspersed with four extended intervals of highly inclined orbits culminating in the F ring and proximal orbits of the Cassini Grand Finale in 2016–2017. Data from the earlier of these highly inclined orbit intervals have been employed to investigate the variation of the PPO fields in the meridian plane, in particular the structure of the PPO-related field-aligned currents that couple the planetary ionosphere and magnetosphere, using data from periapsis passes at sufficiently small, typically few R_S, radial distances (Bradley, Cowley, Provan, et al., 2018; Hunt et al., 2014, 2015, 2016; Hunt, Provan, Bunce, et al., 2018; Hunt, Provan, Cowley, et al., 2018).

These studies have shown that the basic form of the PPO perturbation field and currents is as sketched in Figure 1, specifically for the northern PPO system. Figure 1a shows a sketch of the perturbation field (arrowed black lines) and current (green symbols and arrows) in Saturn's equatorial plane in a view looking down from the north along Saturn's spin/magnetic axis. The figure also indicates the azimuthal PPO phase or longitude parameter, Ψ_N, that is used throughout this paper to define azimuthal position with respect to

this system. As the northern PPO system rotates in the sense of planetary rotation at its individual period, Ψ_N increases with time at a fixed position, by 360° for a full turn. In the inner region, the perturbation field consists of a quasi-uniform field in the equatorial plane that (by definition of the phase system) points directly radially outward at $\Psi_N = 0°/360°$ and directly radially inward at $\Psi_N = 180°$, such that to a first approximation the radial component varies as $\sim\cos\Psi_N$. The azimuthal component, positive in the sense of planetary rotation, then varies in lagging quadrature as $\sim\sin\Psi_N$. However, beyond a certain radial distance indicated by the black dashed circle the azimuthal component reverses sign to vary in leading quadrature as $\sim -\sin\Psi_N$ such that in the outer region the field becomes quasi-dipolar in form. The dipole in question is directed along the $\Psi_N = 0°$ meridian transverse to the planetary spin axis. A colatitudinal perturbation field of comparable magnitude (on the order of ~1 nT) is also present, which for the northern system has the opposite sign to the radial component, thus varying as $\sim -\cos\Psi_N$. The quasi-uniform perturbation fields are thus bent into arches with apices in the south, with field continuity maintained by closure out of the plane of the diagram in the northern polar region. With regard to spatial scales, observations show that the reversal in sense of the azimuthal field occurs in the outer part of the magnetosphere at equatorial radial distances of ~15–20 R_S (Andrews, Cowley, et al., 2010). The outer dotted line in Figure 1a lying at a radial distance typically ~5–10 R_S beyond this corresponds schematically to the magnetopause on the dayside and the inner boundary of the magnetic tail region on the nightside. The central orange circle in Figure 1a then corresponds to the body of the planet, and the yellow surrounding region to the main planetary ring system, extending to ~2.3 R_S in the equatorial plane.

For the southern system the southern PPO phase parameter, Ψ_S, is defined similarly with respect to the orientation of its equatorial perturbation field, such that the radial component also varies as $\sim\cos\Psi_S$, while the azimuthal component varies as $\sim\sin\Psi_S$ in the inner quasi-uniform field region and as $\sim -\sin\Psi_S$ in the outer quasi-dipolar field region. Opposite to the northern system, however, the colatitudinal component varies as $\sim\cos\Psi_S$ in phase with the radial component, such that the field lines are bent into arches with apices in the north, closing in the southern polar region.

The principal currents of the PPO system flow along outer closed magnetospheric field lines in the red shaded region in Figure 1a, directed southward into the plane of the diagram on the left peaking at $\Psi_N = 90°$ (green circled crosses), and northward out of the plane of the diagram on the right peaking at $\Psi_N = 270°$ (green circled dots). These currents are associated with the reversal in sense of the azimuthal field in the outer part of the system across the black dashed circle at ~15–20 R_S, and continue inside to a radial distance of ~10 R_S (e.g., Bradley, Cowley, Provan, et al., 2018; Hunt et al., 2015; Hunt, Provan, Bunce, et al., 2018). The total field-aligned current flowing through the equatorial plane in this region on either side of the $\Psi_N = 0°–180°$ meridian is ~2.5 MA. Inside this in the blue shaded region, however, the field-aligned current flow reverses sense, to northward on the left peaking at $\Psi_N = 90°$, and to southward on the right peaking at $\Psi_N = 270°$, such that (in the presence of weaker radial field variations) the azimuthal field falls with radial distance less rapidly than $\sim 1/r$. This region typically carries a slightly smaller field-aligned current of ~2 MA, with the remaining current closing cross-meridian in the outer magnetosphere as indicated by the outer green arrows. For the southern system the field-aligned currents have the same sense with respect to Ψ_S as for the northern system with respect to Ψ_N, but with reversed directions of the cross-field currents shown by the green arrows.

Figure 1b shows a sketch of the northern PPO system in the $\Psi_N = 90°–270°$ meridian plane, with Saturn's spin/magnetic axis directed upward. The field-aligned boundaries of the red and blue shaded regions and the black dashed line follow Figure 1a, while the arrowed solid black lines indicate background magnetospheric field lines, near-axisymmetric in the inner region. The black circled dots indicate the quasi-uniform PPO perturbation field lying inside of the black dashed field line, while the black circled crosses indicate the quasi-dipolar closure field lying outside the black dashed line and extending principally over the pole in the northern hemisphere (over the pole in the southern hemisphere for the southern PPO system). The principal PPO-related currents in the outer red shaded part of the system shown by the green arrows flow southward along the field at $\Psi_N = 90°$ on the left and northward along the field at $\Psi_N = 270°$ on the right. The currents map into the ionosphere in layers ~4°–5° latitude wide just equatorward of the open-closed field line boundary (OCB). Across this current layer the PPO-related azimuthal field reverses sense from its polar value to reach peak values on closed field lines at its lower

latitude border (Bradley, Cowley, Provan, et al., 2018; Hunt et al., 2014, 2015). On the nightside, the OCB is typically conjugately located at ~13.5° colatitude in the northern hemisphere and ~15° colatitude in the southern hemisphere (Jinks et al., 2014), such that the peak PPO-related azimuthal field and reversal in field-aligned current is located at ~18° in the northern hemisphere and at ~20° in the southern, mapping near ~10 R_S in the equatorial plane as indicated in Figure 1. The north-south asymmetry in conjugate points is due principally to the axial quadrupole term of the internal planetary field (Burton et al., 2010; Dougherty et al., 2018). On the dayside the boundaries are located a degree or two closer to the spin/magnetic poles (e.g., Bader et al., 2019), due to the day-night magnetospheric asymmetry associated with the solar wind flow.

1.3. Mean Azimuthal Fields

Although the PPOs are a principal focus of this study, as mentioned above our analysis also yields profiles of the mean residual fields, after subtraction of the internal field due to the planet and magnetospheric ring current effects. These have also been intensively investigated in the above-cited studies of high-latitude magnetic fields, particularly for the azimuthal component related to angular momentum exchange between the atmosphere-ionosphere and magnetosphere (e.g., Bradley, Cowley, Provan, et al., 2018; Hunt et al., 2014, 2015; Hunt, Provan, Bunce, et al., 2018; Hunt, Provan, Cowley, et al., 2018). These studies have shown that the azimuthal fields are generally "lagging" in form associated with outward transfer of planetary angular momentum, with negative values in the northern hemisphere and positive values in the southern hemisphere. On open field lines the azimuthal field increases in magnitude with distance from the pole, associated with distributed downward directed field-aligned currents which are broadly spread in the summer hemisphere but confined to the region poleward of the OCB in the winter hemisphere (Bradley, Cowley, Provan, et al., 2018). The associated equatorward directed ionospheric current, integrated in azimuth around the pole, peaks at a seasonally independent value of ~6 MA just equatorward of the OCB, before the azimuthal field and current fall across a layer ~3°–4° wide to smaller values. This layer thus corresponds to a sheet of upward directed field-aligned current located on outer magnetospheric closed field lines, which is associated with Saturn's auroral region (Bunce et al., 2008). This current sheet is essentially co-located with the main PPO field-aligned current (red region in Figure 1), and is of comparable magnitude. The main PPO-related field-aligned current is thus also collocated with Saturn's auroral oval, and significantly modulates both the total current and the auroral intensity (e.g., Bader et al., 2018).

In the subauroral region equatorward of the auroral region, however, somewhat divergent results have been reported in the above studies. In their investigation of highly inclined passes through the nightside magnetosphere, Hunt et al. (2015) found evidence for "leading" mean fields, oppositely directed to those in the polar and auroral regions, but a factor of ~10 weaker in magnitude. Contrarily, in their study of the dayside subauroral fields on the F ring orbits, occurring immediately prior to the proximal orbits studied here, Hunt, Provan, Cowley, et al. (2018) found the consistent presence of weak lagging fields persisting to periapsis near the outer edge of Saturn's ring region.

1.4. PPOs and Mean Fields on Ring Region Field Lines

As indicated above, a significant present gap in knowledge thus concerns the magnetic field properties on ring-crossing field lines in the inner part of the magnetosphere. The outer boundary of these field lines maps to ~35° colatitude in the northern hemisphere (with respect to the northern pole), and to ~39° in the southern hemisphere (with respect to the southern pole). It has thus remained unknown whether PPO field perturbations exist within this region, mapping to much of the middle- and low-latitude ionosphere, or whether it might be shielded, that is, by field-aligned currents flowing on or near its outer boundary. The form of any mean azimuthal field also remains unknown, for example, whether the weak lagging fields reported in dayside subauroral data by Hunt, Provan, Cowley, et al. (2018) persist on dayside ring field region lines, and if so, how they may interface with the azimuthal fields of the innermost interhemispheric current system associated with D ring field lines reported by Dougherty et al. (2018) and Khurana et al. (2018). We also note that on the basis of Cassini orbit insertion wave data, Xin et al. (2006) suggested the presence of currents and related azimuthal perturbation fields on ring field lines associated specifically with an ionosphere-ring system interaction. The suggested interaction would produce lagging azimuthal fields in the outer part of the ring system where the Kepler orbit speed is less than the near-planetary rotation speed of the plasma, but

would reverse sense to leading azimuthal fields inside of Saturn synchronous orbit where the Kepler speed exceeds the plasma rotation speed. Synchronous orbit lies at equatorial radial distances of ~1.86 R_S, within Saturn's B ring.

With regard to ring region phenomena, however, it has been reported that two types of disturbances in Saturn's rings exhibit periodicities which appear to be related to the PPOs. First, it has been found by Porco and Danielson (1982) and Mitchell et al. (2013) that the occurrence of ring "spokes" appearing in the B ring near synchronous orbit is modulated at periods comparable with the PPO periods. Second, Hedman et al. (2009) and Chancia et al. (2019) have reported the presence of patterns in the tenuous material in Saturn's D ring and Roche division (between the A ring and the outer F ring) which rotate with periods near the concurrent dominant PPO period. Both phenomena are thus indicative of the action of a similarly rotating electromagnetic force acting on charged dust grains within the ring system. We also note that PPO oscillation amplitudes at significant fractions of peak values remain in the innermost radial bins centered at 4.5 R_S (spanning 3–6 R_S) in the analysis of near-equatorial field data presented by Andrews, Cowley, et al. (2010), though the spatial resolution in this study was somewhat limited in both radial distance and local time (LT). Similarly, significant azimuthal PPO amplitudes remain at the innermost limits of the data available from the intervals of highly inclined orbits analyzed by Hunt et al. (2015, 2016) and Bradley, Cowley, Provan, et al. (2018), which penetrated to equatorial distances of ~4 and ~7 R_S, respectively, allowing study on field lines mapping in the ionosphere to ~25° and ~20° colatitude in the northern hemisphere, and ~28° and ~22° colatitude in the southern, respectively. The analysis presented in this paper thus uniquely extends these prior studies of PPO-related and mean residual fields to inside of the region of ring-crossing field lines.

2. Cassini Proximal Trajectories and Data Analysis Intervals

We begin by discussing the properties of the spacecraft trajectory during the proximal periapsis passes, which are critical to the nature of the data set and analysis procedures. The Cassini proximal orbits (April–September 2017) comprise the final set of 23 very similar ~6.5day period spacecraft revolutions (Revs) 271–293 (defined from apoapsis to apoapsis), the last of which was partial due to entry into Saturn's atmosphere just prior to periapsis on Rev 293. During this interval the orbit was inclined at ~62° to the planet's equator, with apoapsis slightly north of the equator in the midnight sector at ~21 R_S (near to Titan's orbit), and periapsis slightly south of the equator in the noon sector, targeted such that the spacecraft passed inside the inner boundary of Saturn's innermost D ring and above the denser upper atmosphere (prior to Rev 293). Specifically, on Revs 271–292 the radial distance of periapsis varied between ~1.065 and ~1.027 R_S (Dougherty et al., 2018), corresponding to altitudes between ~3,890 km (Rev 276) and ~1,630 km (Rev 290) above the planetary 1-bar spheroid (essentially the visible cloud surface). These values compare with the radius of the D ring inner boundary at 1.110 R_S corresponding to ~6,650 km above 1 bar, and, for example, the equatorial radius of the main Pedersen conducting layer of Saturn's atmosphere at ~1.017 R_S corresponding to ~1,000 km above 1 bar (Galand et al., 2011).

2.1. Trajectories in the Meridian Plane

Figure 2 shows the first and last of the full proximal passes, Revs 271 (blue) and 292 (red), projected into a meridian plane in cylindrical (ρ, z) coordinates, where ρ is perpendicular distance from the planet's spin/magnetic axis and z is perpendicular distance from the planet's equatorial plane positive northward. Here the outer boundary of the planet (orange) corresponds to the ionospheric Pedersen conducting layer 1,000 km above 1 bar, this layer thus having equatorial and polar radii of 61,268 and 55,364 km, respectively. The arrowed black lines show field lines of the axisymmetric model field employed in this study, corresponding to the principal first three terms of the Dougherty et al. (2018) internal field model (axial dipole, quadrupole, and octupole), plus the axisymmetric Bunce et al. (2007) ring current model for a typical subsolar magnetopause radius of 22 R_S. This model is employed throughout to map between the ionosphere north and south, the spacecraft, and the equatorial plane. Specifically, the field lines shown are mapped at intervals of 5° from the northern pole between 0° (the spin axis) and 30° colatitude, the latter mapping to ~3.0 R_S at the equator, together with their conjugate southern counterparts. The field-aligned purple regions north and south indicate the conjugate locations of the auroral region currents, specifically the main layers of field-aligned current flow associated with the PPOs (the red-colored regions in Figure 1). Across these layers the

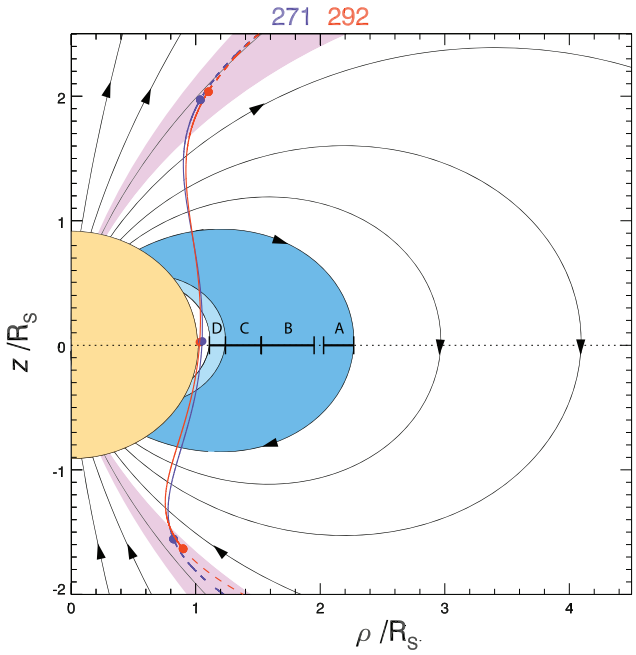

Figure 2. Plot of the periapsis pass trajectories of the initial and final proximal orbits, Revs 271 (blue) and 292 (red), projected into a meridian plane in cylindrical coordinates. Coordinate ρ is the perpendicular distance from Saturn's spin/magnetic axis, while z is perpendicular distance from Saturn's equatorial plane, positive northward. The spacecraft is inbound in the northern hemisphere and outbound in the southern. The outer surface of the planet (orange) corresponds to the main ionospheric Pedersen conducting layer 1,000 km above the 1-bar reference spheroid, while the black arrowed lines correspond to model field lines (see text) plotted every 5° colatitude in the northern ionosphere from the northern pole (the z axis) to 30° colatitude, with conjugate field lines at polar latitudes in the south. The darker blue field-aligned area corresponds to field lines mapping through the main ring region in the equatorial plane, between the inner boundary of the C ring and the outer boundary of the A ring, while the lighter blue field-aligned area corresponds to field lines mapping through the D ring. The rings themselves are indicated by the labeled black lines at the equator, with the gap between the A and B rings corresponding to the Cassini Division. The field-aligned purple areas correspond to the magnetically conjugate auroral regions, specifically the layer carrying the principal PPO currents across which the PPO-related azimuthal field reverses sense and reaches maximum magnitude in the ionosphere at its equatorward boundary, taken to lie between mapped northern ionospheric colatitudes of 13.5° (approximately the OCB) and 18°. The solid line segments of the trajectories between the northern and southern solid circles correspond to the data intervals employed in the analysis in the paper, the northern circles to the inbound crossing of the field line mapping to the northern ionosphere at 15.6° colatitude, and the southern circles corresponding to the inner outbound crossing of the field line mapping to the northern ionosphere at 17.0° (conjugately mapping to the southern ionosphere at ~18.8°). Beyond these points north and south the trajectories are shown dashed. The near-equatorial solid circles represent the points where the trajectories reach their maximum mapped ionospheric colatitudes from either pole, with periapsis points (not marked) lying south of the equator.

PPO-related azimuthal field reverses sense from its polar to its equatorial orientation, attaining its maximum magnitude in the ionosphere at the equatorward boundary. In accordance with the discussion in section 1, this layer is taken to lie in the northern ionosphere between northern colatitudes (with respect to the northern pole) of 13.5°, essentially the OCB, and 18° mapping to ~9 R_S in the equatorial plane (e.g., Bradley, Cowley, Provan, et al., 2018; Bradley, Cowley, Bunce, et al., 2018). Conjugately, it lies in the southern ionosphere between southern colatitudes (with respect to the southern pole) of ~14.9° and ~19.9°. Since, as shown in section 2.2 below, the auroral field lines are traversed inbound and outbound near to the dawn and dusk meridians, respectively, and tailward thereof, the "nightside" boundary locations discussed in section 1 have been taken to apply.

The inner field region colored darker blue in Figure 2 corresponds to the region of field lines passing through Saturn's main ring region in the equatorial plane, rings A–C as indicated by the black lines (the gap between the A and B ring corresponds to the dusty Cassini Division), which lie at radial distances between 2.269 and 1.239 R_S. These field lines map in the northern ionosphere between northern colatitudes of ~35.4° and ~57.1°, and in the southern ionosphere between southern colatitudes of ~39.7° and ~64.9°. Again, the pronounced north-south asymmetry is due to the axial quadrupole term in the internal planetary field. The region colored lighter blue corresponds to the field lines threading the D ring, whose inner boundary at 1.110 R_S maps to ~65.4° colatitude in the northern ionosphere and to ~74.5° colatitude in the southern ionosphere. It is within this inner field line region that Dougherty et al. (2018) reported the discovery of a low-latitude current system which generates azimuthal perturbation fields comparable in magnitude to those on auroral field lines, which have subsequently been discussed by Khurana et al. (2018) and Provan, Cowley, et al. (2019).

The superposed trajectories of Revs 271 and 292 in Figure 2 illustrate the close meridional similarity of all the proximal passes, passing inbound toward periapsis on auroral field lines in the northern hemisphere, then crossing the full width of subauroral and ring field lines both north and south, before passing outbound on auroral field lines in the southern hemisphere. The minimum northern ionospheric colatitudes attained on these trajectories were ~14.9° in the northern hemisphere for both Revs, while the minimum southern ionospheric colatitudes in the southern hemisphere were ~17.8° for Rev 271 and ~18.7° for Rev 292. The intervals selected for analysis in this paper correspond to the segments of the trajectories shown by the solid lines terminated by solid circles, beyond which the trajectories are shown by dashed lines. On the inbound passes these points correspond to where the trajectories cross 15.6° mapped northern ionospheric colatitude, ~0.5° inside of the minimum values. On the outbound passes these points correspond to where the trajectories cross ~18.8° mapped southern ionospheric colatitude, again typically ~0.5° inside of the minimum values. More exactly we employ 17.0° mapped northern colatitude as the limiting colatitude on the outbound passes, since mapped northern colatitude is employed throughout to order the data for analysis, as explained in section 4. Outside of these limits, in the dashed line portions, the trajectories become approximately tangent to the field lines, hence not revealing of colatitudinal structure. These mapped colatitude limits have been applied to the data from all the proximal Revs.

The solid circles on the trajectories just north of the equator in Figure 2 show the points where they attain their maximum mapped northern and southern ionospheric colatitudes, which for Rev 271 corresponds to 72.2° in the northern hemisphere and conjugately 82.0° in the southern hemisphere, and for Rev 292 to 75.7° in the northern hemisphere and conjugately 85.7° in the southern hemisphere. For conciseness, we will refer to these points as the "field-parallel" points on the trajectories, where the spacecraft path lies tangent to the model magnetic flux shell in the meridian plane, the additional azimuthal motion of the spacecraft across field lines at this point notwithstanding (see section 2.2). These points will be employed to define zero time on each pass in the multi-Rev magnetic data time series plots presented in section 4.1, in order to approximately align together the data from each pass. The elapsed time on the inbound portion of each pass from minimum colatitude employed in the northern hemisphere to maximum colatitude near the equator is ~91–96 min (90.6 min for Rev 271 and 95.8 min for Rev 292), while the elapsed time on the outbound portion of each pass from maximum colatitude to minimum colatitude employed in the southern hemisphere is ~69–77 min (69.5 min for Rev 271 and 77.0 min for Rev 292). The overall pass intervals involved are thus ~2.8 hr, approximately a quarter of a PPO cycle. The elapsed time on ring field lines on each pass (blue regions in Figure 2 and the region interior thereto) corresponds throughout to ~32 min inbound to the field parallel point and ~31 min outbound, thus an overall interval of just over ~1 hr, which we note corresponds to a small fraction of a PPO cycle.

2.2. Trajectories Mapped to the Ionosphere

To provide an indication of the range of LTs encompassed on these passes, in Figure 3 we again show the trajectories for Revs 271 (blue) and 292 (red), but now mapped along model field lines into the northern and southern ionospheres. Figures 3a and 3b concentrate on the northern and southern polar region mappings, respectively, to 45° colatitude from either pole, while Figures 3c and 3d show the whole of the trajectories mapped into the northern and southern ionospheres in plots extending to the equator. Latitude circles are shown at 10° intervals in all panels, with the view being down from the north, "through" the planet in the case of the southern mappings in Figures 3b and 3d. For purposes of context we also show in Figures 3a and 3b the statistical auroral oval derived from Cassini ultraviolet data by Carbary (2012), where the black circles joined by black lines show the location of maximum auroral power at 1-hr LT intervals, while the black lines on either side show the half-power points. As expected, these areas are essentially conjugate with the purple-colored field lines in Figure 2 showing the main PPO-related current region. The darker blue region in each figure shows the location of field lines mapping to main rings A–C as in Figure 2, while the lighter blue region in Figures 3c and 3d maps along field lines to the D ring.

The spacecraft trajectories in Figure 3 are shown mapped continuously along model field lines into both the northern and southern ionospheres, where the northern inbound segments are those located principally in the prenoon sector, while the southern outbound segments are those located principally in the postnoon sector, as indicated by the arrows. The segments employed in our analysis are again those indicated by the solid lines terminated by the solid circles, which, as indicated in section 2.1, start when the mapped trajectory crosses 15.6° colatitude in the northern ionosphere inbound, and stop when it crosses 17.0° colatitude in the northern ionosphere outbound. The corresponding colatitudes in the southern ionosphere are ~17.3° inbound and ~18.8° outbound. Beyond these points the mapped trajectories are again shown by dashed lines, to spacecraft radial distances of 7 R_S (far beyond the dashed segments in Figure 2).

For Rev 271 the data segment employed starts at ~6.9 hr LT just after dawn and ends at ~18.6 hr LT just after dusk, both in or very close to the statistical UV auroral region, with the field-parallel (maximum colatitude) point being located approximately half way between at ~12.9 hr LT. We note that due to the axisymmetry of the model field, the footprint LTs at a given time are the same in both hemispheres. For Rev 292 the orbit is located at somewhat earlier LTs, such that the data segment employed starts at ~4.9 hr LT before dawn and ends at ~17.9 hr LT just before dusk, with the field-parallel (maximum colatitude) point being located at ~11.2 hr LT. The interval employed from each Rev thus encompasses a very wide range of LTs, ~11.7 hr for Rev 271 and ~13.0 hr for Rev 292, both spanning essentially the whole of the dayside sector. The LT range for which the spacecraft is located on and inside ring-mapping field lines is less extensive, of course, spanning ~3.9 hr between ~11.0 and ~14.9 hr for Rev 271, and ~4.1 hr between ~9.2 and ~13.3 hr for Rev 292.

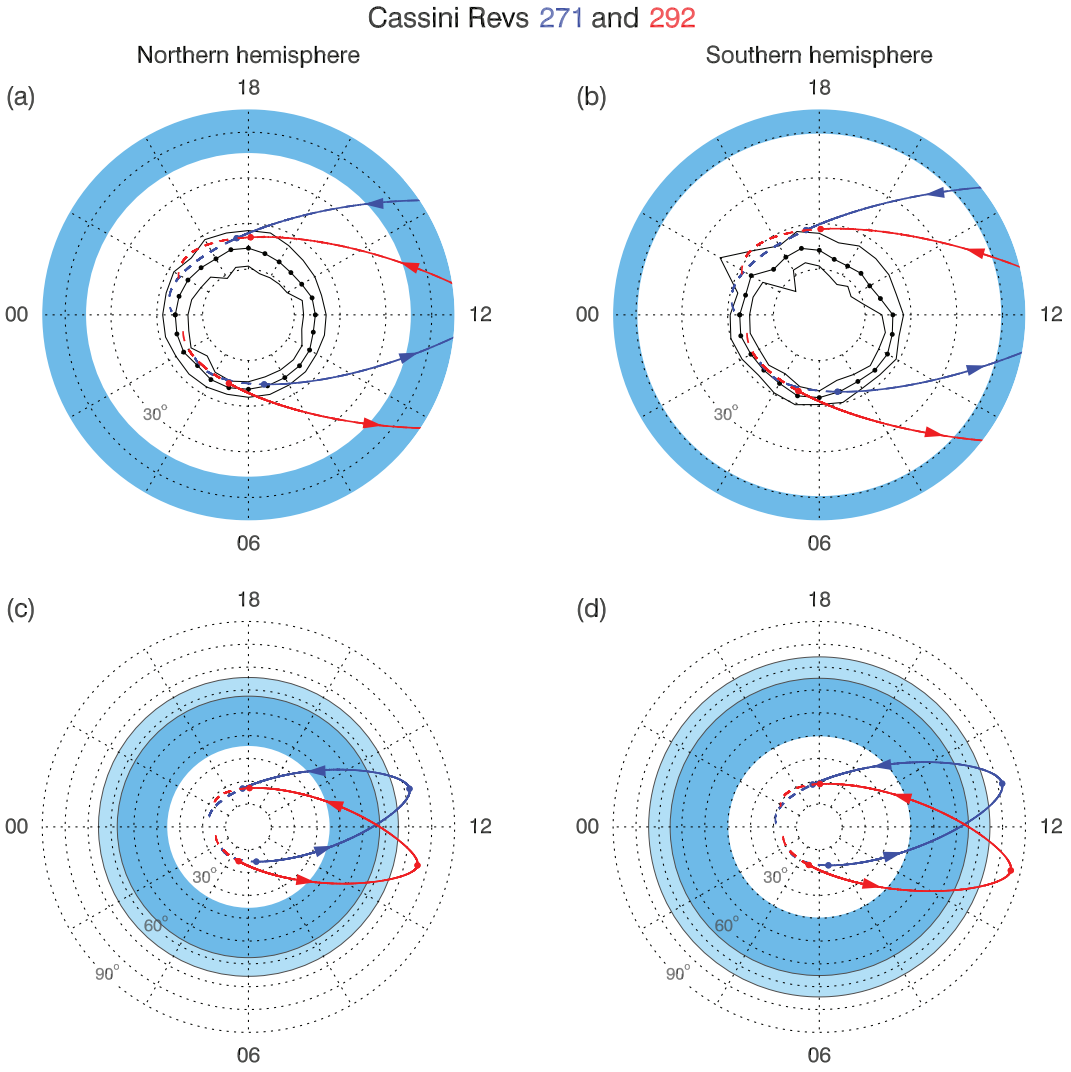

Figure 3. Plots of the trajectories of the initial and final proximal orbits, Revs 271 (blue) and 292 (red), mapped along model field lines (see text) into the northern and southern ionospheres. Figures 3a and 3b show the northern and southern polar mappings, respectively, to 45° colatitude from each pole, while Figures 3c and 3d correspondingly show the whole of the mapped trajectories in plots extending to the equator. In all panels the view is looking down from the north, "through" the planet in the case of the southern hemisphere plots in Figures 3b and 3d, with noon (12 hr LT) on the right and dawn (06 hr LT) at the bottom. Dotted colatitude circles are shown at 10° intervals, while dotted radial lines are plotted at 2-hr intervals of LT. As in Figure 2, the darker blue annular areas correspond to field lines mapping to Saturn's main ring region (rings A–C) in the equatorial plane, while the lighter blue annular areas in Figures 3c and 3d correspond to field lines mapping to the D ring. The black circles joined by black lines in Figures 3a and 3b show the positions of maximum auroral power at 1-hr LT intervals determined by Carbary (2012) from Cassini ultraviolet data, while the black lines either side show the half power points. As in Figure 2, the solid line segments of the trajectories terminated by the solid circles correspond to the trans-periapsis segments employed in the analysis, with dashed line segments being shown beyond (to radial distances of 7 R_S). As indicated by the arrows on the trajectories, the prenoon segments correspond to the northern hemisphere inbound passes and the postnoon segments to the southern hemisphere outbound passes. As also in Figure 2, the near-equatorial solid circles indicate the field-parallel points where the mapped trajectories attain their maximum colatitude with respect to each pole.

3. Initial Appraisal of Periapsis Pass PPO Modulations

As indicated in section 2, the in situ data acquired during the proximal periapsis passes were collected during inbound and outbound sequences of sub-hour traversals of regions with diverse physical characters, namely, auroral, subauroral, ring, and intra-ring field lines, traversals thus taking place on time scales short compared with PPO periods of ~10.7 hr. To discern whether PPO perturbations were present in these regions

we must thus combine data from different passes acquired under conditions of differing PPO phase. We now describe the PPO phases employed in the analysis and use them to provide an initial qualitative appraisal of the PPO effects present on the passes, prior to detailed quantitative analysis in section 4.

3.1. PPO Phases and Periods

Following section 1, the phases of the northern (N) and southern (S) PPO systems are given by

$$\Psi_{N,S}(\varphi, t) = \Phi_{N,S}(t) - \varphi, \tag{1}$$

where $\Phi_{N,S}(t)$ is the azimuth with respect to noon of the prime $\Psi_{N,S} = 0$ meridian of the northern or southern PPO system, while φ is similarly the azimuth with respect to noon of the spacecraft, both taken to increase in the sense of planetary rotation. The phases $\Phi_{N,S}(t)$ for the proximal orbit interval employed here are those determined by Provan et al. (2018) using both northern polar and southern equatorial region data from nightside segments of the same and earlier (F ring) Revs. This analysis showed that from early 2016 to the end of mission, the PPO periods were relatively unchanging within ±0.01 hr at ~10.79 hr for the northern system and ~10.68 hr for the southern system. Due to the increased uncertainties in individual period determinations close to the end of mission due to the diminishing phase data available (none being available from beyond the end of mission, of course), here we have used phase models derived from single linear fits to the phase data from Revs 249 to 293 (essentially the F ring and proximal Revs) spanning from mid-November 2016 to end of mission in mid-September 2017. These phases (in degrees) are given by

$$\Phi_{N,S}(t) = \Phi_{g\ N,S}(t) - \psi_{N,S}(t) = \frac{360t}{\tau_{g\ N,S}} - \psi_{N,S}(t), \tag{2}$$

where the "guide phases" $\Phi_{g\ N,S}(t)$ correspond to those of a fixed period $\tau_{g\ N,S}$, and time $t = 0$ corresponds to 00 UT on 1 January 2004 (essentially the start time of the Cassini science mission). For the northern system Provan et al. (2018) employ $\tau_{g\ N} = 10.8\ \mathrm{h_r}$ and find

$$\psi_N(t) = (287.4 - 0.593(t(\mathrm{days}) - 4700)) \quad \mathrm{deg}, \tag{3}$$

while for the southern system they employ $\tau_{g\ S} = 10.7\ \mathrm{h_r}$ and find

$$\psi_S(t) = (131.3 - 1.588(t(\mathrm{days}) - 4700)) \quad \mathrm{deg}. \tag{4}$$

These expressions are valid for $t \geq 4700$ days, that is, from 00 UT on 13 November 2016 to the end of mission. The corresponding periods are 10.792 hr for the northern system and 10.679 hr for the southern system, with a beat period of ~42.5 days. Uncertainties in these periods are of order ~±0.0005 hr (~2 s), with related overall phase uncertainties of order ~±10°.

With regard to the relative amplitude of the two PPO systems, as mentioned in section 1.1 Provan et al. (2018) deduced an equatorial north/south ratio of ~1.4 during the proximal orbit interval, from consideration of the relative amplitudes of the nightside oscillations employed to determine the phase model. From a study of the modulations observed on the dayside periapsis passes on the F ring orbits (October 2016 to April 2018) immediately preceding the proximal orbit interval, Hunt, Provan, Cowley, et al. (2018) deduced a north/south amplitude ratio of ~1.3. The evidence thus indicates that the northern PPO system was the stronger of the two during the interval considered here, but not by a large factor. In general, we thus expect to find dual PPO modulation with similar amplitudes for the two systems on the proximal passes.

3.2. Overview of Periapsis Pass PPO Modulations

To introduce the nature of the PPO modulations observed on the proximal passes here we make an initial presentation which reveals the major effects present by color-coding the field component time series data by PPO phase, by northern system phase Ψ_N in Figure 4, and by southern system phase Ψ_S in Figure 5. Specifically, we plot the spherical polar field components with planetary and ring current fields subtracted (as detailed below) versus time, organized relative to the near-equatorial field-parallel points taken as $t = 0$ (Figure 2). The figures encompass the interval from $t = -100$ min to $t = +80$ min, spanning the full periapsis intervals considered here as discussed in section 2. The plots thus include traversals of auroral,

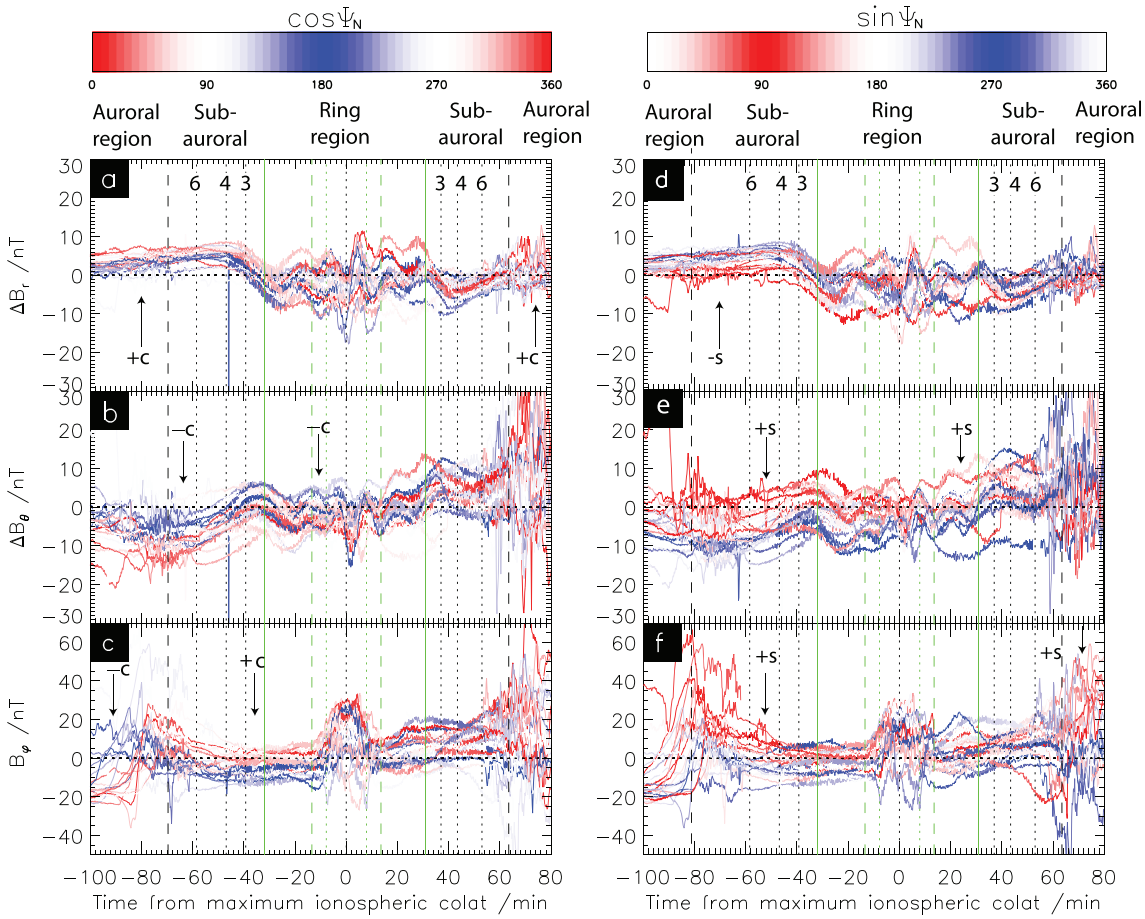

Figure 4. Field data at 10s resolution from all the proximal orbit periapsis passes, color-coded according the northern PPO system phase, Ψ_N, are shown plotted versus time from their field-parallel points taken as $t = 0$ (central vertical black dotted line), over the interval between −100 and +80 min (see section 2). Vertical black dashed lines indicate the equatorward boundary of the auroral region taken to lie at 18° mapped northern ionospheric colatitude (~19.9° mapped colatitude in the southern ionosphere and mapping to ~9.0 R_S in the equatorial plane), the black dotted lines marked 3, 4, and 6 mark subauroral field lines that map to the equatorial plane at corresponding radial distances in R_S, the green solid lines mark the field line passing through the outer boundary of the A ring, while the green dashed and dotted lines mark the field lines passing through the outer and inner boundaries of the D ring, respectively. Data in Figures 4a–4c on the left are color-coded by northern PPO phase such that phases near 0°–360° are colored red and phases near 180° blue, as indicated above these panels. Separation of red and blue data in either direction, red data larger than blue or vice versa, indicates northern PPO modulation as $\pm\cos\Psi_N$, with evident intervals marked as "±C" in these figures. Similarly, data in Figures 4d–4f on the right are color-coded by northern PPO phase such that phases near 90° are colored red and phases near 270° blue, as indicated above these panels, such that separation of red and blue data in either direction indicates northern PPO modulation as $\pm\sin\Psi_N$, with evident intervals marked as "±S" in these figures.

subauroral, ring region, and intra-ring field regions both inbound and outbound (see Figure 2), as shown by the vertical lines and as marked at the top of the figures. The black dashed lines show the equatorward boundary of the auroral region taken to lie at 18° northern ionospheric colatitude, equivalent to ~19.9° southern ionospheric colatitude, which maps to ~9.0 R_S in the equatorial plane. The black dotted lines marked 6, 4, and 3 indicate subauroral field lines mapping to the corresponding radial distances (R_S) in the equatorial plane. The green solid lines mark the field line passing through the outer boundary of the A ring both inbound and outbound, thus delineating the ring data interval, while the green dashed and dotted lines indicate the field lines passing through the outer and inner boundaries of the D ring, respectively. Although these boundaries do vary by a minute or two from pass to pass relative to $t = 0$, marked by the central black dotted line, those shown represent averages over the whole data set, providing a sufficiently accurate indication.

From top to bottom in Figures 4 and 5, the panels show the color-coded data for the residual radial (Figures 4a, 4d, 5a, and 5d), residual colatitudinal (Figures 4b, 4e, 5b, and 5e), and the azimuthal (Figures 4c, 4f, 5c, and 5f) field components. The residual poloidal fields have the 11-order internal

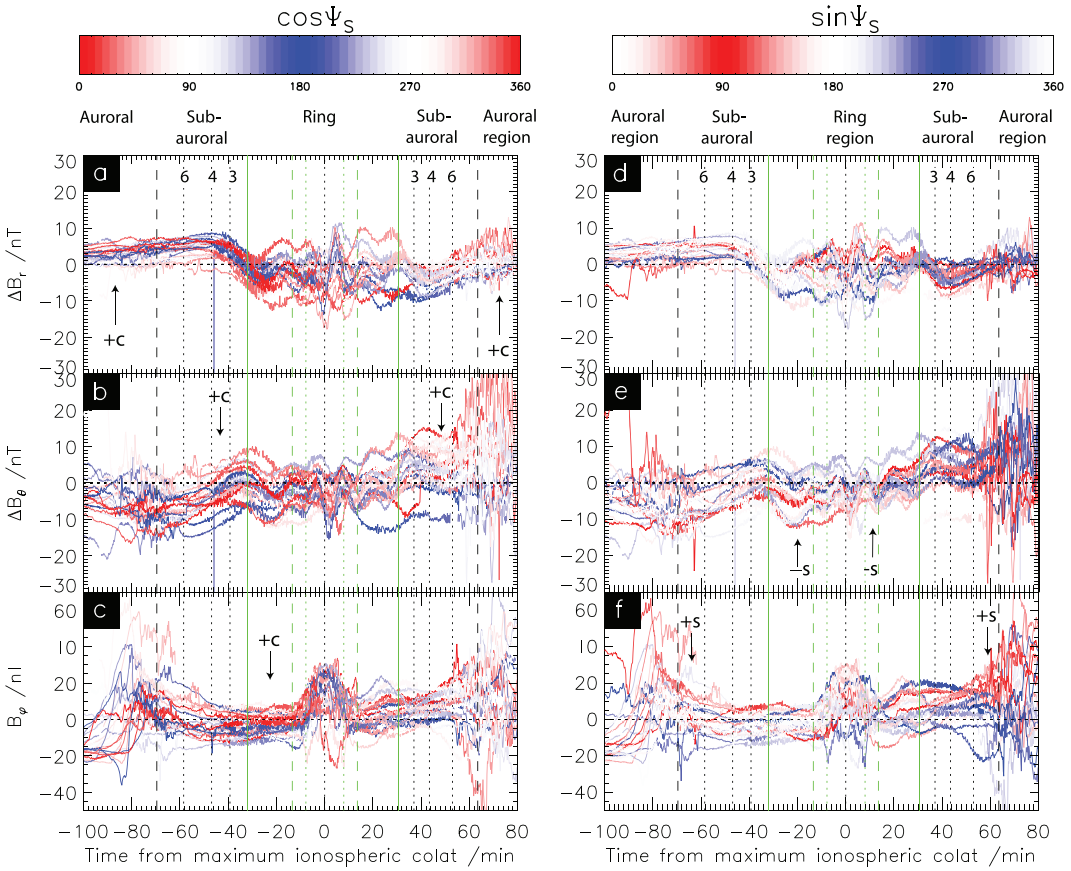

Figure 5. Same as for Figure 4 but where the field data have been color-coded according to the southern PPO system phase Ψ_S.

planetary field of Dougherty et al. (2018) subtracted, together with the Bunce et al. (2007) ring current model for a subsolar magnetopause at 22 R_S (as employed in Figures 2 and 3). Since this model is axisymmetric with zero azimuthal component, the azimuthal field data are shown as measured. These data have been averaged to 10-s resolution, as employed throughout the paper. The notable increase in measurement "noise" occurring between ~−44 min inbound and ~+57 min outbound is due to the magnetometer instrument changing to its highest field range when the field magnitude exceeded 10,000 nT (Dougherty et al., 2018). The variable field behavior associated with the auroral, subauroral, and ring regions is particularly well-marked in the azimuthal component data, including the strong central azimuthal field signatures on and inside of D ring field lines associated with the low-latitude magnetosphere-ionosphere current system discussed by Dougherty et al. (2018), Khurana et al. (2018), and Provan, Cowley, et al. (2019).

The field data in Figures 4 and 5 are color-coded by PPO phase as a function of time on each pass according to the color bars shown at the top of each figure. We note that since each pass lasts for about a quarter of a PPO cycle (~2.8 hr), the PPO azimuths $\Phi_{N,S}$ increase by ~90° during each pass, while the spacecraft azimuth φ increases by ~180° between northern dawn and southern dusk auroral regions (Figure 2). During these passes the spacecraft thus significantly "superrotated" with respect to the PPO systems, with the PPO phases $\Psi_{N,S}$ given by equation (1) decreasing with time through ~90° on each pass, thus requiring the data to be variably color-coded as a function of time. In the left hand panels of each figure, corresponding to Figures 4a–4c and Figures 5a–5c, phases near 0°/360° are color-coded red and those near 180° blue, termed here the "cos" plots, while in the right hand panels corresponding to Figures 4d–4f and Figures 5d–5f, phases near 90° are color-coded red and those near 270° blue, termed here the "sin" plots. If the data for a particular field component are modulated as $\cos\Psi_{N,S}$, the pass-to-pass data will be separated by color in the cos plots, with red data having larger values than blue, while no overall separation would occur in the corresponding sin plot. If instead the field component is modulated as $-\cos\Psi_{N,S}$, then the data will be color separated with

blue data larger than red in the cos plot. For convenience of subsequent discussion such color separation will be denoted below as "R > B" for red data larger than blue, and as "B > R" for blue data greater than red. Similarly, if the data are modulated as $\sin\Psi_{N,S}$, the data will be separated in the sin plot with R > B, with no overall separation in the related cos plot. If instead it is modulated as $-\sin\Psi_{N,S}$, the data will be separated in the sin plot with B > R. Partial separation of data in both cos and sin plots for a given component indicates overall modulation at an intermediate phase, noting that

$$\cos(\Psi-\Delta) = \cos\Delta\cos\Psi + \sin\Delta\sin\Psi, \tag{5a}$$

and

$$\sin(\Psi-\Delta) = \cos\Delta\sin\Psi-\sin\Delta\cos\Psi, \tag{5b}$$

such that the senses of the two modulations, R > B or B > R, also indicate the phase quadrant of the phase deviation Δ. Intervals of clear modulation are indicated in Figures 4 and 5 by the arrows marked "±C" for $\pm\cos\Psi_{N,S}$ modulations in the cos plots, and by the arrows marked "±S" for $\pm\sin\Psi_{N,S}$ modulations in the sin plots.

With regard to the issue of color-coding generally dual-modulated data separately with regard to the northern and southern phases $\Psi_{N,S}$ in order to discern the individual modulations present, we note that the overall proximal orbit interval April to September 2017 corresponded to ~3.5 beat cycles of ~42.5 days, such that the northern and southern phases of the two systems were overall uncorrelated. Modulation due to one system then simply introduces a level of scatter into the data organized relative to the phase of the other system, with little net result. This cross-modulation issue is discussed further in section 4, following quantitative examination in Appendix A.

We first consider the results in Figure 4 where the data are color-coded by the northern PPO phase, Ψ_N, noting from section 3.1 that northern system modulation is expected to be the larger of the two during this interval, if not by a large factor. Following section 1.2, for this system we expect the radial component to vary as $\sim\cos\Psi_N$ giving rise to R > B separation in Figure 4a (the cos plot), the colatitudinal component as $\sim -\cos\Psi_N$ giving rise to B > R separation in Figure 4b (the cos plot), and the azimuthal component (in the equatorward region) as $\sim\sin\Psi_N$ giving rise to R > B separation in Figure 4f (the sin plot). Examining these figures, the expected modulations are clearly seen to be present in the northern inbound data, as indicated by the vertical arrows marked ±C for $\pm\cos\Psi_N$ modulations and ±S for $\pm\sin\Psi_N$ modulations as indicated above. For the radial component in Figure 4a we see R > B separation indicative of $\cos\Psi_N$ modulation in the northern auroral and subauroral region from the start of the interval to ~−40 min, though becoming less obvious in ring region data. R > B separation is also evident in the southern auroral region, as also indicated in Figure 4a. However, in Figure 4d we also see B > R separation in the radial component data indicative of $-\sin\Psi_N$ modulation throughout most of the northern inbound pass extending to outer ring field lines at ~−30 min. From equation (5a) the combination of positive cosΔ and negative sinΔ shows that phase deviation Δ lies at earlier phases between 0° and −90. An "earlier" phase deviation means that given peaks and troughs of the oscillation occur at earlier times than those of the unmodified oscillation, for which Δ = 0°.

Similarly, for the colatitudinal component in Figure 4b we see B > R separation indicative of $-\cos\Psi_N$ modulation as expected in the northern inbound data now extending from the auroral region through the ring region, though becoming less obvious after the field-parallel point at t ~0. In Figure 4e, however, we also see R > B separation indicative of $\sin\Psi_N$ modulation in this component that extends throughout the northern auroral and subauroral region and across the ring region to the southern outbound inner subauroral region near ~+35 min. Again, from equation (5a) this combination of modulations indicates a shift to earlier phases with Δ lying between 0° and −90°.

For the azimuthal component in Figure 4f we see R > B separation indicative of $\sin\Psi_N$ modulation in the northern inbound data as expected to ~−50 min, becoming less obvious in inner subauroral and ring region data, before reemerging in southern outbound auroral region data after ~+60 min. In Figure 4c, however, we initially see B > R separation on the northern inbound pass indicative of $-\cos\Psi_N$ modulation to ~−80 min, then reversing to R > B separation indicative of $\cos\Psi_N$ modulation which is present throughout the remainder of the northern passes, in the auroral, subauroral, and ring regions, but is not apparent in the southern

main ring and subauroral regions. From equation (5b) we note that with the exception of the earliest northern auroral data that indicate a shift to somewhat later phases, these data again indicate a shift to earlier phases, that is, Δ between 0° and −90°, from ~sinΨ_N in the outer regions to ~cosΨ_N in the inner subauroral and ring regions.

In Figure 5 the same data are shown color-coded by southern PPO phase Ψ_S. As discussed in section 1.2, for this system we expect the radial component to vary as ~cosΨ_S, the colatitudinal component as ~cosΨ_S (opposite to the sense of the northern modulation), and the azimuthal component (in the equatorward region) as ~sinΨ_S, thus leading to expected related modulations in Figures 5a, 5b, and 5f, respectively. Given that the northern system is also expected to be the larger amplitude system during this interval, the southern system separation results may be expected to be somewhat noisier than those for the northern system in Figure 4, except perhaps in the outbound southern hemisphere.

For the radial component in Figure 5a we see clear R > B separation indicative of cosΨ_S modulation in the southern outbound data, extending from the outer southern ring region to subauroral and auroral region data to the end of the interval shown. Little consistent separation is seen in Figure 5d. For the colatitudinal component in Figure 5b, we see R > B separation indicative of cosΨ_S modulation in the northern inbound subauroral data extending into the ring region between ~−65 and ~−20 min, and in the southern outbound subauroral and auroral data to the end of the interval shown. In Figure 5e we also see B > R separation indicative of −sinΨ_S modulation in the northern subauroral and ring region data north and south, again indicating a shift to earlier phases. For the azimuthal component in Figure 5f we see R > B separation indicative of sinΨ_S modulation throughout both the northern and southern auroral and subauroral region data, as expected, though becoming less evident within the ring region. In Figure 5c we also see R > B separation indicative of cosΨ_S modulation within the ring region in the northern hemisphere, again indicating a shift to earlier phases, though not in the south.

Overall, the data presentation in Figures 4 and 5 clearly demonstrate that field modulations associated with both the northern and the southern PPO systems are present throughout much of these passes, though with the northern modulations generally more clearly delineated in the northern inbound data and the southern modulations in the southern outbound data, as expected from the previous related analyses of Hunt et al. (2015), Hunt, Provan, Cowley, et al. (2018) and Bradley, Cowley, Provan, et al. (2018). In particular, the results show for the first time that PPO field oscillations are indeed present in the ring field region, as most clearly demonstrated in both the northern and southern system modulations in the colatitudinal and northern azimuthal field component data. It can further be seen directly that the PPO modulations contribute significantly to the overall field variability in these regions, though not being related to the azimuthal component variability in the central D ring and intra-D ring region (Provan, Lamy, et al., 2019). The data are also indicative of overall shifts to somewhat earlier phases in both the northern and southern system oscillations than those anticipated from the phase models of Provan et al. (2018), that is, cos$\Psi_{N,S}$ modulations moving toward −sin$\Psi_{N,S}$ and sin$\Psi_{N,S}$ toward cos$\Psi_{N,S}$, an effect that appears to increase on ring region field lines.

4. Quantitative Analysis of PPO Modulations in Periapsis Pass Data

Although Figures 4 and 5 provide a simple visual overview of PPO modulations in the proximal data, in this section we present a more detailed quantitative analysis. This is similarly based on the premise that the ring region field is dual modulated by the northern and southern PPO systems in a similar manner to that demonstrated in previous studies of magnetospheric regimes beyond the rings, cited in section 1. We thus fit the field component data to appropriate rotating functions of sinusoidal form employing the northern and southern PPO phases derived for this interval by Provan et al. (2018) using near-apoapsis field data, to determine the amplitude and phase of the northern and southern PPO modulations present in each of the periapsis pass physical regimes traversed.

4.1. Sinusoid Fits to the Proximal Data as Functions of PPO Phase

In previous related analyses of inclined orbit periapsis pass data devised to investigate the structure of field-aligned currents from azimuthal field measurements, the data acquired from differing Revs were first transformed to estimated ionospheric values in order to make approximate allowance for the

generally differing radial distances of the data on given field lines on differing Revs (Hunt et al., 2014, 2015, 2016; Bradley, Cowley, Provan, et al., 2018). This was done by taking $\rho B_\varphi \approx$ constant along a given field line between the point of measurement and the hemispheric ionosphere in question, where, as in section 2, ρ is the perpendicular distance from the spin/magnetic axis and B_φ is the azimuthal field. This procedure assumes approximate local axisymmetry, that is, latitude scales small compared with longitude scales, and negligible cross-field current flow between these points. The mapped ionospheric field values, or equivalently the inferred colatitudinal ionospheric current per radian of azimuth, $I \approx -\rho B_\varphi/\mu_o$ (where μ_o is the permeability of free space), were then organized by PPO phase to determine the nature of the related modulations. In the present case, however, the proximal periapsis passes are all closely similar to each other in the meridian as shown in Figure 2, though varying systematically in azimuth across the data set through ~1.8 hr of LT on a given flux shell as shown in Figure 3. Here we therefore simply analyze B_φ as measured, and also similarly analyze the residual spherical polar radial B_r and colatitudinal B_θ field components as well.

To take clear account of the differing physical regimes on these passes, however, prior to PPO analysis the data are again organized by field line (or flux shell) into variable width bins of mapped ionospheric colatitude. We choose to employ the northern ionospheric colatitude as organizing parameter for both the northern inbound and the southern outbound data in order to facilitate their comparison, but we also provide equivalent scales of mapped southern ionospheric colatitude throughout. The field component data from each Rev so organized by mapped ionospheric colatitude are then plotted separately versus northern and southern PPO phases $\Psi_{N,S}$ in order to discern any modulation present. We note that the validity of this procedure applied to the, in general, dual-modulated field data relies on the overall lack of correlation between the northern and southern PPO phases over the ~3.5 beat period data set as noted in section 3, such that modulations due to one system simply introduce a level of scatter into the data organized relative to the other system, while not significantly affecting the determination of the amplitude and phase. This assertion is examined quantitatively in Appendix A via analysis of a simulated dual-modulated data set of known content, where it is shown for the data examined here that if the modulations due to a given system are of amplitude A, the resulting scatter in the data organized relative to the other system affects the deduced amplitudes typically by ~$\pm 0.1A$, which for approximately equal amplitude systems usually represents only a small effect.

We thus fit the residual poloidal and azimuthal component data (as shown in Figures 4 and 5) separately to the northern (N) and southern (S) system functions

$$B_{j\ N,S}\left(\Psi_{N,S}\right) = B_{j0\ N,S}\cos\left(\Psi_{N,S} - \gamma_{j\ N,S} - \Delta_{j\ N,S}\right),$$

where $\Psi_{N,S}$ is the northern or southern PPO phase given by equation (1), index $j = (r, \theta, \varphi)$ indicates the spherical polar field component, angle $\gamma_{jN,S}$ gives the expected phase of component j relative to the r component as discussed in section 1, and the fit parameters are the amplitudes $B_{j0N,S}$ and the phase deviation angles $\Delta_{jN,S}$. By definition of the PPO phases, for the r component we have $\gamma_{rN,S} \equiv 0°$, while according to section 1 we have $\gamma_{\theta\ N} = 180°$, $\gamma_{\theta S} = 0°$, and (in the equatorial region) $\gamma_{\varphi\ N,S} = 90°$. Taking account also of the mean (in general residual) values $\overline{\Delta B_j}$ about which the field components are modulated, the fit functions for the three field components are thus taken as

$$B_{r\ N,S} = \overline{\Delta B_r}_{N,S} + B_{r0\ N,S}\cos\left(\Psi_{N,S} - \Delta_{r\ N,S}\right), \tag{6a}$$

$$B_{\theta\ N,S} = \overline{\Delta B_\theta}_{N,S} + \mathrm{sgn}_{N,S} B_{\theta 0\ N,S}\cos\left(\Psi_{N,S} - \Delta_{\theta\ N,S}\right), \tag{6b}$$

where the sign function is such that $\mathrm{sgn}_N = -1$ while $\mathrm{sgn}_S = +1$, and

$$B_{\varphi\ N,S} = \overline{B}_{\varphi\ N,S} + B_{\varphi 0\ N,S}\sin\left(\Psi_{N,S} - \Delta_{\varphi\ N,S}\right). \tag{6c}$$

For modulations exactly in phase with the Provan et al. (2018) models we thus simply have $\Delta_{jN,S} = 0°$ throughout, while finite values of $\Delta_{jN,S}$ (modulo 360°) indicate departures from those expectations. In particular, deviations to earlier phases notable in the inner region data in Figures 4 and 5 correspond to negative values of $\Delta_{jN,S}$ between 0° and −90°, as indicated in section 3.2. Details of the fit procedure and uncertainty estimates are given in section 4.1.1 below, where results are introduced.

As discussed in section 2.1 in relation to Figure 2, the bins of mapped northern ionospheric colatitude determined by the spacecraft orbit extend from 15.6° on the northern inbound passes (corresponding to ~17.3° in the southern ionosphere) and back to 17° on the southern outbound passes (corresponding to ~18.8° in the southern ionosphere). The maximum northern ionospheric colatitude for which sufficient data are available for analysis is set by the typical spacecraft altitude near periapsis, which examination shows is 72° both inbound and outbound (equivalent to ~81.8° colatitude in the southern ionosphere). We further use nonoverlapping colatitude bins of variable width tailored to the nature of the data, with narrower bins of 0.2° and 0.5° in auroral and subauroral regions down to 20° northern colatitude, where the spacecraft colatitude varies slowly with time while the field component data vary rapidly with time (Figures 4 and 5), and bins of 1° at larger colatitudes. The relatively finely spaced nature of the bins allows the consistent Rev-by-Rev small-scale variations evident particularly in the residual poloidal components in the inner regions in Figures 4 and 5 not to be factored into the overall variations in a given bin.

4.1.1. Northern PPO Modulations in Azimuthal Component Data

In Figure 6 we show some sample fits, specifically for the azimuthal field component, whose oscillations have generally been found to have largest amplitudes in previous studies of near-equatorial data (e.g., Andrews, Cowley, et al., 2010; Andrews et al., 2012; Provan et al., 2013). Each panel of the figure shows the 10s averaged data contributing to a given colatitude bin, color-coded by Rev number as indicated at the top of the figure, plotted versus the northern system phase Ψ_N, with two cycles of PPO phase being shown to aid visualization of data continuity. The mapped northern ionospheric colatitude range is indicated in the top left corner of each panel. Data from the northern inbound passes are shown in Figures 6a–6e (left column), while data from the same mapped colatitudes obtained in the southern hemisphere on outbound passes are shown in Figures 6f–6j (right column). The values from each Rev were first averaged to find the mean value of the field and phase for that Rev (the phase values from a given Rev being essentially constant), with the means being shown by the overplotted black crosses. The best fit parameters of equation (6c) to the black cross values, the mean value $\overline{B}_\varphi$, the amplitude $B_{\varphi 0}$, and the phase deviation Δ_φ, were then obtained using least squares minimization, yielding the fits shown by the black dashed sinusoids varying about the horizontal black dashed lines showing the mean. The fit parameters are given in the bottom portion of each panel, together with the root-mean-square (RMS) deviation of the field values from the fitted line, denoted as RMS in the figure. For purposes of later discussion we also give the RMS deviation of the data from the arithmetic mean of the data, denoted as RMS*. The uncertainties in the fit values shown in each panel were estimated using the "jackknife" statistical resampling method (e.g., section 4 of Wolter (2007)). In this procedure, with N data points (here generally 22 or 23 depending on whether data from final Rev 293 contribute to the data bin), the fit is repeated N times with one data point being successively removed from the data set in each fit. The standard deviation σ of this set of N fit parameters is then calculated, yielding an estimate of the standard deviation of the fit parameter for the data set as a whole of $\sqrt{N-1}\ \sigma$. For phase Δ_φ, the circular standard deviation is given (Mardia and Jupp (2000) and section 4.1 of Hunt et al. (2015)).

Figures 6a–6e show fits to the northern inbound data for selected mapped ionospheric colatitude bins that span from the auroral region to inside the inner boundary of the D ring. Specifically, Figure 6a shows data from the equatorial edge of the northern auroral region spanning 17.5°–18° northern ionospheric colatitude (mapping to the equator at ~9.5 R_S), chosen as an auroral region range that is traversed in both hemispheres. A northern system oscillation of ~11nT amplitude is clearly present, with a phase that deviates from simple expectation by $\Delta_\varphi \approx -20°$. Figure 6b similarly shows northern data from subauroral field lines spanning 24°–25° northern ionospheric colatitude (~4.25 R_S at the equator), where an oscillation of moderately reduced ~7.5nT amplitude is evident, with a larger phase deviation $\Delta_\varphi \approx -50°$. Figure 6c shows data from field lines spanning 44°–45° northern ionospheric colatitude (~1.64 R_S at the equator), mapping to the inner B ring region. An oscillation of ~5-nT amplitude is present with a phase deviation of $\Delta_\varphi \approx -70°$, demonstrating that PPO oscillations are present on ring region field lines, though with an earlier phase than in the outer region, as previously deduced on a qualitative basis from Figure 4. Figure 6d shows data from field lines spanning 59°–60° northern ionospheric colatitude (~1.19 R_S at the equator), mapping to the D ring region. The fit again indicates the presence of an oscillation of ~5nT amplitude with a phase deviation $\Delta_\varphi \approx -80°$ similar to that observed in the B ring region in Figure 6c. Figure 6e shows data from field lines spanning 69°–70° northern ionospheric colatitude (~1.07 R_S at the equator), close to the largest values observed on the proximal passes, mapping inside the inner edge of the D ring. Here the data are much

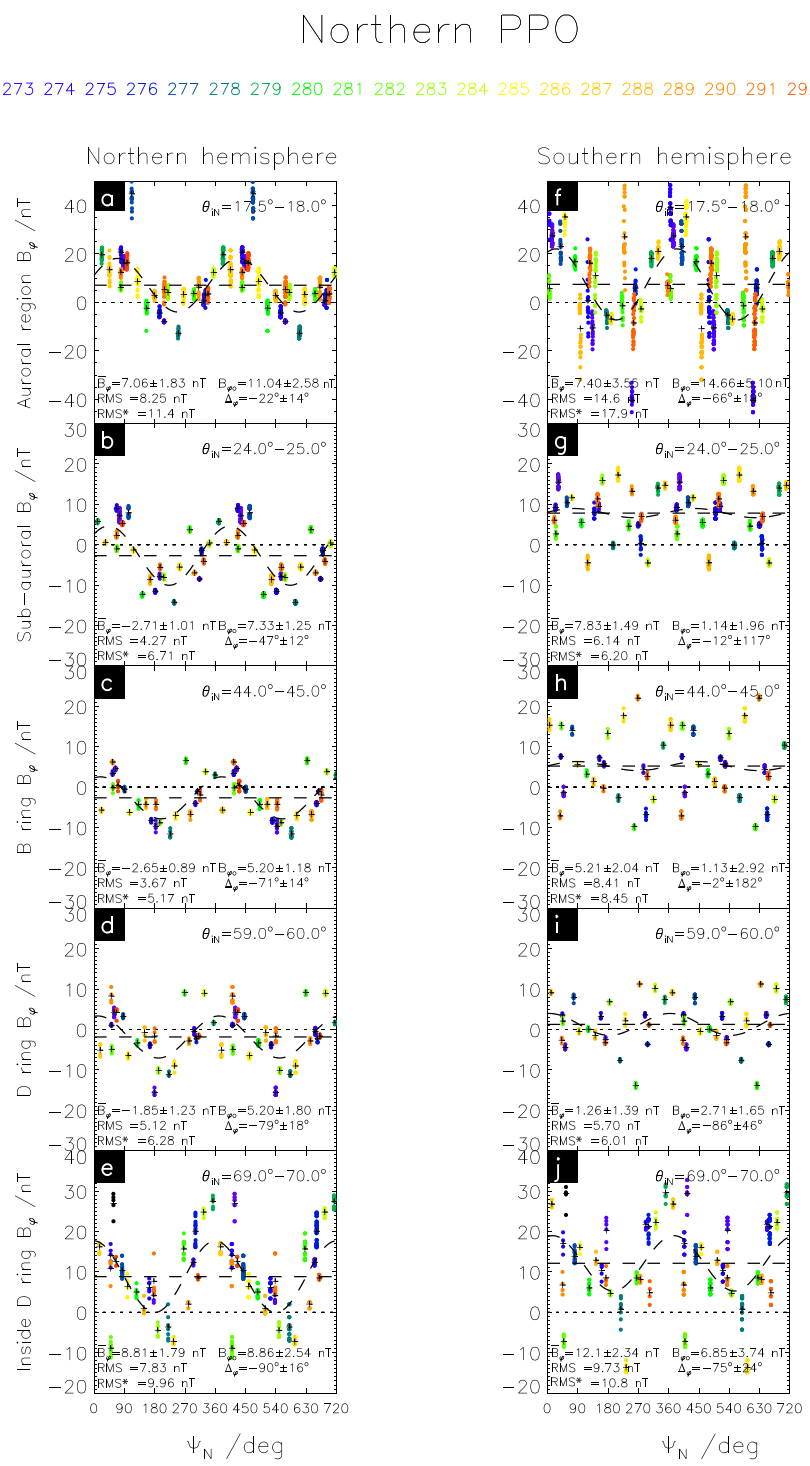

Figure 6. Plots showing individual sinusoidal fits to azimuthal field component data (10s resolution) divided into bins of mapped northern ionospheric colatitude, where Figures 6a–6e show data in selected bins from northern hemisphere inbound data, and Figures 6f–6j corresponding data on the same mapped flux shells from southern hemisphere outbound data, both plotted versus northern PPO system phase Ψ_N. The mapped northern ionospheric colatitudes in each figure are shown in the top right corner, and correspond to the auroral regions in Figures 6a and 6f, the subauroral regions in Figures 6b and 6g, the B ring region in Figures 6c and 6h, the D ring region in Figures 8d and 6i, and inside the D ring in Figures 6e and 6j, as indicated on the left of the figure. Individual 10s data are plotted as solid circles color-coded by Rev number as shown at the top of the plot, with two cycles of phase being shown such that each data point is plotted twice. Rev-averaged field values and phases are shown by overplotted crosses. Least squares sinusoidal fits of equation (6c) to these averaged points are shown by the black dashed lines, where the horizontal black dashed line indicates the mean value $\overline{B}_\varphi$. The fit parameters are given at the bottom of each figure, together with the root-mean-square deviation of the data from the fitted line RMS, and the root-mean-square deviation of the data from the mean of the data RMS*.

more variable from pass to pass due to the simultaneous presence of the intra-D ring region field perturbations that are not organised by the PPOs (Provan, Cowley, et al., 2019). Even so, an oscillation is clearly present with an increased amplitude of ~9 nT and a phase deviation of $\Delta_\varphi \approx -90°$. Overall, these data confirm the qualitative conclusions from Figure 4 that (in this case northern system) PPO-related magnetic field oscillations are present at significant amplitudes on and inside of Saturn's ring region field lines, with a modest augmentation of the amplitude in the azimuthal component inside the D ring region. In all cases the fitted amplitudes are well above the estimated uncertainties by at least a factor of ~3. They also confirm the move to earlier (negative Δ_φ) phases in the inner region compared with auroral and subauroral regions, the phase change between the data in Figures 6a (auroral) and 6d and 6e (D ring and intra-D ring) being ~70°.

In Figures 6f–6j we examine the dependence of the azimuthal field on northern system phase on the same flux shells in the southern hemisphere on the outbound passes. As can be seen by comparing panels across the two columns of the figure, these data are more scattered than equivalent data from the northern inbound passes, with larger fit RMS values, particularly outside of D ring field lines. Indeed, for both the B ring and subauroral data in Figures 6g and 6h the fitted amplitudes are smaller than the estimated uncertainty, thus being consistent with zero. Nevertheless, in the southern intra-D ring and auroral data (Figures 6i, 6j, and 6f) the fits indicate the continued presence of northern system oscillations on the same flux shells in the southern hemisphere, in line with Figure 4, with negative phase deviations similar to those in the northern hemisphere.

As a confidence check on the amplitude determinations relative to the error estimates in Figure 6 (and subsequent figures), and the conclusions drawn from them concerning the validity of the fit results, we have compared the outputs with the amplitudes obtained from fits to random data values under the circumstances of the proximal orbits (i.e., 22 or 23 data values fairly uniformly distributed in PPO phase). Clearly, very particular sets of data obtained from a random sequence could accidentally give rise to fits with arbitrary amplitude larger than uncertainties as estimated above. What we wish to determine, however, is the value of the amplitudes that typically arise from random data sets of given overall RMS scatter, and their magnitude relative to the estimated uncertainties. In many instances it is evident that a significant contributor to the scatter in the data organized relative to a particular PPO system phase arises from the modulation due to the other PPO system. This can be seen, for example, from comparison of the panels of Figure 6 organized with respect to the northern PPO phase with those of Figure 7 (introduced in section 4.1.2), which show the same data organized with respect to the southern PPO phase. In this case the results in Appendix A and Figure A1, together with a wider set of fit results not displayed, show that for a sinusoidal modulation of unit amplitude in one system, the mean amplitudes derived from the essentially randomized data in the other system is ~0.1, as indicated in section 4.1 above. The RMS deviation about zero of such sinusoidally modulated data is $\tilde{}1/\sqrt{2}$, so the typical ratio of the amplitude divided by the RMS deviation for such randomized data is ~0.15. We have also examined the amplitudes derived from random data that on average are uniformly distributed between −1 and +1, and find in this case that the typical fitted amplitudes are somewhat larger at ~0.2. Since the RMS value for such uniform distributions is $\tilde{}1/\sqrt{3}$, the typical ratio of the amplitude divided by the RMS deviation of the data in this case is ~0.35, approximately twice as large as for the sinusoidal data distribution. For some combination of the two noise sources, modulation from the other PPO system and more uniformly distributed data scatter, we may expect a typical amplitude, normalized to the data RMS, which lies between these two values, that is, between ~0.15 and ~0.35. Overall, it thus seems reasonable to conclude that under the circumstances of the proximal orbits, fits to random data may typically yield amplitudes of a factor of ~0.25 of the data RMS, within a typical range between ~0.15 and ~0.35.

We now relate these findings to the ratio between the amplitude and the uncertainty estimated using the jackknife procedure, used here to assess the quality of the fits obtained to the data. Examination of the random data sets shows that a factor of ~1/3 exists between the estimated uncertainties in the fit amplitudes and the overall RMS of the data set (see, e.g., Figure A1). The same approximate linear uncertainty/RMS ratio ~1/3 is also found to apply to a majority of the fits to the magnetic data in Figure 6 (and Figures 7–9 introduced in sections 4.1.2 and 4.1.3 below), the relevant overall RMS value being given as RMS* in the figure panels. This ratio applies in the majority of cases where, like the random data, the fitted amplitude is smaller than the RMS* value. For the minority of cases with very strong data modulation for which the fitted

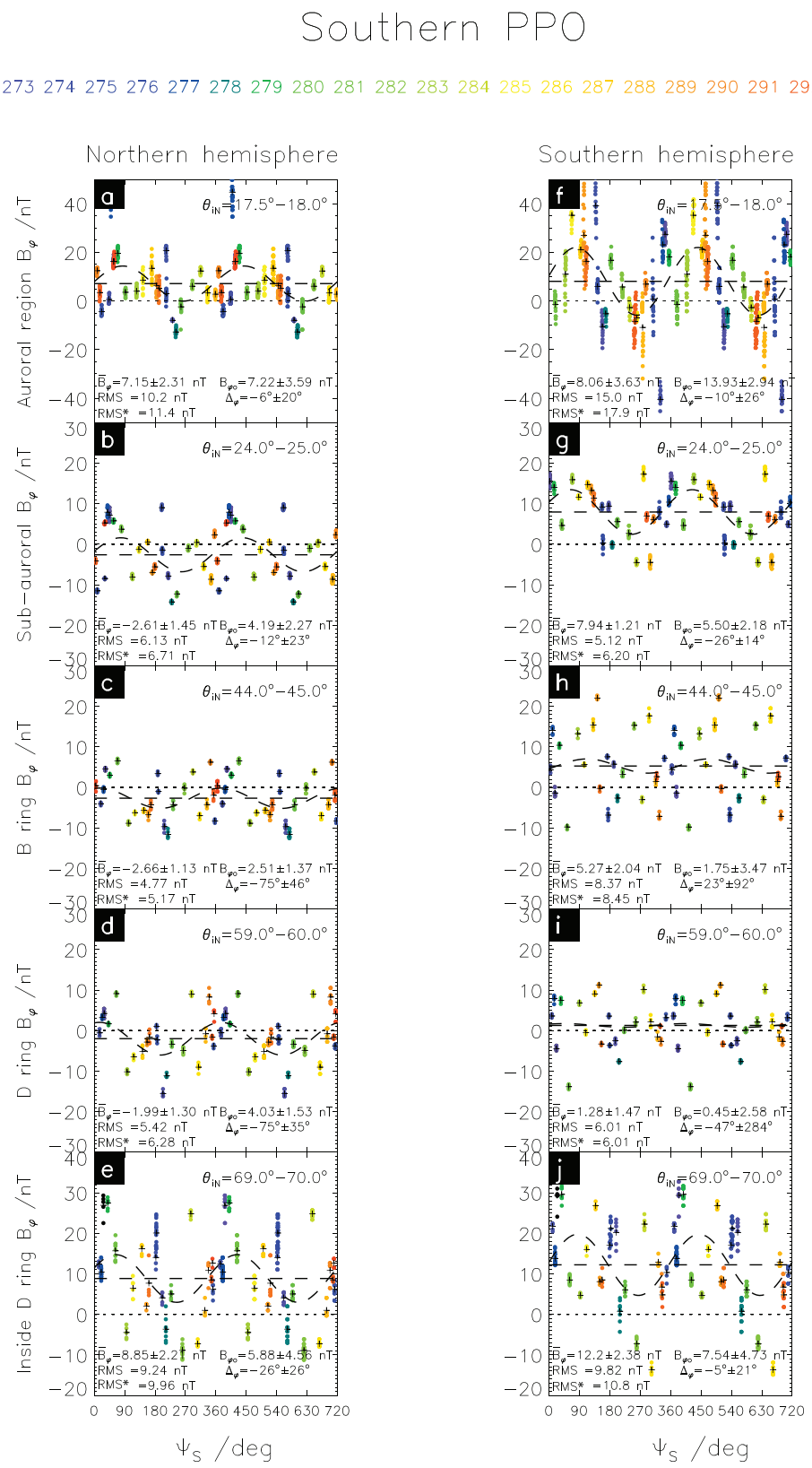

Figure 7. Same as for Figure 6 but showing the northern hemisphere inbound azimuthal component data plotted versus the southern PPO system phase Ψ_S.

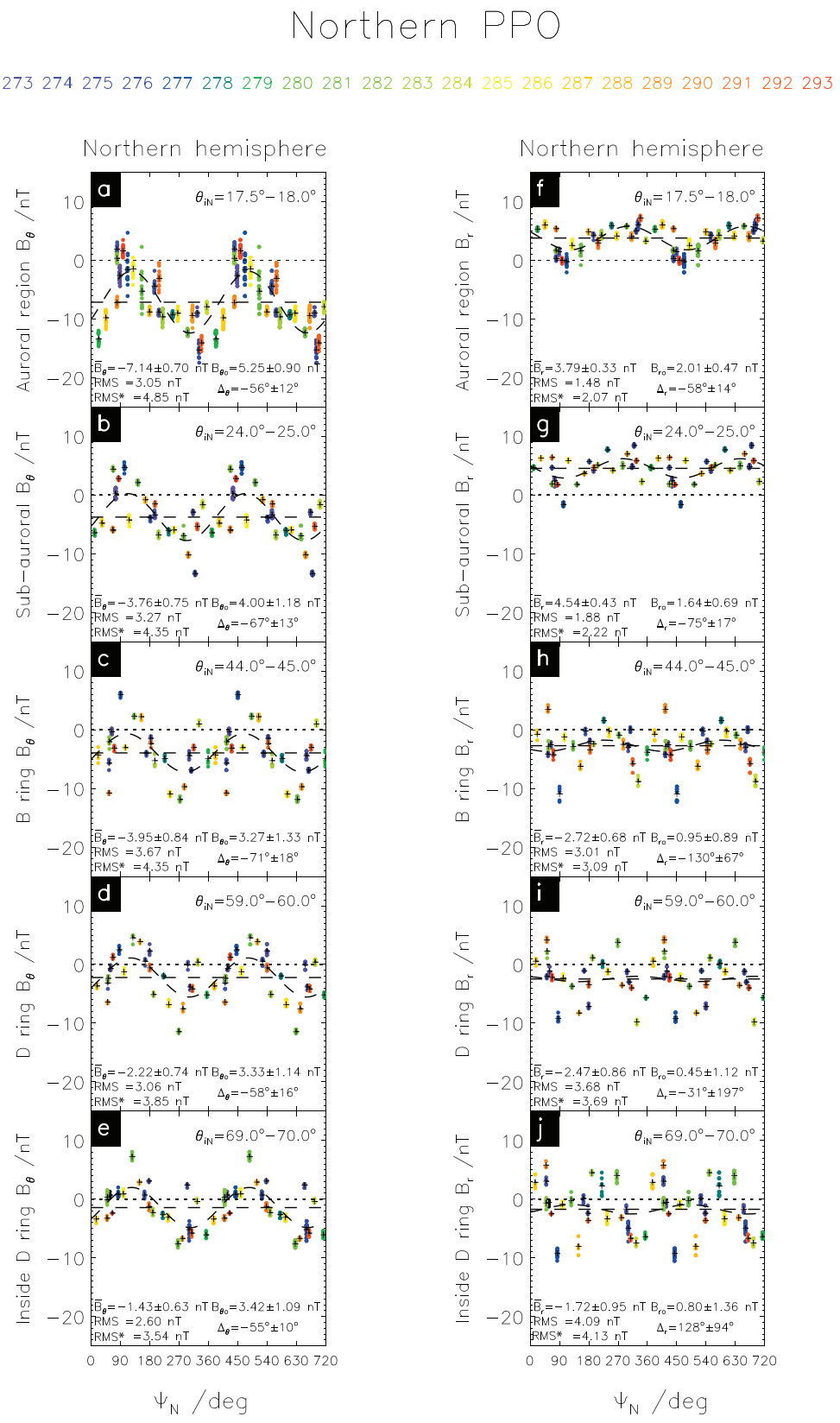

Figure 8. Similar to Figure 6 but showing the residual colatitudinal (Figures 8a–8e) and radial (Figures 8f–8j) field components from the northern hemisphere inbound passes plotted versus northern PPO phase Ψ_N.

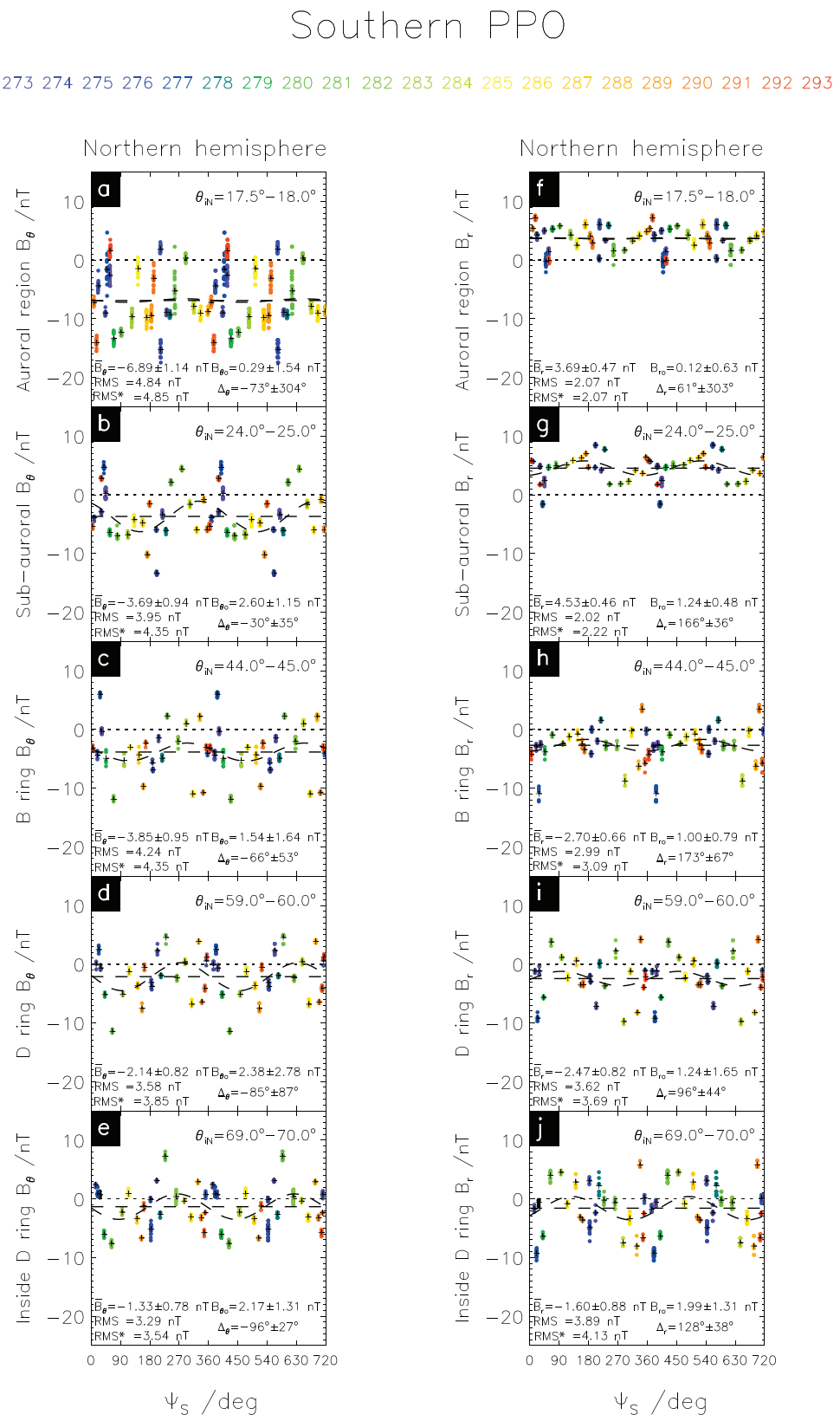

Figure 9. Same as for Figure 8 but showing the residual colatitudinal (Figures 9a–9e) and radial (Figures 9f–9j) field components from the northern hemisphere inbound passes plotted versus southern PPO phase Ψ_S.

amplitude becomes comparable with the RMS* value (e.g., Figures 6a–6c), the estimated uncertainty may fall to a quarter or a fifth of RMS*. We now recall the above discussion that for random data the typical amplitudes are ~0.25 of the overall RMS of the data, within a likely range ~0.15 to ~0.35. Combining this with the factor of ~1/3 between the estimated uncertainty and the overall RMS value, implies that for fits to random data the typical ratio between the amplitude and the estimated uncertainty is ~3×0.25≈0.75, within a likely range between ~3×0.15≈0.45 and ~3×0.35≈1.05. These results thus indicate that we may take fitted amplitudes that are comparable with or smaller than the jackknife estimated errors to correspond to "noise level" fits to random data, that is, consistent with zero as discussed above. Correspondingly, however, amplitudes that are somewhat larger than the jackknife estimated uncertainties are not generally consistent with fits to random data, and may generally be considered to be "well determined." As discussed in section 4.2.2 below, our overall results are in agreement with this conclusion, in showing general consistency in the behavior of the well determined data both between the differing field components of a given PPO system, and between the two individual PPO systems. Qualitatively, PPO modulation of the data becomes visually evident in the distributions in Figure 6 (and Figures 7–9) for cases in which the amplitude is at least half of RMS*, that is, for cases in which the peak-to-peak modulation is at least comparable with RMS*, thus also implying cases where the ratio of the amplitude to the uncertainty exceeds ~1.5.

4.1.2. Southern PPO Modulations in Azimuthal Component Data

In Figure 7 we show the azimuthal component data plotted versus southern system phase Ψ_S in the same format as Figure 6. For the outbound southern hemisphere data in the right hand column, clear southern period oscillations are present in the auroral and subauroral data in Figures 7f and 7g with amplitudes of ~14 and ~6 nT, respectively, similar to the northern oscillation amplitudes in the northern auroral and subauroral regions in Figures 6a and 6b, and with similar negative phase deviations $\Delta_\varphi \approx -10°$ and $-25°$. However, the fitted amplitudes fall to values significantly less than the uncertainties in the southern B and D ring data in Figures 7h and 7i, though reappearing above uncertainties at augmented amplitudes ~8 nT and near-zero phases in scattered data on field lines inside the D ring in Figure 7j.

Figures 7a–7e similarly show the northern hemisphere data plotted versus southern system phase, which due to the presence of the northern system oscillations demonstrated in Figures 6a–6e are more scattered than when plotted versus northern phase, but still reveal the presence of southern oscillations with amplitudes larger than uncertainties throughout, typically ~60–70% of the northern amplitudes in the same bin, and with generally increasingly negative phase deviations on the inner region field lines. An augmentation in amplitude from ~3 nT in the B and D ring regions to ~6 nT inside the D ring is again observed. The southern system amplitudes in the southern hemisphere are somewhat greater than those in the northern hemisphere on auroral and subauroral field lines (compare Figures 7f and 7g with Figures 7a and 7b), as expected. However, the amplitudes on B and D ring field lines in the southern hemisphere are unexpectedly smaller than those in the northern hemisphere, being consistent with zero (Figures 7h and 7i and Figures 7c and 7d), although the amplitudes become comparable on field lines inside the D ring (Figures 7j and 7e).

As for the northern PPO data in Figure 6 discussed in section 4.1.1, consideration of the amplitudes expected from fits to random data yields conclusions consistent with those discussed above. That is, in the majority of cases for which the fitted amplitudes are significantly larger than the estimated uncertainties (Figures 7a–7g and 7j), they are also larger than those expected for comparable sets of random data (with equal RMS about the mean). In Figures 7h and 7i, however, for which the fitted amplitudes are less than the estimated uncertainties, the amplitudes are also similar to those expected from fits to random data.

4.1.3. Northern and Southern PPO Modulations in Northern Hemisphere Poloidal Field Data

A similar overall exposition could also be made for the residual colatitudinal and radial field components. However, here we confine ourselves to showing that these components also generally show oscillations related to the two PPO systems on the inbound passes in the northern (and prenoon) hemisphere, where these effects were clearest in the azimuthal field data in Figure 6 (see also Figures 4 and 5). We then summarize overall in section 4.2. In Figures 8 and 9 we show a selection of these data in a similar format to Figures 6 and 7, using the same mapped northern ionospheric colatitude bins spanning from the auroral region to inside the D ring. Figures 8a–8e and 8f–8j show the northern hemisphere residual colatitudinal and radial field component data, respectively, plotted versus the northern PPO phase, while Figures 9a–9e and 9f–9j show the same data plotted versus the southern PPO phase. The colatitudinal and radial component data

are shown fitted to equations (6b) and (6a), respectively. Examination of Figures 8a–8e clearly shows the presence of northern PPO oscillations in the northern colatitudinal field data, with amplitudes that decline modestly from ~5 nT in the auroral region, through ~4 nT in the subauroral region to ~3 nT in the B, D, and intra-D ring regions. These values are approximately ~60% those of the corresponding amplitudes of the azimuthal components in Figures 6a–6e. The phase deviations are ~−55° in the auroral region, declining to ~−65° and −70° in the subauroral and B ring regions, respectively, similar to the azimuthal field values, before rising slightly again to −55° in and inside of the D ring region (with uncertainties ~±15°). The corresponding results for the radial field component in Figures 8f–8j show the presence of northern PPO oscillations of ~2-nT amplitude in both the auroral and subauroral regions, with phase deviations of $\Delta_r \approx -60°$ and ~−75°. The fitted amplitudes then decline to ~0.5–1 nT near and beyond the limit of detectability and consistent with zero in the B, D, and intra-D ring regions.

When plotted versus the southern phase in Figure 9, we find for the colatitudinal component in Figures 9a–9e that there is no detectable oscillation above uncertainties in the northern auroral and B ring regions, while the data in the subauroral, D and intra-D ring regions show oscillations with amplitudes ~2.5 nT. The phase deviations are $\Delta_\theta \approx -30°$ in the subauroral region, declining to ~−90° on and inside D ring field lines. For the radial field component data in Figures 9f–9j noisy fits with amplitudes above uncertainty estimates are obtained in the northern subauroral and B ring regions, and inside the D ring, with amplitudes ~1 nT in the subauroral and B ring regions, and ~2 nT inside the D ring, all with large positive phase deviations and large uncertainties. Overall, while the status of the results for the radial component in the inner ring-related regions may be unclear, with typical small amplitudes ~1 nT and phase deviations with large uncertainties typically of more than ~±45°, the colatitudinal component data clearly show the presence of both northern and southern system oscillations in almost all regions of northern hemisphere data.

4.2. Overview of PPO Modulation Results

We now provide an overview of the amplitude and phase data derived from the fits to equation (6) throughout the regions traversed, representative examples of which were shown in Figures 6–9.

4.2.1. Northern PPO Modulations

Figure 10 shows results for the fits to the data versus northern PPO phase, exemplified in Figures 6 and 8, where Figure 10a shows the fit amplitudes B_{i0} and Figure 10b the corresponding phases Δ_i. Results for the mean fields $\overline{\Delta B_i}$ will be overviewed in section 6. Northern hemisphere inbound data are shown on the left and southern hemisphere outbound data on the right, both being plotted versus mapped northern ionospheric colatitude, with an entirely equivalent scale of mapped southern ionospheric colatitude being shown at the top of the plot. As indicated in section 4.1, the northern hemisphere data span the range from 15.6° northern ionospheric colatitude on the left of the plot to 72° at the center marked by the vertical black dotted line (17.3° to 81.8° southern ionospheric colatitude), while the southern hemisphere data span the range from 17.0° northern ionospheric colatitude on the right of the plot also to 72° at the center (18.8° to 81.8° southern ionospheric colatitude). The other vertical lines follow the format in Figures 4 and 5, delineating the inner auroral, subauroral, ring, and intraring field regions.

The data shown by the red, green, and blue circles in Figure 10 correspond to the r, θ, and φ field components, respectively, where to avoid clutter only representative uncertainty estimates are displayed. The plotted symbol type also gives an indication of fit quality, with solid triangles indicating fit amplitudes that are more than twice the estimated uncertainty, solid circles amplitudes between once and twice the uncertainty, and open circles fit amplitudes that are smaller than the uncertainty, which we thus consider consistent with zero within the uncertainties (see also the discussion in section 4.1.1). The open circle data have nevertheless been retained in the plot since they give an indication of an upper limit to the amplitudes in the regimes concerned, within the uncertainties. It can be seen that for the azimuthal component "good" fits (solid symbols) were obtained throughout the northern hemisphere, and in the southern intra-D ring and outer subauroral and auroral regions, but not in the southern main ring region and inner subauroral regions where the fitted amplitudes fall to ~1–2 nT with uncertainties of ~±3 nT (Figure 6). For the colatitudinal component good fits were also obtained throughout the northern hemisphere (Figures 8a–8e), now extending to southern hemisphere ring field lines and inner subauroral region. For the radial component good fits with amplitudes ~1–2 nT were obtained in the northern auroral, subauroral, and outer ring regions (Figures 8f–8h), together with the outer subauroral and auroral regions in the southern hemisphere.

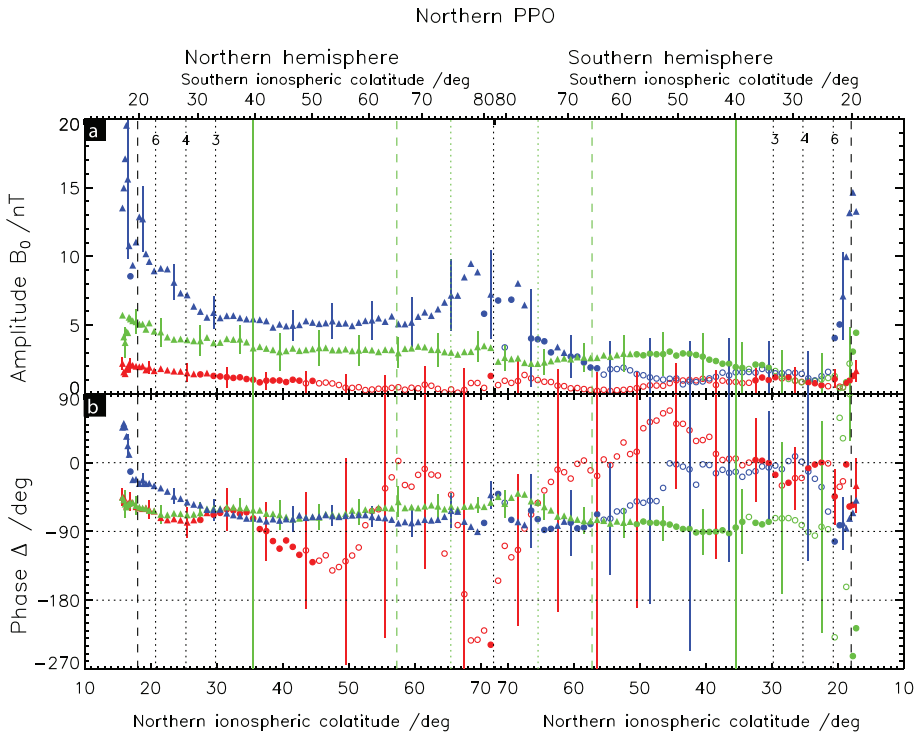

Figure 10. Overview of sinusoid fit results to the proximal periapsis pass data organized by northern PPO phase Ψ_N, where Figures 10a and 10b show the fit amplitudes B_{i0} and corresponding phase deviations Δ_i, respectively (equation (6)). Inbound northern hemisphere data are shown on the left, and outbound southern hemisphere data on the right, both plotted versus mapped northern ionospheric colatitude, with the central vertical black dotted line marking the point where the spacecraft reached the largest useable mapped colatitudes in both northern and southern ionospheres. An equivalent mapped southern ionospheric colatitude scale is shown at the top of the plot. The other vertical lines follow the format in Figures 4 and 5. The red, green, and blue circles correspond to the r, θ, and φ field components, respectively, with representative error bars displayed. The solid and open circles indicate fits with amplitudes larger or smaller, respectively, than the estimated uncertainties, while the solid triangles indicate fits with amplitudes more than twice the uncertainties.

In more detail, it can be seen that in much of the data in Figure 10a the azimuthal component exhibits the largest amplitudes, with values ~10–20 nT in the northern auroral region, falling across the northern subauroral region to ~5 nT on field lines mapping to the outer edge of the A ring, and remaining at similar values to the outer edge of D ring field lines. The amplitudes then rise to peak at ~8–9 nT inside of the D ring, though with large uncertainties. In the southern hemisphere the amplitudes fall to ~2–3 nT on southern D ring field lines, before falling to values consistent with zero throughout the main ring and inner subauroral regions, then rising rapidly to ~15 nT in the southern auroral region. The corresponding phase deviations fall rapidly from positive ~+50° values in the northern auroral region across zero to plateau at ~ − 25° in the northern inner auroral and outer subauroral regions, before falling increasingly gradually across the inner subauroral and main ring regions to ~−60° to ~−80° on and inside D ring field lines.

A notable feature of these results (as well as for the azimuthal field oscillations of the southern system discussed in section 4.2.2 below), is the elevation of the azimuthal component oscillation amplitudes on and inside of D ring field lines, albeit with enhanced estimated uncertainties in this region. A significant contributor to these uncertainties is evidently the highly variable but largely positive azimuthal fields associated with the intra-D ring interhemispheric current system mentioned in section 1.4 (Dougherty et al., 2018; Khurana et al., 2018), the variations of which have been shown to be unrelated to the PPO phases (Provan, Cowley, et al., 2019). The peak magnitude of these perturbations is typically ~20 nT, compared with ~5 nT for the PPO azimuthal component oscillations in the ring region shown in Figure 10. The question then arises as to whether the presence of such large-amplitude noise superposed on the PPO oscillations specifically on and inside D ring field lines could skew the fitted amplitudes to the larger values shown in

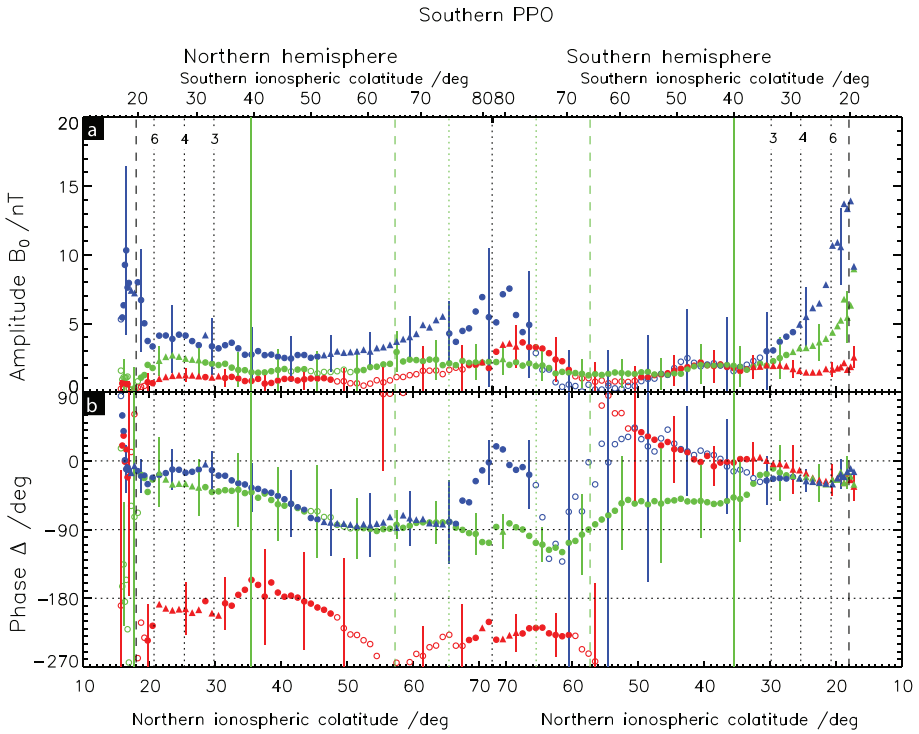

Figure 11. Same as for Figure 10 but showing an overview of sinusoidal fit results to the proximal periapsis pass data organized by southern PPO phase Ψ_S.

Figure 10 (and for the southern system in Figure 11 introduced below). This issue is investigated quantitatively in Appendix B using a simulated data set intended to mimic conditions on the proximal passes. It is shown that at the levels of noise present on the proximal passes, the amplitudes may become somewhat scattered about the true amplitude, but are not in general significantly elevated in value in the manner seen in Figure 10 (and Figure 11). It is further shown that the phases will also scatter about the true values due to this effect, generally by a few tens of degrees.

Turning now to the colatitudinal component data in Figure 10, it is first seen that the northern system amplitudes in the northern hemisphere are approximately half those of the azimuthal component, falling more gradually from ~5 nT in the northern auroral region to ~3 nT in the central ring regions north and south. The amplitudes then fall to smaller less well determined values in the southern subauroral region. The phase deviations are ~−50° in the northern auroral region, somewhat more negative than for the azimuthal component, and lie typically between ~−60° and ~−80° in the northern and southern ring regions, similar to the azimuthal component.

The radial component data in Figure 10 only provide consistent results with amplitudes larger than uncertainties in the northern auroral, subauroral, and outer ring regions, with amplitudes falling from ~2 nT in the auroral region to ~1 nT in the outer ring region. These values are again roughly half those of the colatitudinal component, and thus about a quarter of those of the azimuthal component. The phase deviations are generally consistent with those of the colatitudinal component within uncertainties in these regions, and also largely with the azimuthal component within the inner northern subauroral region. Elsewhere, the fitted amplitudes fall to ~1 nT or less, with scattered essentially undetermined phases having large uncertainties.

Overall, comparison of Figure 10 with the corresponding cos and sin plots for the northern PPO system in Figure 4 shows that the fit results discussed here directly follow the behaviors visually identified in the latter figure, as discussed in section 3.2. The same is true of the southern PPO results shown previously in Figure 5, as we now discuss.

4.2.2. Southern PPO Modulations

Figure 11 shows corresponding results for fits to the data plotted versus southern PPO phase, exemplified in Figures 7 and 9. For the azimuthal field component, peak amplitudes of ~14 nT are found in the southern auroral region, falling rapidly across the outer southern subauroral region to ~3 nT in the inner subauroral region. The phase deviations are approximately constant at ~−25° in these regions. The amplitudes then become less than estimated uncertainties on innermost subauroral and southern ring field lines, as for the northern PPO amplitudes in this regime, but then rise again to ~4–7 nT, larger than the still rather large uncertainties, inside the D ring region both north and south of the equator. Phase deviations in the latter region vary between ~−50° and ~+20°, with rather large uncertainties. Amplitudes are ~3 nT on northern main ring field lines, unexpectedly somewhat larger than in the corresponding region in the southern hemisphere, rising modestly toward subauroral values of ~3–5 nT, then peaking at ~7–10 nT in the northern auroral region. The phase deviations in the northern hemisphere rise from ~−80° on ring field lines back to ~−10° to −20° on northern outer subauroral and equatorward auroral region field lines, before again exhibiting positive values at the smallest colatitudes sampled, similar to the northern system phase deviations in Figure 10b. It is thus notable that the phase deviations show good consistency north and south on subauroral and auroral flux tubes despite the fact that the corresponding data on the leftmost and rightmost sides of the plot are separated in time by approximately a quarter of a PPO cycle, corresponding to a change in PPO phase of ~90°, and ~12 hr of LT (Figure 3), corresponding to an opposite change in PPO phase of ~180°. For the corresponding northern PPO azimuthal component data in Figure 10, the phase deviations on outer subauroral field lines are ~−20° to ~−30° in the northern hemisphere, similar to the southern PPO system, but remain near −50° to −80° in the southern hemisphere.

The colatitudinal component data in Figure 11 show related behavior, with amplitudes falling rapidly from a peak of ~9 nT on southern auroral field lines to ~2 nT on outer subauroral field lines and in the main ring region. Phase deviations fall from ~−20° on southern auroral and outer subauroral field lines, closely similar to the azimuthal component in these regions, to values varying about ~−90° on inner southern ring field lines, though with large uncertainties. The amplitudes remain at ~1.5–2.5 nT on and inside of D ring field lines, with phases generally within a few tens of degrees of ~−90°, and remain at such values on main ring and inner subauroral field lines in the northern hemisphere, with phase deviations that rise gradually back to ~−10° to ~−30° in the subauroral region, essentially equal to the azimuthal component phase deviations within estimated uncertainties.

For the radial component, the amplitudes are ~1–2 nT in the southern auroral, subauroral, and outer ring region field lines, with phase deviations initially close to those determined from the colatitudinal and azimuthal components, though drifting toward positive values with large uncertainties in the southern ring region. The amplitudes then rise once more to measureable values ~2–4 nT on intra-D ring field lines in the southern but not in the northern hemisphere. The phases in the southern intra-D ring region are ~−180° with large uncertainties, thus apparently opposite to the phase deviations of the similarly equatorially enhanced azimuthal field oscillations. The radial component phases then remain scattered about such values in the northern hemisphere, with small amplitudes ~1 nT in the outer ring and subauroral regions, though returning to values scattered around ~−20°, again consistent with the colatitudinal and azimuthal field component values, in the northern auroral region data.

Comparing the data from the northern and southern phase analyses in Figures 10 and 11, it can be seen that, with few exceptions, consistent results concerning the variation of the PPO oscillation amplitude and phase were obtained for well determined data (solid symbols) throughout the diverse physical regimes traversed on the proximal orbits. This comment applies both to the behavior of differing field components for the individual PPO systems, and to the comparative behavior of the two PPO systems, thus supporting the discussion of the validity of the well determined data in section 4.1.1.

Having thus overviewed the data for both PPO systems, we now briefly comment on the effect of cross-modulation due to the general dual presence of the two PPO systems, that is, the effect of the modulations due to one PPO system on the determination of the amplitude and phase of the other. As shown in Appendix A, for the specifics of the proximal data set, such cross-modulation results in spurious variations in amplitude of typically ~10% of the amplitude of the "interfering" system. Given the results in Figures 10 and 11, therefore, generally showing oscillations of comparable magnitude for the two systems on given field

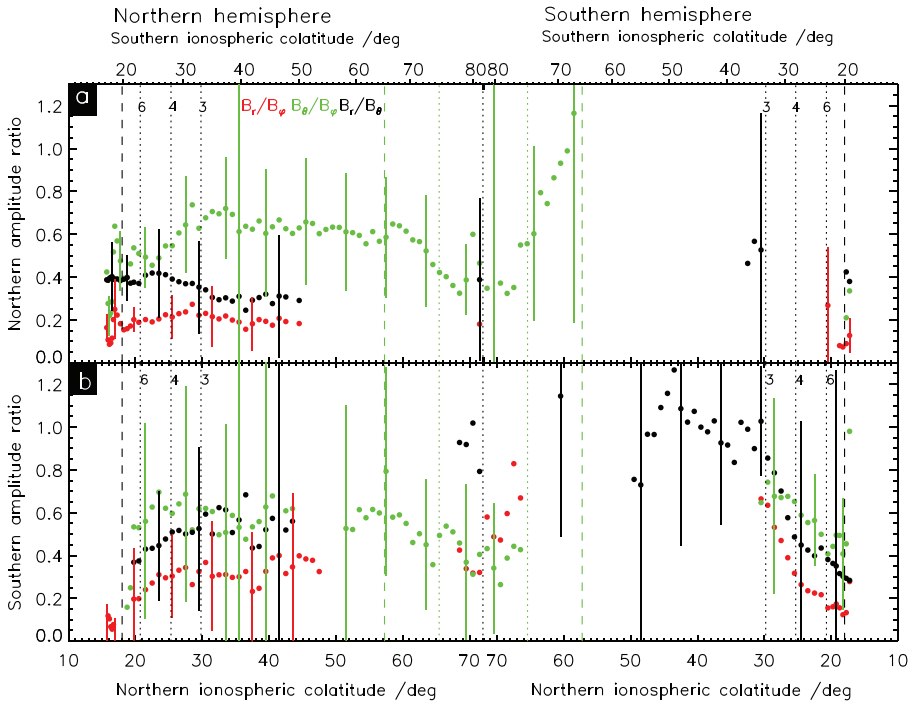

Figure 12. Plot of the PPO amplitude ratios of the three field components in a format similar to Figures 10 and 11. The B_r/B_φ and B_θ/B_φ ratios are shown by the red and green circles, respectively, while their quotient, the B_r/B_θ ratio, is shown by the black circles. Values are shown only for cases in which both amplitudes in the ratio are larger than their estimated uncertainties.

lines, it is evident that the variations due to this effect will generally be minor, corresponding to ~10% of the amplitudes shown, with related variations in oscillation phase of ~10°.

4.2.3. Field Component Amplitude Ratios

We now look at some aspects of the results in Figures 10 and 11 in more detail, and begin by examining the relative amplitudes of the PPO oscillations in the three field components. In section 5.2 these will be compared with related results obtained previously from equatorial data. The amplitude ratios are shown in Figures 12a and 12b for the northern and southern PPO systems, respectively, in a format related to Figures 10 and 11. The red and green circles show the ratios of the radial and colatitudinal component amplitudes relative to the azimuthal component amplitude, respectively, while the black circles indicate the quotient of these values giving the ratio of the amplitudes of the radial and colatitudinal components (as indicated in the top panel). Values are shown only for cases in which both amplitudes in the ratio are larger than uncertainties, even in which case the propagated uncertainties are generally quite large.

For the northern PPO system in Figure 12a it is seen that these reasonably well determined ratios are confined mainly to the northern hemisphere, with near-constant values ~0.2 for B_r/B_φ and ~0.65 for B_θ/B_φ, with a consequent value of ~0.35 also for B_r/B_θ. Such values are continuous across the inner subauroral and outer northern ring field region, while the B_θ/B_φ ratio moves to smaller values ~0.4–0.5 in the inner northern ring region and inside the D ring region. Well determined values in the southern hemisphere are mainly confined to the auroral region where the ratios relative to the azimuthal component are smaller with ~0.1 for B_r/B_φ and ~0.2–0.3 for B_θ/B_φ.

For the southern PPO system in Figure 12b, the B_r/B_φ and B_θ/B_φ ratios rise from generally small values in the northern auroral and outer subauroral regions to ~0.3–0.4 for B_r/B_φ in the inner subauroral and ring regions, and to values ~0.5–0.6 for B_θ/B_φ. In the southern hemisphere the B_r/B_φ and B_θ/B_φ amplitude ratios are again smaller in the auroral region, ~0.15 for B_r/B_φ and ~0.45 for B_θ/B_φ, then rising toward larger values ~0.7 in the inner subauroral region as the azimuthal component amplitudes rapidly fall.

4.2.4. Northern and Southern System Amplitude Ratios

We also enquire what may be deduced from the results in Figures 10a and 11a about the relative amplitudes of the two PPO systems during the proximal orbit interval. From section 3.1 we recall that Provan et al. (2018) inferred from consideration of the off-equatorial nightside oscillation amplitudes that the northern system was the stronger of the two, but not by a large factor, with an estimated north/south amplitude ratio k of ~1.4. Hunt, Provan, Cowley, et al. (2018) had previously deduced a north/south amplitude ratio of ~1.3 for the prior interval of F ring orbit data. The essential difficulty in deducing a value of k from the proximal periapsis data set lies in the off-equatorial nature of the data, since the north/south ratio k applies strictly only to the simultaneously observed amplitudes in dual-modulated equatorial data where it can be assumed that the field is equally perturbed from both polar hemispheres, such that the deduced amplitude ratio is reflective of the strength of the two systems overall. The prior analyses of Hunt et al. (2015), Hunt, Provan, Cowley, et al. (2018) and Bradley, Cowley, Provan, et al. (2018) have also shown that the azimuthal component PPO amplitudes fall significantly along field lines between the generating and opposite ionospheres, a fact reflected, that is, in the amplitude profile of the northern PPO system in Figure 10a. At the same time, for the southern PPO system in Figure 11a the southern amplitudes in the main ring and inner subauroral regions are unexpectedly smaller than those in the northern hemisphere, suggestive of an inbound/outbound difference in amplitudes which we here presume is associated with a weak LT gradient in the dayside amplitudes (Figure 3). We take both effects into approximate account in the following considerations.

We first assume that the inbound and outbound observation points on a given flux shell (i.e., given mapped ionospheric colatitude) represent essentially equivalent points relative to the two hemispheric PPO sources. We note that mapping azimuthal amplitudes to the equator from two such positions using $\rho B_\varphi \approx$ const along a field line (see discussion in section 4.1 and section 5) would be by essentially the same ρ ratio factor (see Figure 2). For a given field line, we thus take the amplitude of the northern system in the south relative to the northern system in the north, and the southern system in the north relative to the southern system in the south to have the same ratios R, expected to be somewhat less than unity. Ratio R may vary with colatitude from region to region, however, such that in general it may be regarded to be a function of mapped ionospheric colatitude. Allowing for a small gradient in amplitude with azimuth (LT) across dayside field lines, however, we take both northern and southern system outbound amplitudes to be a factor F times the inbound amplitudes on the same flux shell, which may also vary with flux shell (i.e., mapped ionospheric colatitude) given the differing ranges of LT spanned between the inbound and outbound orbit portions (Figure 3). Denoting the amplitudes of the northern and southern PPO systems by "N" and "S," respectively, and the northern and southern hemispheres of observation by "NH" and "SH," respectively, we then have the following relations between the inbound (northern/prenoon) and outbound (southern/postnoon) amplitudes

$$B_{N/SH}(\theta_i) = R(\theta_i)F(\theta_i)B_{N/NH}(\theta_i), \tag{7}$$

and

$$B_{S/NH}(\theta_i) = \frac{R(\theta_i)}{F(\theta_i)}B_{S/SH}(\theta_i). \tag{8}$$

Eliminating $F(\theta_i)$ between these equations yields

$$R(\theta_i) = \sqrt{\frac{B_{N/SH}(\theta_i)B_{S/NH}(\theta_i)}{B_{N/NH}(\theta_i)B_{S/SH}(\theta_i)}}, \tag{9}$$

which involves the ratios of the amplitudes of the northern system in the southern hemisphere to the northern system in the northern hemisphere, and the southern system in the northern hemisphere to the southern system in the northern hemisphere, while eliminating $R(\theta_i)$ yields

$$F(\theta_i) = \sqrt{\frac{B_{N/SH}(\theta_i)B_{S/SH}(\theta_i)}{B_{N/NH}(\theta_i)B_{S/NH}(\theta_i)}}, \tag{10}$$

which involves the ratios of the southern outbound amplitudes to the northern inbound amplitudes for both systems. The north/south amplitude ratio k can then be expressed, for example, as

$$k = \frac{F(\theta_i)B_{N/NH}(\theta_i)}{B_{S/SH}(\theta_i)} = \sqrt{\frac{B_{N/NH}(\theta_i)B_{N/SH}(\theta_i)}{B_{S/NH}(\theta_i)B_{S/SH}(\theta_i)}}, \quad (11)$$

which involves the ratios of the northern and southern systems in the northern hemisphere and the northern and southern systems in the southern hemisphere.

The above ratios are plotted versus mapped northern ionospheric colatitude in Figure 13, with an equivalent scale of southern ionospheric colatitude shown at the top of the figure. Similar to Figure 12, we only consider values for which all four amplitudes for a given field component in a given bin have amplitudes larger than the estimated uncertainties. Even in these cases, however, the propagated uncertainties can be very large, so we also restrict attention to the regions and components with the largest and best determined amplitude values, specifically to the colatitudinal component on and inside D ring field lines, and the azimuthal component in the outer subauroral and auroral field lines.

Results are plotted in Figure 13 on separate expanded colatitude scales, where ratios R, F, and k are shown in Figures 13a–13c for the outer subauroral and auroral regions, and in Figures 13d–13f for the D ring region. In the latter region all the ratio values are consistent with unity within uncertainties. However, the R values in Figure 13d are generally slightly smaller than unity as expected, with a mean value of ~0.89. The F values in Figure 13e are also slightly smaller than unity with a mean of ~0.85, indicating that the oscillations have slightly smaller amplitude postnoon than prenoon. The north/south PPO amplitude ratio k values are also larger than unity, with a mean of ~1.32.

For the auroral/subauroral region, the R values in Figure 13a generally have a rather smaller value than inside the D ring as might also be expected, with a mean of ~0.69. Thus of the PPO-related fields and currents generated in a given ionosphere, north or south, somewhat over half propagates across the equatorial region to the opposite ionosphere, as previously deduced by Bradley, Cowley, Provan, et al. (2018) (see also Hunt et al., 2015; Hunt, Provan, Cowley, et al., 2018). For ratio F in Figure 13b the auroral/subauroral values are now somewhat greater than unity with a mean of ~1.34, meaning that in this regime postnoon outbound amplitudes are greater than prenoon inbound amplitudes by approximately this factor. The ratios k derived from the auroral/subauroral data in Figure 13c are again consistent with values a little larger than unity, in this case with a mean of ~1.22, consistent with the near-equatorial data in Figure 13f. These results are thus in approximate accord with the findings of Provan et al. (2018) from the proximal orbit nightside data, that the northern system was the stronger of the two during the proximal orbit interval, but not by a large factor. A reasonable overall k value indicated by the proximal data, taking account of both the above estimates, is ~1.25.

5. Mapping PPO Fields to the Ionosphere and Equator: Comparison With Previous Results

We now relate the results summarized in Figures 10 and 11 to those derived previously from earlier Cassini data, obtained both at high latitudes over the auroral regions and near the equatorial plane. Specifically, we compare with the colatitudinal profiles of the PPO-related azimuthal fields and currents derived from preequinox and postequinox nightside high-latitude data by Hunt et al. (2014, 2015) and Bradley, Cowley, Provan, et al. (2018), and with dayside F ring orbit data derived by Hunt, Provan, Bunce, et al. (2018). We also compare with the three-component equatorial profiles of the then-dominant southern PPO system derived by Andrews, Cowley, et al. (2010) from preequinox data, as well as with the quasi-dipolar "core" region (radial distances ~4–12 R_S) mean equatorial amplitudes quoted by Andrews et al. (2012) and Provan et al. (2013, 2016) using data from various mission phases.

5.1. Mapping Azimuthal Component PPO Amplitudes to the Ionosphere

As indicated in section 4.1, quantitative comparison of the perturbation fields measured at different positions along magnetospheric field lines is possible for the azimuthal field component, for which in the quasi-axisymmetric approximation $\rho B_\varphi \approx$ constant along a given field line (see Appendix B2 of Hunt et al. (2014)), assuming negligible cross-field current flow between the points concerned. The measured azimuthal field amplitudes $B_{\varphi 0}$ for a given PPO system in Figures 10a and 11a can thus be mapped along field lines into the ionosphere using

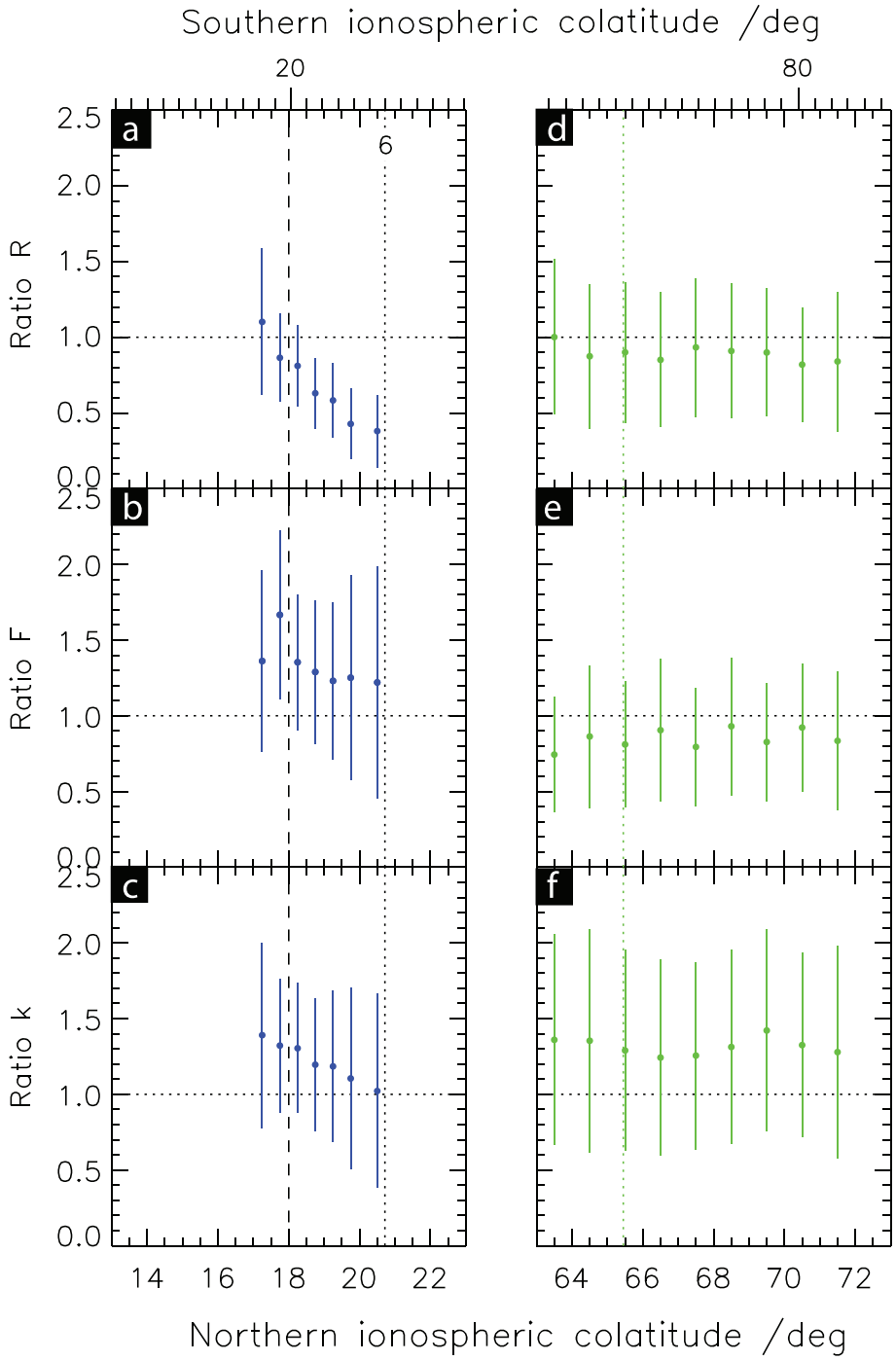

Figure 13. Plots of the PPO amplitude ratios *R*, *F*, and *k* defined by equations (9)–(11), respectively, are shown versus mapped northern ionospheric colatitude in two restricted colatitude regimes corresponding to auroral and outer subauroral field lines in Figures 13a–13c (northern colatitudes 13°–23°), and field lines in and inside the D ring in Figures 13d–13f (northern colatitudes 63°–73°). An equivalent scale of southern ionospheric colatitude is shown at the top of these panels. As in Figures 10 and 11 the black vertical dashed line in Figures 13a–13c marks the equatorward boundary of the auroral region, while the green dotted line in Figures 13d–13f indicates the inner edge of D ring field lines. Only results for the azimuthal field component (blue) are shown in Figures 13a–13c, and for the colatitudinal component (green) in Figures 13d–13f, corresponding to the best determined/largest field components in these regimes. Values are shown only for cases in which all four amplitudes contributing to a given ratio have amplitudes larger than the uncertainty. Parameter *R* (Figures 13a and 13d) relates to the ratio of the amplitudes observed on a given field line between the generating and opposite hemispheres (opposite/generating), parameter *F* (Figures 13b and 13e) to the ratio of amplitudes observed inbound in the prenoon sector and outbound in the postnoon sector (postnoon/prenoon), and *k* (Figures 13c and 13f) to the ratio of amplitudes of the two PPO systems (north/south).

$$B_{\varphi 0\ i} \approx \left(\frac{\rho}{\rho_i}\right) B_{\varphi 0}, \tag{12}$$

where ρ_i is the perpendicular radial distance in the ionosphere of the field line passing through the measurement point at perpendicular radial distance ρ. The value of ρ at the measurement point in equation (12) varies slightly, of course, over the data points contributing to a given mapped ionospheric colatitude bin (Figure 2), and so was first averaged individually over each contributing Rev, and then over all the Revs, thus ensuring that the data from each Rev is given equal weight, as in the sinusoidal fits themselves. It may also be noted that the mapped field values will be slightly different for a given measured amplitude $B_{\varphi 0}$ depending on whether it is mapped to the northern or southern ionosphere due to the axial quadrupole asymmetry in the planetary field. However, given the nature of the trajectory shown in Figure 2, it is evident in the present case that the values derived from the northern inbound data should provide excellent approximations to the northern ionospheric values, while the southern outbound data should similarly provide excellent approximations to the southern ionospheric values. Accordingly, we map the northern inbound data in Figures 10a and 11a to the northern ionosphere, plotted versus mapped northern ionospheric colatitude, and the southern outbound data to the southern ionosphere, plotted versus mapped southern ionospheric colatitude, following the presentational procedure adopted in the related papers analyzing high-latitude field data by Hunt et al. (2014, 2015), Hunt, Provan, Cowley, et al. (2018) and Bradley, Cowley, Provan, et al. (2018).

The northern hemisphere northern and southern system azimuthal component amplitudes mapped to the northern ionosphere are shown are shown by the blue symbols (coded as in Figures 10a and 11a) in Figures 14a and 14c, respectively, while the southern hemisphere northern and southern system amplitudes mapped to the southern ionosphere are similarly shown in Figures 15a and 15c, respectively. Equivalent scales of colatitude in the opposite hemisphere are shown at the top of each figure. We note that we have used log scales of mapped ionospheric colatitude in both cases in order to expand the scale in the auroral region where the fields and currents vary most rapidly. We also note that the field amplitude scale for the southern hemisphere values in Figures 15a and 15c has been increased compared with that for the northern data in Figures 14a and 14c in order to better display these data. The current amplitude scales, however, are the same in the two plots. The set of vertical lines in these figures correspond to those shown previously, for example, in Figures 10 and 11, to which the northern and southern hemisphere OCBs of Jinks et al. (2014) have been added in Figures 14 and 15, respectively, shown by the black dot-dashed lines.

In Figure 14a it can be seen that in the northern ionosphere the amplitude of the mapped northern PPO oscillations rises to a peak of ~70 nT at ~16° colatitude, falls to ~35 nT in the outer subauroral region, and then near-monotonically across the subauroral and main ring regions to ~7.5 nT in the inner main ring region, before rising modestly to peak again at ~10 nT in the intra-D ring region. The amplitude of the southern PPO system in the northern ionosphere in Figure 14c shows similar behavior, except that the values are smaller by a factor of ~2, peaking at ~35 nT at ~16° colatitude in the auroral region, falling to a minimum of ~3 nT in the inner main ring region, and then peaking modestly again at ~7 nT in the intra-D ring region. In the southern hemisphere the northern PPO amplitude in Figure 15a falls rapidly across the outer subauroral region from ~40 nT in the inner auroral region to poorly determined values less than ~5 nT in the inner subauroral and main ring regions, before rising somewhat again to peak at ~7 nT in the intra-D ring region. The southern PPO amplitude in the southern hemisphere in Figure 15c peaks at ~35 nT in the inner auroral region before falling more gradually to ~5 nT across the subauroral region, and then to poorly determined smaller values in the ring region. The amplitude then rises again to peak at ~8 nT in the intra-D ring region.

In previous studies of the high-latitude azimuthal fields cited above, however, results have been expressed in terms of the horizontal meridional (principally Pedersen) current per radian of azimuth, I_m, flowing in the ionosphere at the feet of the field lines, such that the related field-aligned currents may then be discussed. From Ampère's law the amplitude of the current per radian of azimuth is given by

$$I_{m0} = \frac{\rho_i B_{i\ \varphi 0}}{\mu_o} \approx \frac{\rho B_{\varphi 0}}{\mu_o}, \tag{13}$$

where we note that the value depends only on locally measured quantities. Physically, I_m is directed from south to north where B_φ is positive and from north to south where B_φ is negative, opposite in the two

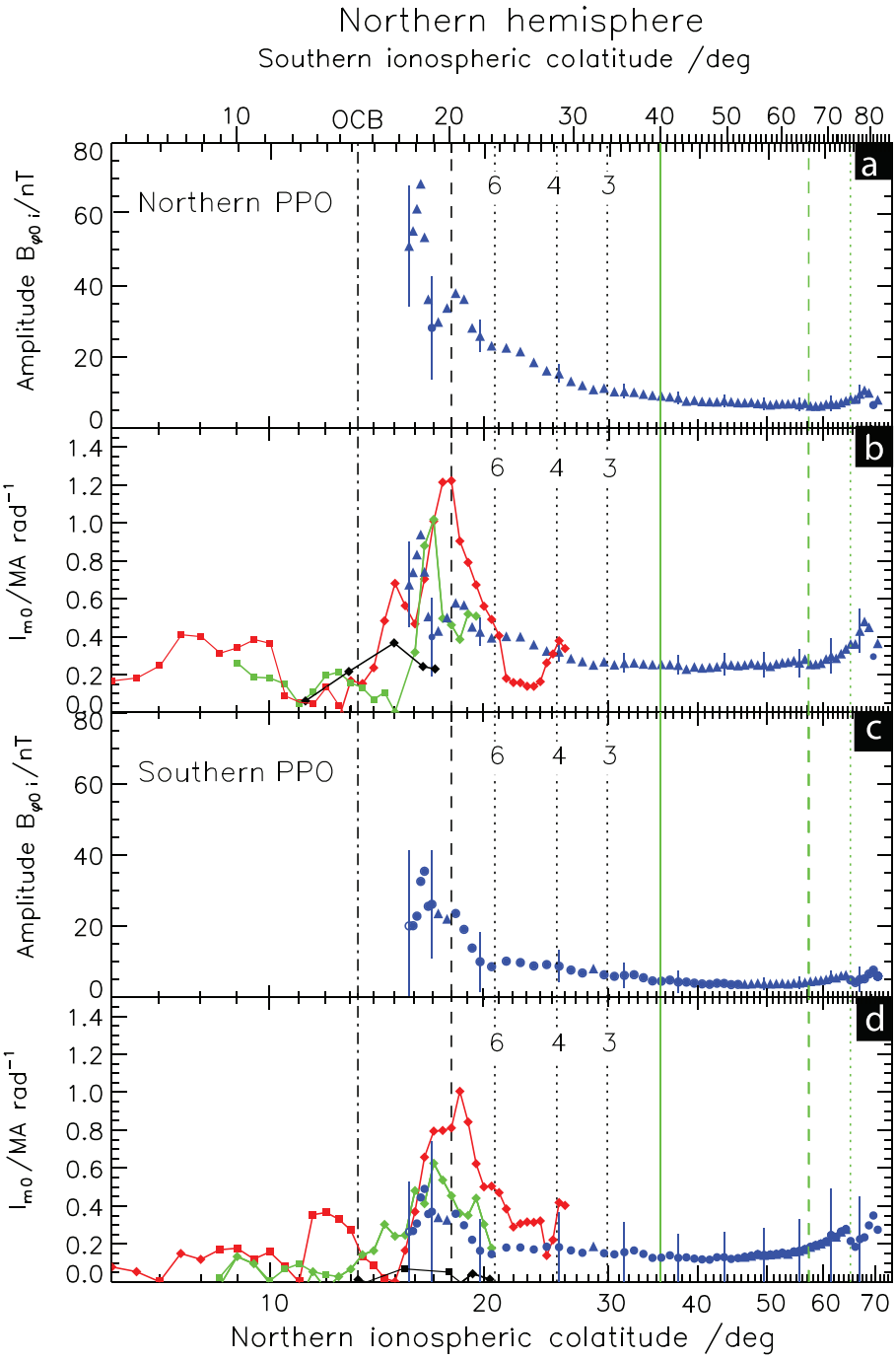

Figure 14. Plots of the northern and southern PPO system azimuthal component oscillation amplitudes in the northern hemisphere shown in Figures 10a and 11a, respectively, mapped along model field lines into the northern ionosphere using equation (12), and plotted versus northern ionospheric colatitude on a log scale (blue symbols). An equivalent scale of southern ionospheric colatitude is shown at the top of the plot. The northern and southern system amplitudes are shown in the same blue symbol format as in Figures 10a and 11a in Figures 14a and 14c, respectively, while the corresponding meridional ionospheric currents derived using equation (13) are shown in Figures 14b and 14d, respectively. Color-coded meridional current amplitude profiles derived from previous studies of high-latitude data are shown by diamonds and squares. The red data are those determined by Hunt et al. (2015) from high-latitude passes in 2008 (their Figures 7b and 7c), the green data are those determined by Bradley, Cowley, Provan, et al. (2018) from high-latitude passes in 2012–2013 (their Figures 11b and 11c), and the black data are those determined by Hunt, Provan, Bunce, et al. (2018) from F ring orbit passes in 2016–2017 (their Figures 7e and 7f). In each case the diamonds indicate oscillations with equatorial polarization as ~+sin$\Psi_{N,S}$, while the squares indicate oscillations with polar polarization as ~−sin$\Psi_{N,S}$. In addition to showing the same vertical line region identifiers as, for example, in Figures 10 and 11, the black dot-dashed line also indicates the northern OCB of Jinks et al. (2014).

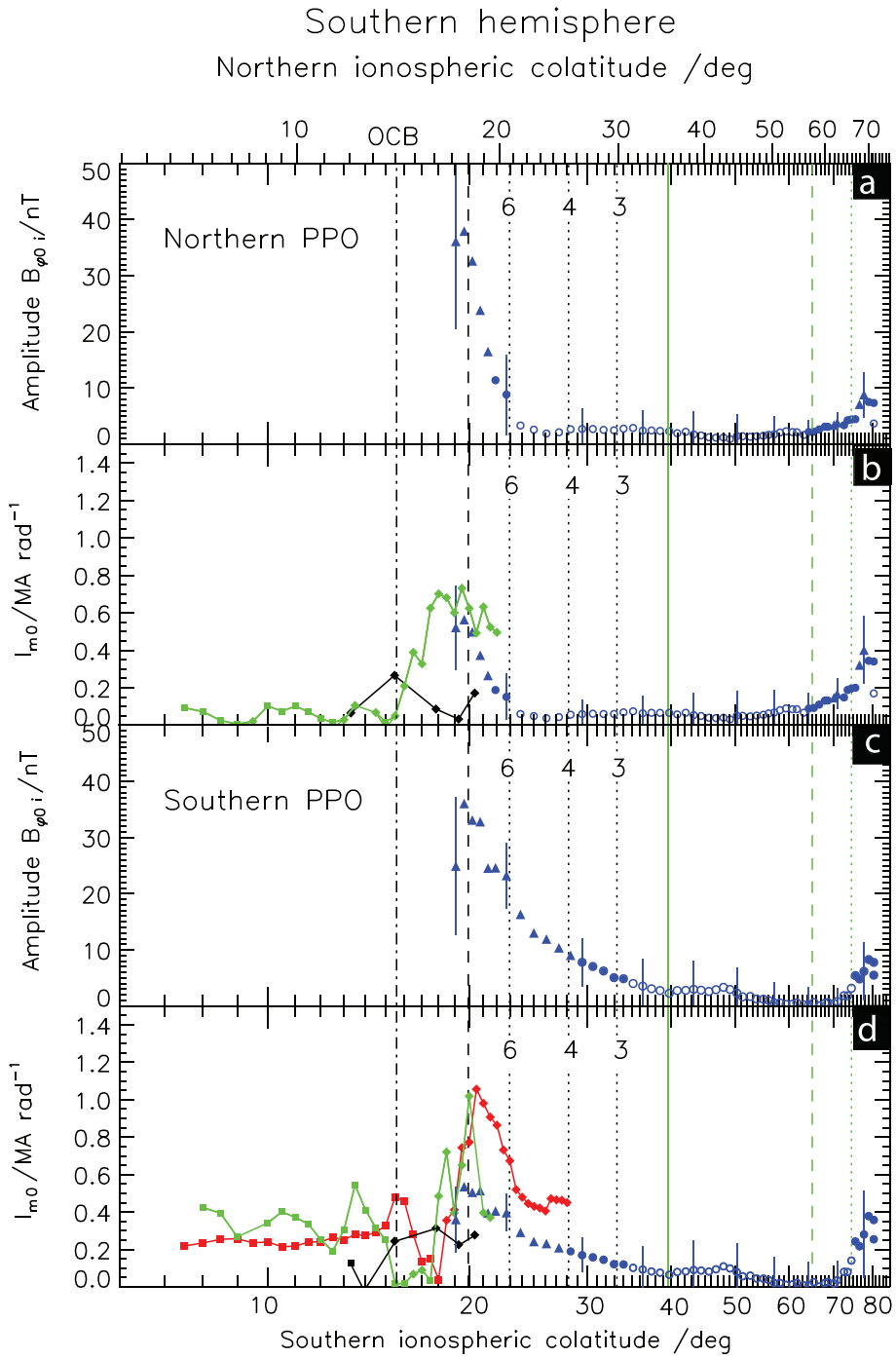

Figure 15. Similar to Figure 14 but showing plots of the northern and southern PPO system azimuthal component oscillation amplitudes in the southern hemisphere mapped along model field lines into the southern ionosphere using equation (12), and plotted versus southern ionospheric colatitude on a log scale (blue symbols coded as in Figures 10a and 11a). An equivalent scale of northern ionospheric colatitude is shown at the top of the plot. In this case the red data are those determined by Hunt et al. (2014) from high-latitude passes in 2008 (see Figure 18c of Bradley, Cowley, Provan, et al. (2018)), the green data are those determined by Bradley, Cowley, Provan, et al. (2018) from high-latitude passes in 2012–2013 (their Figures 12b and 12c), while the black data are those determined by Hunt, Provan, Bunce, et al. (2018) from F ring orbit passes in 2016–2017 (their Figures 7k and 7l). Note that there are no red data in Figure 15b, since no northern period oscillations were discerned in the 2008 southern hemisphere measurements.

halves of the PPO cycle. In Figures 14b and 14d the blue symbols show the meridional current amplitudes for the proximal data for the northern and southern PPO systems in the northern hemisphere, respectively, while Figures 15b and 15d similarly show the current amplitudes for the northern and southern PPO systems in the southern hemisphere, respectively. In the northern hemisphere, the northern PPO current amplitude in Figure 14b peaks at ~0.95 MA/rad in the inner part of the auroral region, falls to ~0.25 MA/rad in the inner main ring region, with a subsidiary maximum of ~0.45 MA/rad in the intra-D ring region. The southern system currents in Figure 14d are similar in form but approximately half the magnitude, falling from a peak of ~0.5 MA/rad in the inner auroral region to ~0.15 MA/rad in the inner subauroral and main ring regions, while the subsidiary maximum in the intra-D ring region is ~0.3 MA/rad.

Since the meridional currents are expressed here (as in the related studies cited above) as currents per radian of azimuth, in the absence of azimuthal PPO-related currents of comparable magnitude, their variation with colatitude relates directly to the field-aligned current flow to and from the ionosphere per radian of azimuth. The falling amplitude values mainly in the subauroral region thus indicate the occurrence of distributed field-aligned currents corresponding to the blue regions in Figure 1, opposite in sense to the main PPO currents in the auroral region corresponding to the red regions in Figure 1. The overall magnitude of these field-aligned currents at the peaks of the PPO cycles are thus ~0.7 MA/rad for the northern system and ~0.35 MA/rad for the southern system, corresponding to the difference between the maximum and minimum values of the current per azimuth, flowing mainly in the inner auroral and subauroral regions rather than the main ring region. The reversed gradients leading to the secondary maxima inside the D ring region are then indicative of a reversed field-aligned current flow of ~0.2 MA/rad for the both systems.

In the southern hemisphere, the northern PPO current amplitude in Figure 15b peaks at ~0.6 MA/rad near the boundary of the inner auroral region as covered by the southern hemisphere proximal trajectories, falls rapidly to ~0.15 MA/rad in the outer subauroral region and to smaller poorly determined values in the inner subauroral and main ring regions, before peaking again at ~0.4 MA/rad in the intra-D ring region. The southern PPO current amplitude in Figure 15d peaks at ~0.5 MA/rad near the boundary of the auroral region falls more gradually to ~0.1 MA/rad in the inner subauroral region, then to smaller ill-determined values in the main ring region, before rising again to peak at ~0.35 MA/rad in the intra-D ring region. The corresponding field-aligned currents in the subauroral and outer ring regions are ~0.45 MA/rad for the northern system and ~0.4 MA/rad for the southern system, while the intra-D ring currents are ~0.25 MA/rad for both systems.

We now compare these amplitude profiles with related results derived previously from analyses of high-latitude azimuthal field data by Hunt et al. (2014, 2015), (Hunt, Provan, Bunce, et al., 2018) and Bradley, Cowley, Provan, et al. (2018). As a consequence of the variable and much larger near-equatorial periapsis of the preproximal highly inclined orbits whose data were employed in these studies (typically in the range ~3 to ~10 R_S), the traversals of the auroral and subauroral field regions on each pass were more variably located and considerably slower, lasting generally of order the PPO cycle period. The consequently distinct analysis methodologies adopted in these studies then generated values of the maximum and minimum PPO azimuthal fields and meridional currents taken to occur at PPO phases $\Psi_{N,S}$ around ~90° and ~270°, assuming variation approximately as $+\sin\Psi_{N,S}$ in the equatorial region, and as $-\sin\Psi_{N,S}$ in the polar region (Figure 1). These values may then be compared with the fitted amplitudes derived here, and are overplotted in Figures 14b and 14d for the northern hemisphere, and in Figures 15b and 15d for the southern hemisphere. The red values are those derived by Hunt et al. (2014, 2015) from the preequinox 2008 interval of highly inclined orbits, the green values are those of Bradley, Cowley, Provan, et al. (2018) derived from post-equinox 2012–2013 data, while the black values are those of Hunt, Provan, Bunce, et al. (2018) derived from the F ring orbit periapsis pass data from 2016 to 2017 that immediately preceded the proximal orbit interval studied here. Data with equatorial phasing as $\sim+\sin\Psi_{N,S}$ are indicated by diamonds, while data with polar phasing as $\sim -\sin\Psi_{N,S}$ are shown by squares. We recall that the phases determined here, shown in Figures 10b and 11b, deviate toward polar values from the phases observed in the outer subauroral region only in the smallest colatitude region traversed in the northern hemisphere inside of ~17° northern colatitude, and is not observed at all in the region traversed in the southern hemisphere (see Figures 10b and 11b and further in section 5.2).

For the northern hemisphere data in Figures 14b and 14d there is good overall correspondence between the proximal orbit amplitude profiles and those determined from the 2008 (red) and 2012–2013 (green) data,

both with regard to magnitude and form. The peak values in the northern auroral region for the 2008 data determined by Hunt et al. (2015) are somewhat larger than those determined here, by a factor of ~2 for the then-dominant southern PPO system, while those for the 2012–2013 data with similar PPO conditions to those occurring during the proximal orbits (i.e., near-equal amplitudes to mildly northern-dominant) determined by Bradley, Cowley, Provan, et al. (2018) are very comparable for both systems. The current peaks in the previously derived profiles occur at slightly larger co-latitudes by ~1°–2°, which is likely a LT effect, since the northern passes in 2008 and 2012–2013 occurred on the nightside, centered near ~21 and ~03–06 hr, respectively, while those on the inbound proximal orbits occurred in the dawn and postdawn sector (Figure 3). The same effect likely also accounts for the smaller colatitude of the current peak derived by Hunt, Provan, Bunce, et al. (2018) from the F ring data (black), which were observed on the dayside in the prenoon sector. However, it is unclear why the peak amplitude of ~0.4 MA/rad for the northern system in Figure 14b is less than half of those determined here and in the other prior studies, and is consistent with zero within errors for the southern system in Figure 14d. Comparing these profiles, however, it is evident that in the northern hemisphere the most poleward proximal orbit data in the auroral region just straddles the peak in the PPO-related fields and currents. Equatorward thereof, these data newly show that the PPO fields and currents extend continuously onto ring field lines, with some augmentation in the D ring region.

For the southern hemisphere data in Figure 15 we first note that no northern system oscillations were discerned in the southern 2008 data by Hunt et al. (2014), such that no corresponding (red) profile appears in Figure 15b. The profile determined from the 2012–2013 data (green) by Bradley, Cowley, Provan, et al. (2018), however, corresponds quite well with the proximal values determined here over their rather restricted common range, with values that peak at ~0.7 MA/rad at ~18°–19° southern colatitude just poleward of the range covered by the proximal data. These values are a little lower than those of the northern system in the northern hemisphere for the related 2012–2013 data in Figure 14b. The values obtained from the 2016–2017 F ring orbits (black) by Hunt, Provan, Bunce, et al., 2018are again significantly smaller, peaking at ~0.25 MA/rad at smaller southern colatitudes of ~15.5°. For the southern system in the southern hemisphere in Figure 15d we see that the peak values determined from the 2008 and 2012–2013 data are both ~1.0 MA/rad at ~20°, larger than the peak values determined from the proximal data by a factor of ~2, while the 2016–2017 F ring orbit peak values are again smaller at ~0.3 MA/rad located slightly poleward at ~18°. We note that both F ring and proximal data were obtained at similar predusk to dusk LTs and are thus directly comparable, while both 2008 and 2012–2013 data were obtained in the midnight sector, likely giving rise to the relative equatorward displacement of the peak currents. Overall, however, this comparison shows that in the southern hemisphere the most poleward proximal data corresponds to the region lying just equatorward of the peak in the PPO-related fields and currents in the auroral region, extending into the subauroral and ring regions of weaker PPO fields and currents.

5.2. Mapping Azimuthal Component PPO Amplitudes to the Equator

In addition to mapping the azimuthal field amplitudes to the ionosphere, these values can also be mapped along field lines into the equatorial plane using

$$B_{\varphi 0\ eq} \approx \left(\frac{\rho}{\rho_{eq}}\right) B_{\varphi 0}, \tag{14}$$

where ρ_{eq} is the equatorial radial distance of the field line passing through the measurement point at perpendicular radial distance ρ. The mapping preserves the associated field-aligned current flow between flux shells, in the assumed absence of significant cross-field current flow between these points. In this case, of course, we obtain a pair of values at each equatorial radial distance, corresponding to the values mapped along the same field line from the northern inbound and southern outbound passes. In general, for a given PPO system we expect the value mapped from the data in the "generating" hemisphere, the northern hemisphere for the northern system and the southern hemisphere for the southern system, to be larger than the value mapped from the opposite hemisphere, the former value representing an upper limit to the equatorial value and the latter a lower limit, their difference being related to the cross-field currents flowing on the field lines between the two measurement points (see Figure 1).

In Figures 16a and 16c we show the equatorial azimuthal field amplitude profiles $B_{\varphi 0\ eq}$ for the northern and southern PPO systems, respectively, plotted versus equatorial radial distance, where a log-log format is now

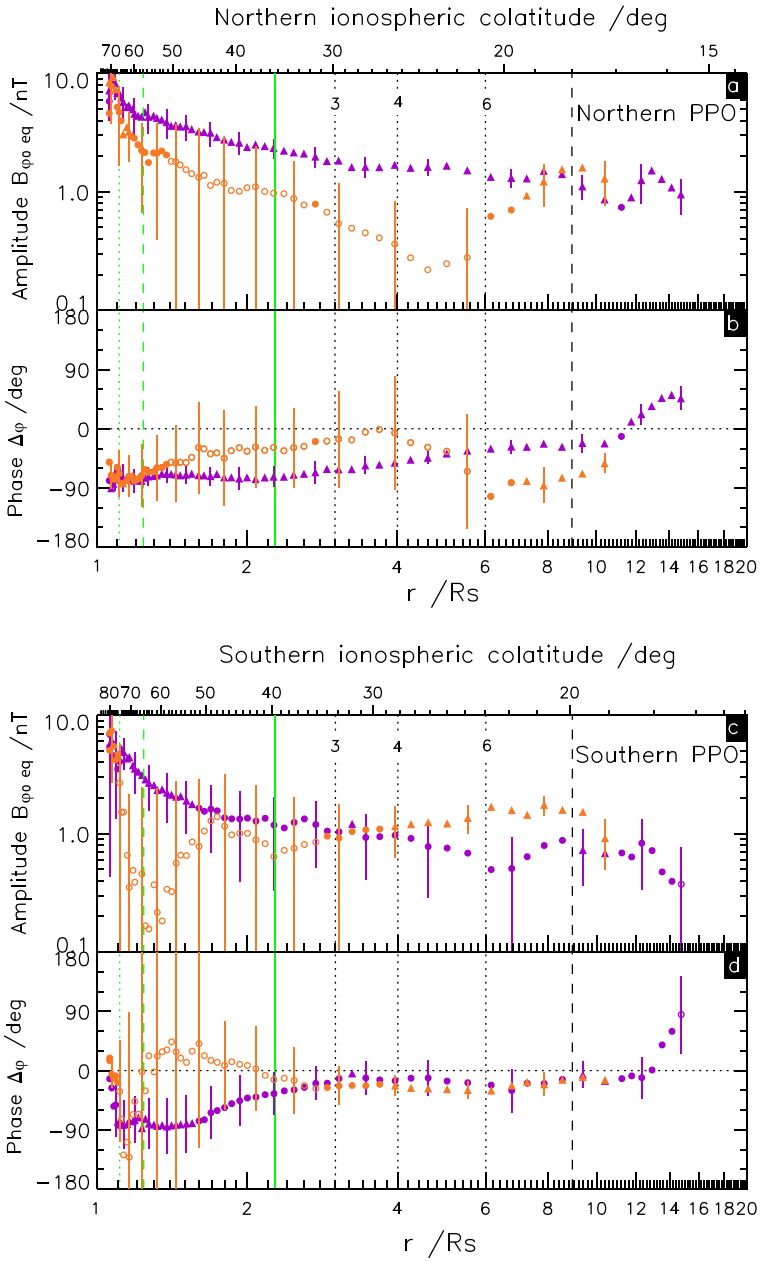

Figure 16. Plots of the amplitude and phase of the azimuthal field component PPO oscillations shown in Figures 10 and 11 mapped to the equator using the model field, and shown versus the equatorial radial distance (R_S) on a log-log scale. The northern PPO amplitudes and phases are shown in Figures 16a and 16b, respectively, while the southern PPO amplitudes and phases are shown in Figures 16c and 16d, respectively. The amplitudes from Figures 10a and 11a have been mapped to the equator using equation (14), while the phases have been transcribed directly. In both cases, the profiles mapped from the northern hemisphere data are shown by the purple symbols, while the profiles mapped from the southern hemisphere data are shown by the orange symbols. As in Figures 10 and 11, solid symbols represent values for which the amplitude exceeds the estimated uncertainty, while for the open circles this condition is not satisfied. The vertical lines delineate the boundaries of physical regions, with increasing radial distance marking the inner and outer boundaries of the D ring (green dotted and dashed lines), the outer boundary of the A ring (solid green line), and the inner boundary of auroral region field lines (black dashed line).

employed in order to satisfactorily accommodate the data. Scales of equivalent mapped northern or southern ionospheric colatitude are shown at the top of each pair of plots. The set of vertical lines in the figure have the same meaning as those in Figures 10–12, delineating ring region, subauroral, and auroral regimes. The amplitude values obtained from mapping the northern profiles in Figures 10a and 11a are shown by the purple symbols, while those obtained by mapping the southern profiles are shown by the orange symbols. Solid symbols again indicate well determined values for which the amplitude is larger than the estimated

uncertainties in the same format as Figures 10 and 11, while the open circles indicate values for which this condition is not satisfied, thus being consistent with zero. Figures 16b and 16d show profiles of the northern and southern phase deviation Δ_φ in a similar format, transcribed without modification from Figures 10b and 11b.

With only a few exceptions it can first be seen that for the well determined values, those mapped from the northern hemisphere are larger than those mapped from the southern hemisphere for the northern PPO system in Figure 16a (purple data larger than orange), and vice versa for the southern PPO system in Figure 16c (orange data larger than purple), as expected (see also section 4.2.4 and Figures 13a and 13d). With regard to the exceptions, it may be recalled that the northern and southern data were obtained in differing LT sectors and are thus not actually on the same field lines as each other, the northern data being obtained largely in the prenoon sector and the southern data largely in the postnoon sector (Figures 3, 13b, and 13e). Examining the individual profiles, we see in Figure 16a that for the northern PPO system, the mapped amplitudes initially fall rapidly across D ring field lines (bounded by the green dotted and dashed lines) from peak 5–10-nT values, essentially unmodified compared with Figure 10a, to much more slowly falling values ~3 nT in the main ring region (bounded by the green solid line), at least as determined from the mapped northern hemisphere data. In the subauroral region the values mapped from the northern hemisphere continue to fall slowly to ~1.5 nT in the outer part of the subauroral region, becoming more variable but with similar magnitude in the inner part of the auroral region (beyond the black dashed line). The well determined values derived from the southern hemisphere data in the outer subauroral and auroral regions then increase from ~0.6 nT to values close to, or even slightly exceeding, those derived from the northern hemisphere data.

The southern PPO system amplitude profiles in Figure 16c show similar behavior for the well determined values, initially falling rapidly from several-nT values on intra-D ring and D ring field lines to more slowly varying values in the outer regions. Values derived from southern hemisphere data (orange) show slowly rising values ~1–2 nT in the subauroral region, while those derived from northern hemisphere data (purple) fall slowly from ~1 nT in the inner subauroral region to ~0.7 nT in the outer subauroral and inner auroral regions. Overall, these data are consistent with a slow and steady fall in amplitude with radial distance in the equatorial region, from ~2–3 nT in the inner main ring region to ~1–2 nT in the subauroral and inner auroral regions. This sense of variation is evidently opposite to that of the directly determined azimuthal component amplitudes in Figures 10a and 11a from which they were derived, which instead generally increase with decreasing mapped ionospheric colatitude (increasing equatorial radial distance) to peak sharply at ~10–15 nT values on outer subauroral and inner auroral field lines. This behavior is thus seen to be an effect of the convergence of the field lines and associated field-aligned currents (Figure 1) between the equator and the high-latitude measurement points, with near-constant ~1–2 nT equatorial values increasing as ~$1/\rho$ along the field lines toward the planet.

In Figure 17 we compare these results with those obtained directly from equatorial data by Andrews, Cowley, et al., 2010, their Figure 4a), who derived three-component radial profiles of PPO amplitudes and phases in 4-hr LT sectors in the subauroral and auroral regions outside of ~3 R_S. The data concerned were acquired during extended equatorial orbit intervals during 2004–2007, such that the relevant PPO system was the then-dominant southern system. Following the color-coding adopted by Andrews, Cowley, et al. (2010), the azimuthal component radial profiles obtained in the postdawn (6–10 hr LT), noon (10–14 hr), and predusk (14–18 hr) sectors are shown by green, yellow, and red diamonds, respectively, joined by similarly color-coded dashed lines. These radial profiles, obtained using nonoverlapping 3 R_S bins, are shown superposed on the mapped northern and southern PPO azimuthal amplitude profiles derived here in Figures 17a and 17b, in the same format as Figures 16a and 16c, though with a stretched vertical scale for clarity. Overall, it is seen that the values are similar in magnitude and form to those derived here from the mapped proximal data, particularly with the northern data for the northern system and the southern data for the southern system. Values generally fall from ~1–2 nT in the innermost 3–6 R_S radial range to ~0.5–0.75 nT in the outermost 12–15 and 15–18 R_S ranges relevant to the present results. It is interesting to note, however, that the profiles derived from nightside sector equatorial data by Andrews, Cowley, et al. (2010) show rather different behavior, as shown in the same format in Figures 17c and 17d. Here the profiles obtained from data in the post-dusk (18–22 hr LT), midnight (22–02 hr), and predawn (02–06 hr) sectors are shown by the mauve, black, and blue diamonds, respectively. These amplitudes rise from similar ~0.5–1.5-nT values in the innermost

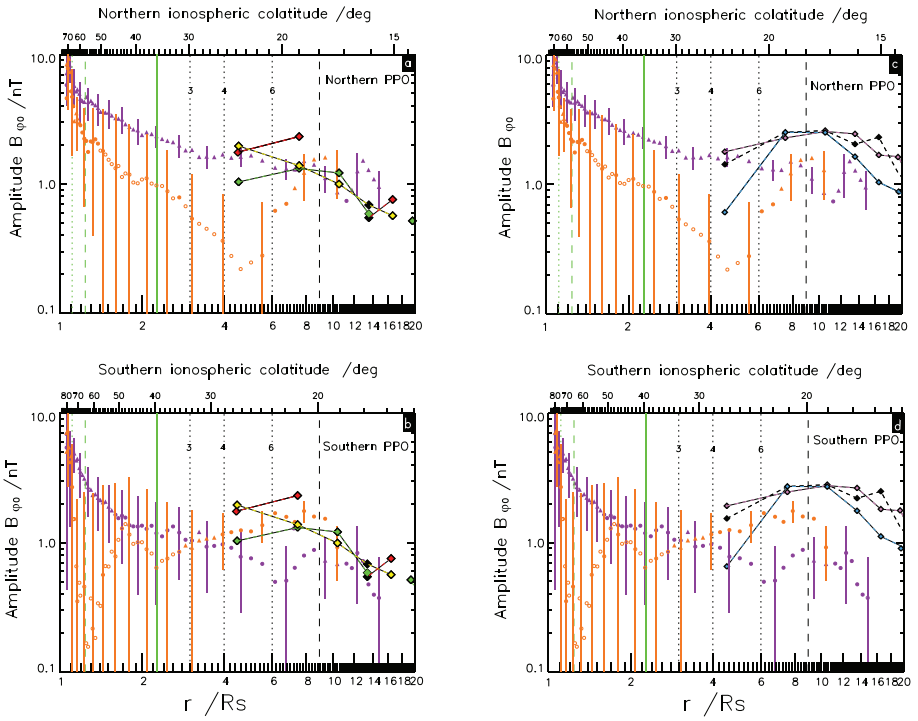

Figure 17. Comparison of the mapped equatorial azimuthal component PPO amplitude profiles derived here from the proximal periapsis passes and those derived directly from equatorial data by Andrews, Cowley, et al. (2010). The proximal profiles for the northern PPO system are shown in Figures 17a and 17c and for the southern PPO system in Figures 17b and 17d, in the same format as Figure 16 except for a stretch in scale of the vertical axis to improve clarity. The azimuthal field profiles derived by Andrews, Cowley, et al., 2010, their Figure 4a) from equatorial data acquired during 2004–2007 correspond to those of the then-dominant southern PPO system, and are shown by diamond symbols joined by dashed lines. Andrews, Cowley, et al. (2010) employed nonoverlapping 3 R_S radial intervals, the innermost spanning 3–6 R_S (thus centered at 4.5 R_S as shown), and 4-hr nonoverlapping intervals of LT. The profiles shown in Figures 17a and 17b correspond to the dayside sector most relevant to the proximal data analyzed here, specifically the postdawn sector 6–10 hr LT (green), the noon sector 10–14 hr (yellow), and the predusk sector 14–18 hr (red). At larger distances coverage of the predusk sector is poor in this data set. In Figures 17c and 17d we instead superpose the azimuthal amplitude profiles from nightside data, corresponding to the postdusk sector 18–22 hr LT (mauve), the midnight sector 22–02 hr (black), and the predawn sector 02–06 hr (blue).

radial range, in approximate accord with the values derived here, to peak at ~2.5 nT broadly across the radial range ~7.5–15 R_S, typically well above the dayside amplitudes derived here. Andrews et al. (2019) have suggested that this difference arises due to a factoring into the equatorial nightside data of fields associated with the PPO-related tilting of the equatorial current sheet, thus not related directly to the magnetosphere-ionosphere coupling currents whose effects dominate at high latitudes.

We may also compare the results in Figures 16a and 16c with the near-equatorial core region amplitudes derived in a sequence of studies by Andrews et al. (2012, their Table 1), Provan et al. (2013, their Table 1), and Provan et al. (2016, their Figure 6), spanning postsolstice southern summer (2005–2007), near equinox and postequinox (2009–2012), and northern spring data (2015), respectively. These three-component amplitudes were derived from individual fits to near-equatorial periapsis pass data spanning from periapsis typically at ~4 R_S (usually between ~3 and ~5 R_S) to an outer limit of 12 R_S chosen to correspond to the quasi-dipolar core region of the magnetosphere, thus corresponding to the middle and outer subauroral and innermost auroral regions in the present study (see also Figure 1a where the dashed line where the azimuthal component reverses sign typically corresponds to ~15 R_S). Such data also generally covers a broad and variable range of LTs. Reviewing the azimuthal field amplitudes quoted in these studies for the dominant system, the southern system during southern summer, the northern system for postequinox and northern spring, and either for the near-equal amplitude conditions during the equinoctial interval, we find values typically in the range ~1.4 to ~1.7 nT. Such values are again entirely comparable with those derived in the

outer subauroral and inner auroral regions from the northern hemisphere data for the northern system in Figure 16a and the southern hemisphere data for the southern system in Figure 16c, though usually being a little larger than the well determined values derived from the opposite hemispheres.

We may further compare the values of the radial and colatitudinal component amplitudes between the equatorial region and the higher latitudes examined here. The equatorial core region radial component amplitudes reported in the above-cited papers are typically somewhat less than the azimuthal amplitudes by factors of ~0.5–0.6, thus having typical values ~0.8–1.0 nT for the dominant system, while colatitudinal component amplitudes are typically comparable with or slightly less than the azimuthal amplitudes with factors of ~0.9–1.0, thus having typical values ~1.3–1.7 nT. We note that these values are in good accord with the values derived by Andrews, Cowley, et al., 2010, their Figure 4a) in the corresponding subauroral and inner auroral radial ranges. As for the azimuthal field component, the absolute values of the amplitudes of the radial and colatitudinal components in the subauroral and inner auroral regions in Figures 10a and 11a are again larger than the corresponding equatorial values, but only by factors of 2–3, that is, by not so large a factor as the ~$(1/\rho)$ field convergence factor of up to an order of magnitude for the azimuthal field component. As a consequence, on subauroral field lines the amplitude ratio of the radial component relative to the azimuthal component falls from ~0.5 to 0.6 in the equatorial region, as found in the core region analyses, to ~0.15–0.3 at high latitudes on the proximal orbits as discussed in the section 4.2.3 (Figure 12). For the colatitudinal component in the same region the ratio similarly falls from ~0.9–1.0 in the equatorial region to ~0.4–0.6 on the proximal orbits. Thus while the amplitudes of the radial and colatitudinal components do increase away from the equator, the increase in each case is roughly half of the ~$(1/\rho)$ increase in the azimuthal component.

We now examine the azimuthal component phase deviations Δ_φ of the northern and southern PPO systems relative to the phases derived by Provan et al. (2018), shown in Figures 16b and 16d, respectively, which provides a radial perspective on these values additional to that discussed relative to Figures 10b and 11b in section 4.2. In both cases Δ_φ is shifted to earlier phases near ~−90° within the D ring region, and rises to smaller but still negative values at larger radial distances across the main ring region, as determined from the northern hemisphere data. The rise in phase deviation is rapid to ~−30° for the southern system, but is more gradual to ~−75° for the northern system. There is also evidence of a sharp increase toward zero and positive values within the innermost intra-D ring region. In the subauroral region the southern system phase deviation is near-constant at ~−15° as determined from both data sets, while for the northern system the phase deviation continues to increase gradually to ~−30° in values determined from the northern hemisphere data. It is also seen that for both systems the phase deviations move consistently toward positive "later" phases ~+45° at the largest radial distances observed, traversed only inbound on northern (and dawn sector) field lines, at mapped radial distances between ~12 and ~15 R_S. This behavior mirrors that derived by Andrews, Cowley, et al. (2010) for the azimuthal component at similar equatorial radial distances (their Figure 4a), related to the reversal in sense of the azimuthal PPO component in the outer equatorial and polar magnetosphere (across the dashed line circle in Figure 1a).

The negative phase shifts of typically a few tens of degrees observed in the subauroral regions, larger for the northern system than for the southern, may possibly be due to the regions from which these phases were derived by Provan et al. (2018). For the northern PPO system the phases were derived using the nightside northern polar data available from the inbound passes of the highly inclined F ring and proximal Revs (see Figure 3 of Provan et al. (2018)), it being previously found by Hunt et al. (2015, 2016) that the oscillations on such field lines, having taken account of the phase deviations of the individual field components, may be subject to a delay relative to the subauroral region by a few tens of degrees. In particular, Hunt et al. (2016) using high-latitude data from 2008 found that the polar oscillations in both the northern and southern hemispheres were delayed by ~35° relative to the subauroral region. Such a delay in the F ring and proximal orbit northern polar oscillations employed by Provan et al. (2018) would then result in the oscillations in the subauroral region in the present case appearing to have earlier phases by a comparable value, as observed. The southern system phases derived by Provan et al. (2018) were obtained from southern hemisphere off-equatorial data at ~10–15 R_S radial distances (see their Figure 3), for which phase shifts of this order relative to the inner subauroral region may also be plausible. On the other hand, we note that no such phase shifts between polar and subauroral region data were detected by Bradley, Cowley, Provan, et al. (2018) using high

latitude data from 2012 to 2013. In either case such phase shifts would not account for the earlier ~−90° phases observed in the inner ring region for both systems.

6. Mean Residual Fields

Although the focus of the paper thus far has been on the properties of PPO field oscillations in the inner region of Saturn's magnetosphere, a further product of the analysis is profiles of the mean residual fields $\overline{\Delta B_j}$ in equation (6), from which PPO effects are in principle removed. Previous related results related specifically to the azimuthal field component are overviewed in section 1.3. Of course this study actually provides two mean field profiles for each component, one from the northern PPO fit analysis, the other from the equivalent southern PPO fit analysis. However, examination shows that these two estimates are very closely similar as may be expected, typically to within a few percent (compare, e.g., Figures 6 and 7 and Figures 8 and 9). They are also closely similar to the simple arithmetic mean of the data contributing to each colatitude bin, as also expected for data sets with well-spread ensembles of contributory PPO phases. Here we have arbitrarily chosen to display the mean field obtained from the northern PPO fit analysis.

6.1. Mean Field Results

Results are shown in Figure 18, plotted versus mapped northern ionospheric colatitude in a format similar to Figures 10 and 11 (with southern mapped ionospheric colatitude being shown at the top of the plot). For the radial and colatitudinal field data in Figures 18a and 18b, respectively, we recall that the values represent the residual fields after subtraction from the measured data of the full spherical harmonic degree 11 internal field of Dougherty et al. (2018), together with a fixed axisymmetric model ring current field. A small data discontinuity can be seen across the center of the plot (vertical black dotted line), resulting from the fact that (as in previous sections) these values were derived from data organized by background magnetic field line. Although this choice was made for the PPO analysis in order to clearly organize the data by physical regime, as in previous related analyses, this leads to the exclusion of data from some more deeply penetrating passes that map to marginally larger colatitudes than the upper limit of 72° employed here (up to ~76° in the northern ionosphere), this limit being set by the requirement of having sufficient data in each bin to obtain good coverage of PPO phase. Although this manner of combining the data might not be optimum for examining the mean values of the poloidal components in the immediate equatorial region, the results are sufficient to show the general nature of the mean residual fields, which vary quasi-sinusoidally with latitude with ~5-nT peak-to-peak amplitude in approximate quadrature between the radial and colatitudinal components (see also Dougherty et al. (2018)). The same behavior is also evident in the continuous time-series plots in Figures 4 and 5. It remains unclear whether these field variations are generated internally by the planet, or whether they are due, for example, to currents flowing in the ionosphere below the spacecraft. In the latter case, the quadrature perturbations suggest the presence of a sequence of east-west directed currents that in the equatorial region are approximately antisymmetric about the field-parallel point.

For the azimuthal component in Figure 18c, however, organization of the data by magnetic field line (i.e., physical regime) is again a more natural choice. We recall from section 1.3 that in previous studies principally of the auroral regions, the mean azimuthal field generally corresponds to a lagging configuration, taken to relate to plasma subcorotation and outward transport of planetary angular momentum. As also indicated in section 1.3, the mean azimuthal field at ionospheric heights generally peaks just equatorward of the OCB, and falls across the auroral region to smaller variable values on subauroral field lines. The fall in azimuthal field magnitude is associated with upward-directed field-aligned currents in both hemispheres, and thus with Saturn's auroras. While in the nightside data studied by Hunt et al. (2014, 2015) and Bradley, Cowley, Provan, et al. (2018) the weak subauroral fields beyond ~18° northern ionospheric colatitude (~20° southern ionospheric colatitude) were found to be variable in nature but with indications of a weak leading field configuration, in the dayside F ring periapsis pass data studied by Hunt, Provan, Bunce, et al. (2018), Hunt, Provan, Cowley, et al. (2018) weak lagging fields were observed throughout the subauroral region to periapsis just outside of the ring region. In Figure 18c it can be seen that in the subauroral regions the mean azimuthal fields for the proximal data largely follow the results obtained on the F ring orbits, with lagging negative fields in the northern hemisphere and positive fields in the southern hemisphere which extend from the subauroral region inner boundary interfacing with the ring field region (green solid lines), to near the auroral region. An exception occurs in the spike of positive leading mean azimuthal fields which occurs

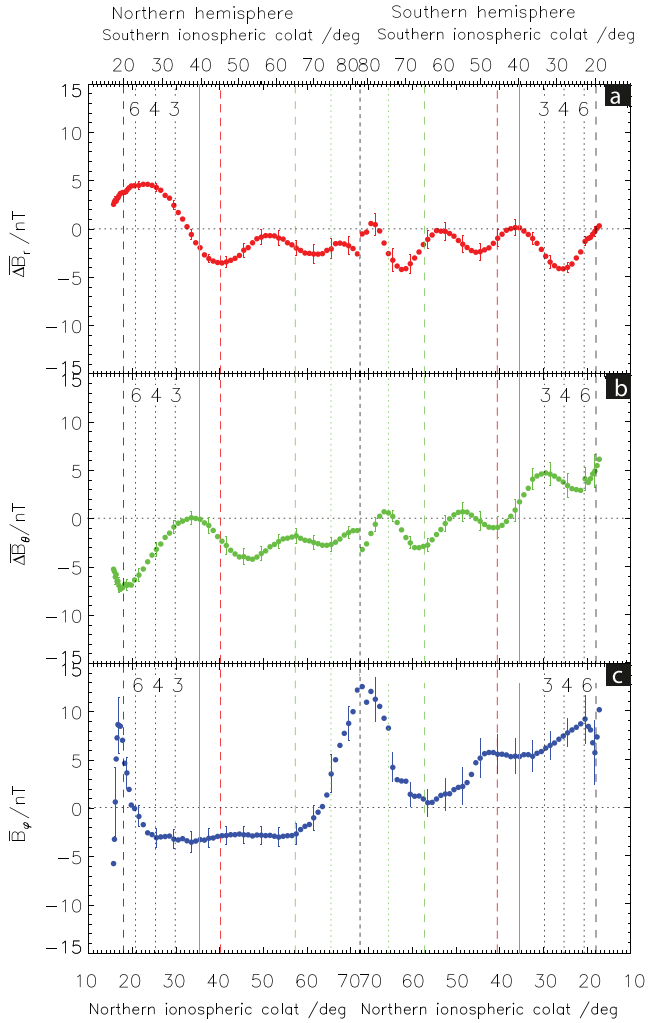

Figure 18. Overview of mean field residual values $\overline{\Delta B_i}$ obtained from the fit analysis to the periapsis pass data organized by northern PPO phase. (a) The mean residual field for the radial component. (b) The mean residual field for the colatitudinal component. (c) The mean value of the azimuthal field component. The values from the southern PPO phase fits are very closely similar, and also to the direct arithmetic means. As in Figures 10 and 11, the northern inbound and southern outbound data are shown on the left and right of the plot, respectively, both plotted versus mapped northern ionospheric colatitude, with an equivalent scale of southern ionospheric colatitude being shown at the top of the plot. The vertical lines are also as for Figures 10 and 11 (and Figures 4 and 5), with the exception that the red dashed lines correspond to field lines passing through Saturn synchronous orbit in the equatorial plane (~1.86 R_S) for a nominal rotation period of 10.6 hr.

across the boundary between the auroral and subauroral regions in the northern hemisphere, which, as shown in section 6.2 below, has no counterpart in any of the previous related studies. It is evident in the time series plots in Figures 4 and 5, however, that the azimuthal data are highly variable in this region as reflected in the large uncertainty values in Figure 18. This feature might thus be regarded as a peculiarity of the proximal data set, with only 23 individual contributions, possibly associated with unusual outer magnetospheric conditions in the dawn sector on some of these passes.

Inside the subauroral region, however, the data in Figure 18c newly show that the mean azimuthal fields are continuous across the boundary between the subauroral and outer ring regions, thus maintaining their lagging configuration on ring field lines. This degree of continuity seems remarkable if the fields are associated with plasma subcorotation, given that plasma production and radial transport must be considerably different in the subauroral and ring regimes. Indeed, throughout much of the ring region where the lagging fields are observed, the angular velocity of the Kepler-orbiting ring grain material and associated neutral gas

considerably exceed that of the planet. The vertical red dashed lines in Figure 18 indicate field lines that pass through the equator at the synchronously-orbiting point for a nominal rotation period of 10.6 hr, the corresponding equatorial radius being ~1.86 R_S in the outer part of the B ring. At the outer boundary of the D ring (green dashed lines), for example, the Kepler orbit period is reduced to ~5.8 hr. Particle pick-up alone in this region would instead result in a leading field configuration, opposite to that observed. The results in Figure 18c clearly show, however, that in the northern hemisphere the ~3-nT negative azimuthal field shows no marked feature at this or any other boundary between the central subauroral region and the outer boundary of D ring field lines. In the southern hemisphere the corresponding positive field is also near-constant but somewhat larger at ~6 nT between the central subauroral region and across the outer A ring and synchronous orbit field lines. There is therefore no evidence in these results for the ionosphere-ring interaction current system hypothesized by Xin et al. (2006) on the basis of a similar discussion to that given above, in which the azimuthal field perturbation reverses sense about Saturn synchronous orbit from lagging outside this orbit to leading inside. In the southern hemisphere, however, the lagging azimuthal field drops rapidly across the inner ring region interior to synchronous orbit, to near zero at the outer D ring boundary. This inner region of reduced southern hemisphere lagging azimuthal fields corresponds approximately to field lines on which the southern ionosphere at ~1,000-km heights is strongly shadowed from solar radiation by the densest parts of the B ring material, thus likely significantly reducing the mean ionospheric conductivity in this region (Hadid et al., 2018).

On and inside D ring field lines, however, the mean azimuthal fields are instead dominated by the near-symmetric field perturbations discussed previously by Dougherty et al. (2018) and Provan, Cowley, et al. (2019), attributed by Khurana et al. (2018) to the action of differential neutral atmospheric wind shear at the two ends of the near-equatorial field lines. These fields are confined within the outer boundary of D ring field lines, between the green dashed lines in Figure 18c, where they grow in magnitude across the D ring and intra-D ring regions on either side to peak at ~15 nT near the equator. The rise in magnitude appears particularly prominent near the inner boundary of the D ring region on both sides. This overall feature, however, is seen to be somewhat asymmetric about the equator by virtue of being superposed on the larger-scale oppositely-directed lagging fields on either side of the equatorial plane (as well, in general, of course, as being superposed on individual passes on the PPO-related fields of ~5–10-nT amplitude shown in Figures 10a and 11a).

6.2. Mapping Mean Azimuthal Values to the Ionosphere: Comparison With Previous Results

We now examine in more detail the relationship between the mean azimuthal fields in Figure 18c and the previous results outlined in section 1.3. As for the PPO azimuthal fields in section 5.1, to take approximate account of the differing radial distances at which the data were acquired, the measured values are mapped to the ionosphere using equation (12), and compared with the similarly mapped values derived from previous studies of high-latitude data by Hunt et al. (2014, 2015), Hunt, Provan, Bunce, et al. (2018) and Bradley, Cowley, Provan, et al. (2018). We again map the northern inbound data to the northern ionosphere and the southern outbound data to the southern ionosphere, with results shown by the blue circles in Figures 19a and 19c, respectively, plotted (as for Figures 14 and 15) on logarithmic scales of mapped ionospheric colatitude. These essentially follow the discussion of the measured fields in section 6.1, allowing for the modifying effect of the perpendicular distance factor, with near-symmetrical positive features peaking at ~10–15 nT inside the D ring region, but with oppositely-directed lagging fields (as indicated) outside, except for the prominent ~30-nT peak of leading values occurring across the inner auroral and outer subauroral region boundary in the northern hemisphere in Figure 19a.

The associated meridional ionospheric currents per radian of azimuth, I_m, together with those derived from earlier studies, are shown for the northern and southern hemispheres in Figures 19b and 19d, respectively. With the sign convention for I_m that it is positive when directed toward the equator in both hemispheres, as employed in the previous studies, the current is given by

$$I_m = \pm\frac{\rho_i B_{i\,\varphi}}{\mu_o} \approx \pm\frac{\rho B_\varphi}{\mu_o}, \tag{15}$$

where the upper and lower signs correspond to the northern and southern hemispheres, respectively. As for the PPO system in section 5.1, the results can then be employed to discuss related field-aligned current flow

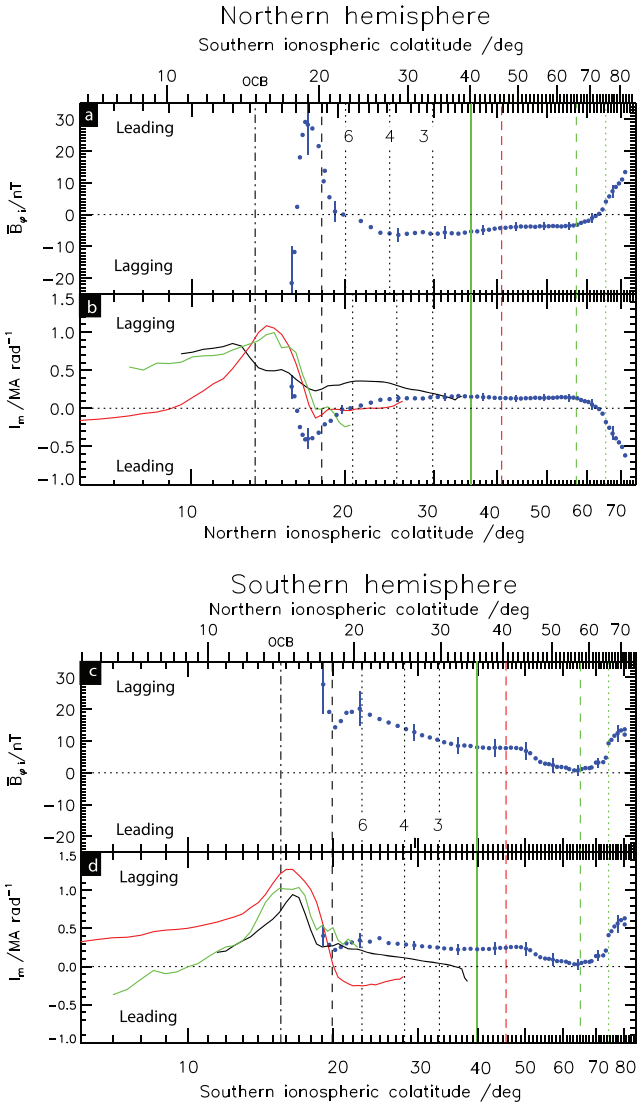

Figure 19. (a) A plot of the northern hemisphere mean azimuthal field from Figure 18 (blue circles) mapped into the northern ionosphere using equation (12), and plotted versus northern ionospheric colatitude on a log scale. An equivalent scale of southern ionospheric colatitude is shown at the top of the plot. (b) The corresponding meridional ionospheric current (blue circles), positive equatorward, derived from equation (15). The superposed lines show the related profiles derived from previous studies, by Hunt et al. (2014, 2015) from preequinox 2008 data (red), by Bradley, Cowley, Provan, et al. (2018) from postequinox 2012–2013 data (green), and by Hunt, Provan, Bunce, et al. (2018) from 2016–2017 F ring orbit data (black). (c) The southern hemisphere mean azimuthal field from Figure 18 (blue circles) mapped into the southern ionosphere using equation (12), and plotted versus southern ionospheric colatitude on a log scale. (d) The associated meridional ionospheric current (blue circles) derived from equation (15), together with the related profiles derived from previous studies using the same color code. The vertical lines are region identifiers as in Figures 14 and 15, with the addition of the red dashed line marking Saturn synchronous orbit for a nominal 10.6-hr period as in Figure 18.

into or out of the ionosphere directly from the colatitudinal variation of I_m. The current profiles derived from the proximal data are again shown by blue circles, while the values derived from previous studies are superposed using the same color codes as in Figures 14 and 15. That is, the red profiles are the values derived by Hunt et al. (2015) from the preequinox 2008 data set (their Figures 3b and 3d for the northern and southern hemispheres, respectively), the green profiles are those of Bradley, Cowley, Provan, et al. (2018) from the postequinox 2012–2013 data set (their Figures 7b and 7d), while the black profiles are those derived by Hunt, Provan, Bunce, et al. (2018) from the 2016–2017 F ring orbit data set (their Figures 4a and 4b). Vertical dashed lines show the same region identifiers as in Figures 14 and 15, with the addition of a red dashed line marking the field line passing through the equator at Saturn synchronous orbit as in Figure 18.

Examining the currents derived from the proximal data, we first note that the features on and inside D ring field lines on the right sides of Figures 19b and 19d indicate the presence of south to north ionospheric current flow in both hemispheres, closing via upward and downward directed field-aligned currents ~0.7 MA/rad in the north and south, respectively, as previously discussed by Dougherty et al. (2018), Khurana et al. (2018), and Provan, Cowley, et al. (2019). In the subauroral and main ring regions, however, the near-constant equatorward directed (lagging field) currents ~0.15 MA/rad in the northern hemisphere and ~0.25–0.3 MA/rad in the southern hemisphere indicate the overall presence of only very weak field-aligned currents in these regions. An exception occurs in the southern hemisphere in Figure 19d, where the decline in the meridional current in the inner part of the main ring region indicates the presence of an upward directed field-aligned current of ~0.25 MA/rad flowing from the southern ionosphere toward the ring plane, the ring region concerned spanning from the outer edge of the D ring at a radial distance of ~1.24 R_S to the inner part of the B ring at ~1.65 R_S. The other main feature is the large negative (poleward) current peak ~ −0.4 MA/rad occurring in the northern hemisphere near the inner boundary of the auroral region in Figure 19b, related to the positive (leading) peak in azimuthal field in Figure 19a, indicative of the presence of auroral region upward then principally subauroral downward field-aligned currents of at least ~0.5 MA/rad flowing in the vicinity of this boundary.

Comparison with the mean mapped ionospheric azimuthal fields determined from previous studies superposed in Figures 19b and 19d helps indicate the nature of the proximal data in relation to the overall profiles of the mean field and current. As discussed in section 1.3, the profiles derived from previous studies rise in a steady (but seasonally-dependent) manner in the polar region to peak generally just equatorward of the OCB, before falling rapidly to much smaller values across the auroral region. In the inner auroral and subauroral regions the mean fields and currents then exhibit weaker more slowly varying values which show indications of leading fields for the nightside 2008 data analyzed by Hunt et al. (2015) (red profiles), but of lagging fields for the dayside F ring orbit data presented by Hunt, Provan, Bunce, et al. (2018), Hunt, Provan, Cowley, et al. (2018) (black profiles). It is first clear from this comparison that in the northern hemisphere the proximal data correspond to the inner part of the auroral region of larger lagging fields and equatorward currents, and to the region of weaker slowly-varying fields equatorward thereof, though (as indicated in section 6.1) there is no counterpart in the earlier studies of the large peak in leading

fields and poleward currents in the vicinity of the auroral region boundary. In the southern hemisphere the proximal data correspond only to the latter weaker field region. Thus focusing on the subauroral data, the comparison secondly indicates that the lagging fields generally present on the dayside proximal passes relate to the similarly lagging fields observed in this region on the dayside F ring passes (black profiles), and are unlike the values obtained in this region on the nightside 2008 passes (red profiles). The proximal data then newly show that these lagging fields extend unmodified onto dayside ring region field lines, across Saturn synchronous orbit to the outer D ring field line boundary.

7. Summary

We have analyzed the periapsis pass magnetic field data from the final orbits of the Cassini spacecraft at Saturn (Revs 271–293) between April and September 2017, on which the spacecraft passed inbound from the northern auroral region in the dawn sector, through the equatorial plane in the noon sector in the gap between the D ring inner edge and Saturn's denser atmosphere, and outbound to the southern auroral region in the dusk sector. These orbits thus provided continuous in situ data that encompass auroral, subauroral, ring region, and intra-ring region field lines, the ring and intra-ring data being unique within the Cassini data set. Here we have employed the northern and southern system PPO phase models derived by Provan et al. (2018) using near-apoapsis nightside data from both F ring and proximal orbits to examine the periapsis pass data for the presence of PPO field oscillations, the analysis also generating profiles of the mean residual fields on these passes. Principal results are as follows.

a Dual modulation of the field by northern and southern PPO systems was found almost continuously in these data, demonstrating for the first time the presence of PPOs on and inside ring region field lines. While oscillations in all three field components were detected for both systems in the northern inbound ring region data, only colatitudinal component oscillations for both systems were detected above the noise level in the southern outbound ring region. The presence of such field perturbations may provide explanation for apparent PPO-related phenomena observed in the ring material itself, through the action of these fields on charged dust grains. Where oscillations in all three field components are above the noise level, the azimuthal component is generally the largest in amplitude on the proximal passes, falling from ~10–15 nT on auroral field lines continuously across the subauroral region to ~3–5 nT on main ring field lines in the northern hemisphere, then increasing somewhat to ~7–9 nT across D ring field lines into the intra-D ring region. The amplitude of the colatitudinal field component is typically half that of the azimuthal component (except on southern ring region field lines), while the amplitude of the radial component is typically a quarter of that of the azimuthal component. The PPO oscillations form a significant contributor to the pass-to-pass variability of the field in these regions.

b The phases of both northern and southern system oscillations are typically ~10°–30° earlier than anticipated on the basis of the Provan et al. (2018) models in the inner auroral and outer subauroral regions, probably resulting from the phase models being derived using nightside data from outer magnetospheric and polar field regions. On ring region field lines, however, phases become progressively earlier, typically reaching ~90° phase deviation in the inner ring region. Oppositely, azimuthal component phases on central auroral region field lines traversed on northern inbound passes (but not reached on southern outbound passes) rotate significantly later toward polar values.

c Although the issue of the relative amplitudes of the two PPO systems is difficult to assess using largely off-equatorial observations, the proximal periapsis data are consistent with the view that the northern system was the stronger of the two during this interval, but not by a large factor, in agreement with previous estimates using F ring and nightside proximal orbit data by Hunt, Provan, Cowley, et al. (2018) and Provan et al. (2018), respectively. Overall, the present data set indicates a north/south system amplitude ratio ~1.25.

d Mapped to the ionosphere, the PPO azimuthal field amplitudes peak at ~30–60 nT in the inner part of the auroral region, implying peak meridional ionospheric currents of ~0.5–1 MA/rad, and fall to ~5–10 nT in the inner part of the subauroral region (within uncertainties of a few nT). These results are consistent with the prior analyses of nightside preequinox and postequinox auroral and subauroral region data by Hunt et al. (2014, 2015) and Bradley, Cowley, Provan, et al. (2018), respectively, in their regions of overlap, but are typically a factor of 2 larger than the values derived by Hunt, Provan, Bunce, et al. (2018) from dayside F ring orbit data.

e Mapped to the equator, azimuthal field amplitudes fall rapidly across D ring field lines, and then slowly with radial distance to the limit of these observations at mapped radial distances of ~15 R_S. Subauroral and inner auroral region values are consistent with those derived directly from dayside equatorial data by Andrews, Cowley, et al. (2010), while falling below those derived from nightside equatorial data. Peaking of the azimuthal component amplitudes in the auroral region in the proximal data is approximately consistent with an ~1/ρ increase along the field lines from near-constant values in the equatorial region as the field lines and associated currents converge toward the pole. Comparison also indicates that the colatitudinal and radial component amplitudes also increase away from the equator, but only by approximately half as much as the azimuthal component, giving rise to the ratios indicated under item (a).

f Mean values of the residual poloidal field components (with degree 11 internal field and fixed axisymmetric ring current field subtracted, and PPO modulations removed) show quasi-sinusoidal variations with latitude of ~5-nT peak-to-peak amplitude. The variations in the radial and colatitudinal components are to a first approximation in quadrature. It remains unclear whether these fields are generated internally within the planet or are due to ionospheric currents flowing below the spacecraft.

g Mean values of the azimuthal field, to which neither the planetary field nor the ring current contribute, are to a first approximation lagging in nature in the subauroral region with magnitude ~3–5 nT, consistent with the results of Hunt, Provan, Bunce, et al. (2018), Hunt, Provan, Cowley, et al. (2018) from analysis of the F ring orbit data. The proximal periapsis pass data show that these fields extend essentially unmodified into the ring region, and across field lines mapping to Saturn synchronous orbit. In the northern hemisphere they extend inward to the outer boundary of D ring field lines, while in the southern hemisphere they decline from a point somewhat inside of synchronous orbit to near-zero values at the same field line boundary, indicative of a field-aligned current flow of ~0.25 MA/rad flowing from the southern ionosphere toward the C and inner B rings. There are no indications in these results for the ionosphere-ring interaction current system suggested by Xin et al. (2006), proposed to reverse sense across Saturn synchronous orbit. Near-symmetrical azimuthal fields peaking at ~15 nT are superposed on and inside D ring field lines near the equator, as previously reported by Dougherty et al. (2018), Khurana et al. (2018), and Provan, Cowley, et al. (2019). The physical origin of the extended surrounding region of lagging dayside fields remains unclear.

Appendix A: Validity of Analysis Methodology

In this appendix we examine the validity of the analysis methodology adopted in section 4 in which the field modulations due to the northern and southern PPO systems were separately estimated from dual-modulated data by plotting the data separately versus the two PPO system phases, $\Psi_{N,S}$, and least-squares fitting a sinusoid plus constant term $B = \overline{B} + B_{0N,S}\cos\left(\Psi_{N,S} - \Delta_{N,S}\right)$ to the resulting data in each case (equation (6)). The fit parameters are the constant term $\overline{B}$ (essentially the mean field value for data near-uniformly spread in phase), the oscillation amplitudes $B_{0N,S}$, and the phase deviations relative to the system phases $\Delta_{N,S}$. This methodology relies on the assumption that the two system phases are essentially uncorrelated over the data set as a whole, such that modulations due to one system only produce amplitude-dependent scatter in the data organized relative to the other system, not leading to significant spurious cross-modulation amplitudes. We argued in sections 3 and 4 that this should be the case given that the interval considered corresponds to ~3.5 beat cycles of the two oscillations, though the numbers of data points in each fit, only 22 or 23 (one per contributing Rev), is relatively small. In this appendix we quantitatively examine the extent to which these assumptions are justified by generating simulated data sets of known input to which the methodology is applied.

As in sections 3 and 4 we take the PPOs to have fixed rotation periods over the whole interval, given by $\tau_N = 10.792$ h $_r$ and $\tau_S = 10.679$ h $_r$ for the northern (N) and southern (S) systems, respectively, such that we may write the system phases as

$$\Psi_{N,S}(\varphi, t) = \frac{360t}{\tau_{N,S}} - \varphi - \psi'_{N,S}, \tag{A1}$$

for some pair of phase constants $\psi'_{N,S}$. To enhance the veracity of the simulated data we employ actual times and azimuths of corresponding points on the 22 full proximal Revs, which for convenience we have taken to

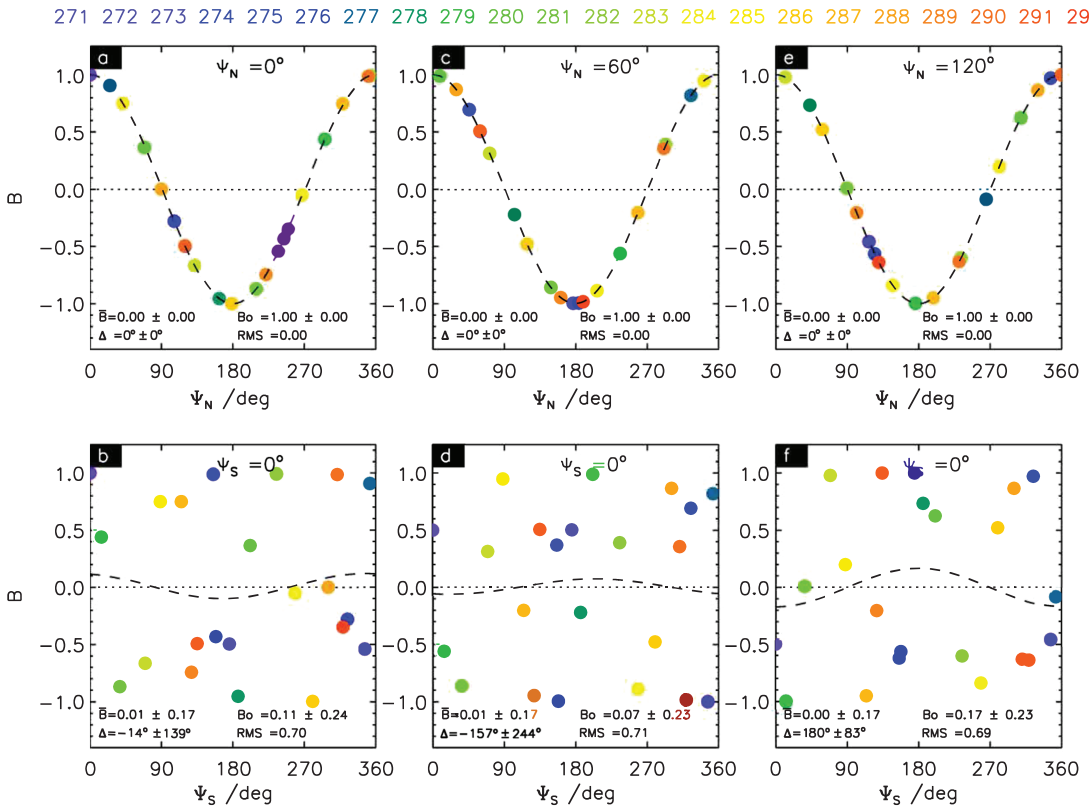

Figure A1. Plots of simulated color-coded PPO-modulated field data derived from equation (A3) as described in Appendix A, for $B_N = 1$ and $B_S = 0$, are shown plotted (top row) versus the northern PPO phase in Figures A1a, A1c, and A1e and (bottom row) versus the southern phase in Figures A1b, A1d, and A1f, where the phases are as given by equation (A2). The northern phase constant is taken as (left column) $\psi_N = 0°$ in Figures A1a and A1b, (middle column) $\psi_N = 60°$ in Figures A1c and A1d, and (right column) $\psi_N = 120°$ in Figures A1e and A1f, while the southern phase constant is taken as $\psi_S = 0°$ throughout. The dashed lines show the least squares best fit sinusoids given by equation (A4a) for the top row of panels, and by equation (A4b) for the bottom row of panels, with fit constants and estimated uncertainties indicated in each panel.

be the field-parallel points on each pass (as employed to organize the data in Figures 4 and 5). These times and azimuths are denoted as t_n and φ_n, where index $n = 1,\ 2,\ \ldots\ldots\ 22$, with $n = 1$ corresponding to the first proximal Rev 271, and $n = 22$ to the last full proximal Rev 292. By suitable choice of the phase constants $\psi'_{N,S}$ we can then write the PPO phases as

$$\Psi_{N,S}(\varphi, t) = \frac{360(t-t_1)}{\tau_{N,S}} - (\varphi - \varphi_1) - \psi_{N,S}, \tag{A2}$$

a form that allows the relative phasing of the two modulations to be simply choosable through the difference in the phase constants ψ_N and ψ_S. The dual-modulated data is then simulated by the set of 22 values

$$B_n = B_N \cos\left(\frac{360(t_n-t_1)}{\tau_N} - (\varphi_n - \varphi_1) - \psi_N\right) + B_S \cos\left(\frac{360(t_n-t_1)}{\tau_S} - (\varphi_n - \varphi_1) - \psi_S\right), \tag{A3}$$

where amplitudes B_N and B_S, and phases ψ_N and ψ_S are choosable model constants. As in section 4, we then least squares fit these dual-modulated model data separately with the functions

$$B_N = \bar{B}_N + B_{N0} \cos\left(\frac{360(t-t_1)}{\tau_N} - (\varphi - \varphi_1) - \psi_N - \Delta_N\right) \tag{A4a}$$

and

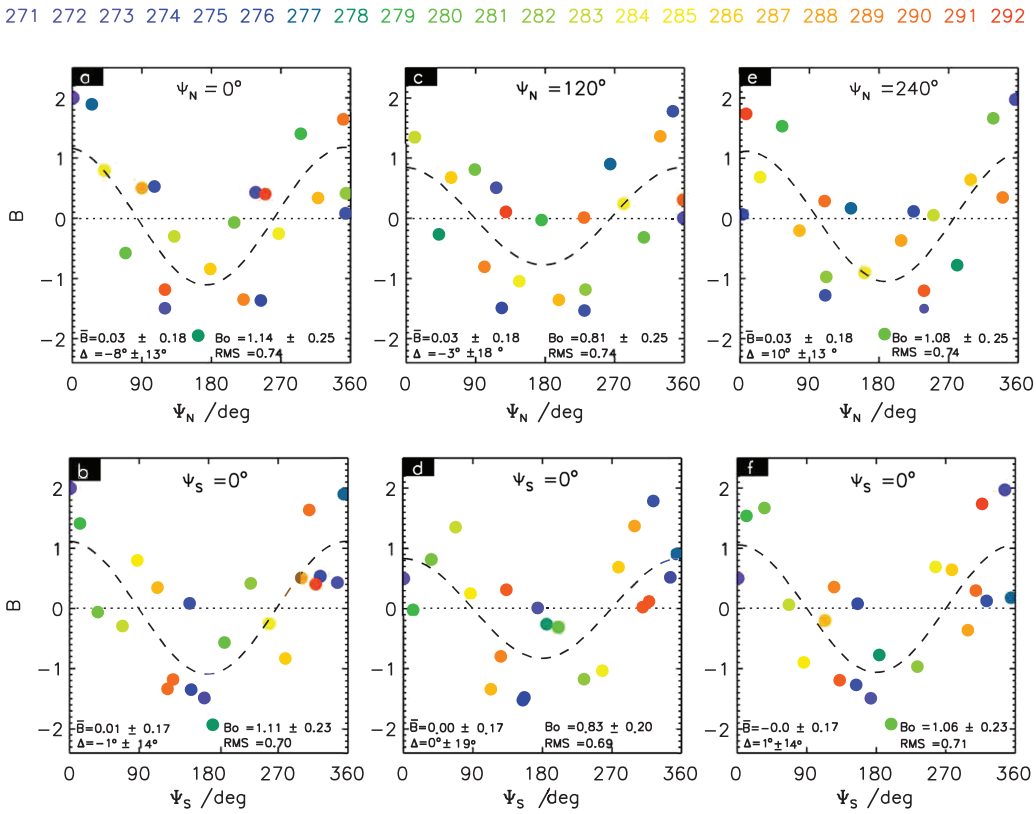

Figure A2. Same for Figure A1 except for dual-modulated data of equal amplitude, that is, $B_N = B_S = 1$ in equation (A3). The northern phase constant is taken as (left column) $\psi_N = 0°$ in Figures A2a and A2b, (middle column) $\psi_N = 120°$ in Figures A2c and A2d, and (right column) $\psi_N = 240°$ in Figures A1e and A1f, while the southern phase constant is taken as $\psi_S = 0°$ throughout.

$$B_S = \overline{B}_S + B_{S0}\cos\left(\frac{360(t-t_1)}{\tau_S} - (\varphi-\varphi_1) - \psi_S - \Delta_S\right), \tag{A4b}$$

and we examine how close the separately fitted amplitudes $B_{N,S0}$ are to the chosen values $B_{N,S}$, and how close the phase deviations $\Delta_{N,S}$ are to zero.

We now present some representative sample results. We first examine the extent of the cross-modulation that occurs when one oscillation is present but not the other, by taking $B_N = 1$ and $B_S = 0$ in equation (A3). We consider various values of phase constant ψ_N, and while ψ_S is irrelevant in equation (A3) when $B_S = 0$, we take $\psi_S = 0$ when fitting equation (A4b) to the data to determine the (in this case spurious) southern PPO modulation parameters. Figure A1 shows results for three values of ψ_N, for $\psi_N = 0°$ in Figures A1a and A1b, $\psi_N = 60°$ in Figures A1c and A1d, and $\psi_N = 120°$ in Figures A1e and A1f, where the first of these figures in each case (top row of panels) shows the color-coded data least squares fitted using the northern system phase as given by equation (A4a), while the second of these figures (bottom row of panels) shows the same data least squares fitted using the southern system phase as given by equation (A4b). Results for ψ_N in the range 180° to 360° are equivalent to those shown here, except for a change of sign in each of the data values. The fit values are as indicated in each panel, with fit uncertainties estimated using the same jackknife procedure as in section 4. The sinusoid fits (dashed lines) obtained using the northern phase in Figures A1a, A1c, and A1e are essentially perfect as might be expected, with $\overline{B}_N \approx 0$, $B_{N0} \approx 1$, and $\Delta_N \approx 0°$, despite the nonuniform sampling of the field values in northern system phase. As also expected, the same data plotted versus the southern phase in Figures A1b, A1d, and A1f simply appears scattered. However, variable finite amplitudes are obtained on fitting equation (A4b) to these data, though in all cases consistent with zero as indicated by the estimated uncertainties. Overall, it is found that ~10% of the northern amplitude appears spuriously in the southern phase fits, within a typical range ~0%–20%

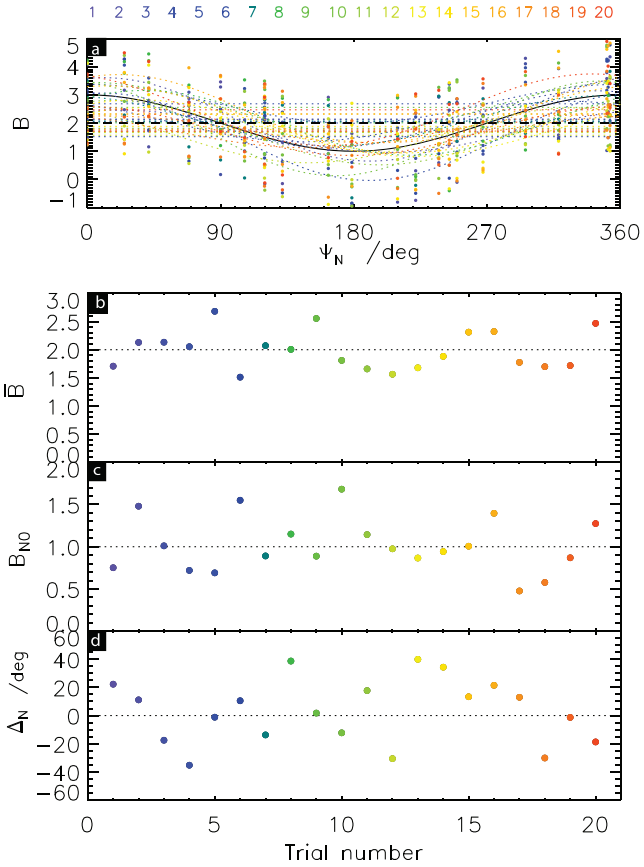

Figure B1. Plots showing results for the calculation discussed in Appendix B designed to investigate the effect of a significant random noise field on the sinusoid fits to azimuthal field data in the intra-D ring field line region. The noise concerned consists of the field perturbations associated with the interhemispheric current system flowing on these field lines, estimated typically to have a peak magnitude (~20 nT) 4 times the amplitude of the PPO oscillations (~5 nT). The results of 20 "trials" using differing sets of random numbers in equation (B1) are shown, color-coded as shown at the top of the figure, with $B_N = 1$, $\psi_N = 0°$, and $R_{max} = 4$. Figure B1 shows the model sinusoid $B_N\cos(\Psi_N)$ plotted versus phase Ψ_N (black solid line), varying about the expected mean $R_{max}/2 = 2$ (black dashed line), together with the 20 sinusoids fitted to data with random noise added, shown by the color-coded dashed lines. Figures B1b–B1d show the corresponding fit parameters in equation (B2), namely, the mean value $\overline{B}_N$, the amplitude B_{N0}, and the phase deviation Δ_N, respectively, again color-coded by trial number.

depending on phase ψ_N, consistent with the estimated uncertainties. Entirely similar results are obtained for the spurious amplitude of the northern system when instead we take $B_S = 1$ and $B_N = 0$ in equation (A3).

In Figure A2 we show results for dual modulated data in a similar format to Figure A1 (though with an increased range on the ordinate), where we take $B_N = B_S = 1$ in equation (A3), together with $\psi_S = 0°$ and a range of values of ψ_N values as marked in each panel of the figure. As expected, the data now exhibit significant scatter about overall sinusoidal modulations when plotted versus both northern as well as southern phases. In conformity with the above results, however, the variability in the amplitude of all the fits is typically ~±10% about the known values of unity, within a typical range ~0%–20% depending on the relative phase given by ψ_N. The associated phase deviations $\Delta_{N,S}$ are typically ~10° or less.

Appendix B: Effect of Intra-D Ring Region Noise on Azimuthal Field Sinusoid Fits

A singular property of the proximal pass PPO results is the enhancement in azimuthal component amplitudes combined with variations in phase found on and inside of D ring field lines in both the northern and southern system results shown in Figures 10 and 11, respectively. Amplitudes rise across D ring field lines from ~3–5 nT on main ring field lines to peak at ~7.5 nT at the highest ionospheric colatitudes reached inside of the D ring, while phase deviations are found to vary by up to ~90°. The uncertainties in these sinusoidal fits are also notably enhanced in this region, as can also be seen in Figures 10 and 11 (see also Figures 6 and 7). A significant contribution to the enhanced scatter in this region is evidently the presence of the "intra-D ring" azimuthal magnetic field perturbations believed due to quasi-static interhemispheric current flow (Dougherty et al., 2018; Khurana et al., 2018), which are found to be highly variable in form from pass to pass in a manner uncorrelated with the PPO phases (Provan, Cowley, et al., 2019). These azimuthal field perturbations are usually positive in sign, to a first approximation symmetrical about the field-parallel point, and variable in amplitude between a few nT and ~20 nT. Their peak magnitude is thus significantly larger than that of the quasi-sinusoidal PPO azimuthal component variations generally present on the ring field lines. The question therefore arises as to whether the presence of these large essentially randomly varying perturbations can systematically affect the sinusoidal fit results shown in Figures 10 and 11, both with regard to amplitude and phase. It is evident that given increasing "noise" magnitudes, the sinusoid fits will eventually become swamped by the effects of the superposed variations, giving enhanced amplitudes related to the noise with essentially random phases. Here we investigate whether such effects could account for the enhanced D ring amplitudes shown in Figures 10 and 11.

In order to simulate these effects as they apply to the proximal pass data, we use a formulation related to that in Appendix A and take a pass-to-pass model field given by

$$B_n = B_N\cos\left(\frac{360(t_n - t_1)}{\tau_N} - (\varphi_n - \varphi_1) - \psi_N\right) + R_n(R_{max}), \quad \text{(B1)}$$

where t_n and φ_n are specifically the time and azimuth of the field-parallel points of the proximal passes, with $n = 1$ corresponding to Rev 271 and $n = 22$ to Rev 292. We use the northern system period τ_N for definiteness, and without loss of generality set $B_N = 1$ and $\psi_N = 0°$ as baseline values. The R_n values are obtained from a

random number generator in the range $0 \le R_n \le R_{max}$, thus with a mean value $\overline{R}_n \approx R_{max}/2$. Given a typical ring region azimuthal component amplitude of ~5 nT, and a typical maximum intra-D ring perturbation field of ~20 nT with a consequent averaged perturbation field of ~10 nT as in Figure 18c, we thus choose $R_{max} = 4$ in equation (B1), a factor of four larger than the model amplitude $B_N = 1$. We then least squares fit the resulting data set using the function

$$B_N = \overline{B}_N + B_{N0}\cos\left(\frac{360(t-t_1)}{\tau_N} - (\varphi-\varphi_1) - \psi_N - \Delta_N\right), \quad \text{(B2)}$$

to examine the variation of $\overline{B}_N$ about the expected mean value of $R_{max}/2 = 2$, the variation of the fitted amplitude B_{N0} about $B_N = 1$, and the variation of the fitted phase Δ_N about $\psi_N = 0°$. The process is then repeated using a number of random data sets in order to gauge the typical range of variation.

Results are shown in Figure B1 using twenty sets of random numbers. The black solid line in Figure B1a shows the baseline sinusoid $B_N\cos(\Psi_N)$ with $B_N = 1$ plotted versus phase Ψ_N, oscillating about the expected mean value $R_{max}/2 = 2$ shown by the dashed back line, together with the twenty fitted values shown as color-coded dashed lines. The panels beneath, Figures B1b–B1d, show the three fit parameters in equation (B2), namely the mean value $\overline{B}_N$, the amplitude B_{N0}, and the phase deviation Δ_N, respectively, shown color-coded by trial number as in Figure B1a. The mean value in Figure B1b scatters about a value of 2 as expected, with an overall mean and standard deviation with this particular data set of 1.98 ± 0.34. The amplitude in Figure B1c similarly scatters about the true amplitude of unity, with a mean and standard deviation of 0.99 ± 0.34. These results therefore show that under proximal orbit conditions the additional noise in the azimuthal component data at the levels experienced on intra-D ring field lines does not generally produce an elevation in the deduced PPO amplitudes of the magnitude observed in Figures 10 and 11. The phase deviation in Figure B1d scatters about zero with a circular mean and standard deviation of $2.0° \pm 24.1°$. Phase deviations of such magnitude may contribute somewhat to the intra-D ring phase deviations in the azimuthal component evident in Figures 10 and 11, but appear insufficient to account for the larger of the phase deviations determined.

Acknowledgments
Work at the University of Leicester and Imperial College London was supported by STFC consolidated grants ST/N000749/1 and ST/N000692/1, respectively. E.J.B. was supported by a Royal Society Wolfson Research Merit Award and M.K.D. by a Royal Society Research Professorship. T.J.B. was supported by STFC Quota Studentship ST/N504117/1. We thank Steve Kellock and the Cassini magnetometer team at Imperial College for the access to processed magnetic field data. Calibrated magnetic field data from the Cassini mission are available from the NASA Planetary Data System at the Jet Propulsion Laboratory (https://pds.jpl.nasa.gov/).

References

Andrews, D. J., Bunce, E. J., Cowley, S. W. H., Dougherty, M. K., Provan, G., & Southwood, D. J. (2008). Planetary period oscillations in Saturn's magnetosphere: Phase relation of equatorial magnetic field oscillations and SKR modulation. *Journal of Geophysical Research*, *113*, A09205. https://doi.org/10.1029/2007JA012937

Andrews, D. J., Cecconi, B., Cowley, S. W. H., Dougherty, M. K., Lamy, L., Provan, G., & Zarka, P. (2011). Planetary period oscillations in Saturn's magnetosphere: Evidence in magnetic field phase data for rotational modulation of Saturn kilometric radiation emissions. *Journal of Geophysical Research*, *116*, A09206. https://doi.org/10.1029/2011JA016636

Andrews, D. J., Coates, A. J., Cowley, S. W. H., Dougherty, M. K., Lamy, L., Provan, G., & Zarka, P. (2010). Magnetospheric period oscillations at Saturn: Comparison of equatorial and high-latitude magnetic field periods with north and south SKR periods. *Journal of Geophysical Research*, *115*(A12), A12252. https://doi.org/10.1029/2010JA015666

Andrews, D. J., Cowley, S. W. H., Dougherty, M. K., Lamy, L., Provan, G., & Southwood, D. J. (2012). Planetary period oscillations in Saturn's magnetosphere: Evolution of magnetic oscillation properties from southern summer to post-equinox. *Journal of Geophysical Research*, *117*, A04224. https://doi.org/10.1029/2011JA017444

Andrews, D. J., Cowley, S. W. H., Dougherty, M. K., & Provan, G. (2010). Magnetic field oscillations near the planetary period in Saturn's equatorial magnetosphere: Variation of amplitude and phase with radial distance and local time. *Journal of Geophysical Research*, *115*, A04212. https://doi.org/10.1029/2007JA014729

Andrews, D. J., Cowley, S. W. H., Provan, G., Hunt, G. J., Hadid, L. Z., Morooka, M. W., & Wahlund, J.-E. (2019). Magnetic field oscillations in Saturn's equatorial magnetosphere: Results from the Cassini mission. *Journal of Geophysical Research: Space Physics*, published https://doi.org/10.1029/2019JA026804

Arridge, C. S., André, N., Khurana, K. K., Russell, C. T., Cowley, S. W. H., Provan, G., et al. (2011). Periodic motion of Saturn's nightside plasma sheet. *Journal of Geophysical Research*, *116*(A11), A11205. https://doi.org/10.1029/2011JA016827

Bader, A., Badman, S. V., Kinrade, J., Cowley, S. W. H., Provan, G., & Pryor, W. R. (2018). Statistical planetary period oscillation signatures in Saturn's UV auroral intensity. *Journal of Geophysical Research: Space Physics*, *123*, 8459–8472. https://doi.org/10.1002/2018JA025855

Bader, A., Badman, S. V., Kinrade, J., Cowley, S. W. H., Provan, G., & Pryor, W. R. (2019). Modulations of Saturn's UV auroral oval location by planetary period oscillations. *Journal of Geophysical Research: Space Physics*, 952–970. https://doi.org/10.1002/2018JA026117

Badman, S. V., Andrews, D. J., Cowley, S. W. H., Lamy, L., Provan, G., Tao, C., et al. (2012). Rotational modulation and local time dependence of Saturn's infrared H_3^+ auroral intensity. *Journal of Geophysical Research*, *117*, A09228. https://doi.org/10.1029/2011JA017990

Bradley, T. J., Cowley, S. W. H., Bunce, E. J., Smith, A. W., Jackman, C. J., & Provan, G. (2018). Planetary period modulation of reconnection bursts in Saturn's magnetotail. *Journal of Geophysical Research: Space Physics*, *123*, 9476–9507. https://doi.org/10.1002/2018JA025426

Bradley, T. J., Cowley, S. W. H., Provan, G., Hunt, G. J., Bunce, E. J., Wharton, S. J., et al. (2018). Field-aligned currents in Saturn's nightside magnetosphere: Subcorotation and planetary period oscillation components during northern spring. *Journal of Geophysical Research: Space Physics*, *123*, 3602–3636. https://doi.org/10.1002/2017JA024885

Bunce, E. J., Arridge, C. S., Clarke, J. T., Coates, A. J., Cowley, S. W. H., Dougherty, M. K., et al. (2008). Origins of Saturn's aurora: Simultaneous observations by Cassini and the Hubble Space Telescope. *Journal of Geophysical Research*, *113*, A09209. https://doi.org/10.1029/2008JA013257

Bunce, E. J., Cowley, S. W. H., Alexeev, I. I., Arridge, C. S., Dougherty, M. K., Nichols, J. D., & Russell, C. T. (2007). Cassini observations of the variation of Saturn's ring current parameters with system size. *Journal of Geophysical Research*, *112*, A10202. https://doi.org/10.1029/2007JA012275

Burton, M. E., Dougherty, M. K., & Russell, C. T. (2010). Saturn's internal planetary magnetic field. *Geophysical Research Letters*, *37*, L24105. https://doi.org/10.1029/2010GL045148

Carbary, J. F. (2012). The morphology of Saturn's ultraviolet aurora. *Journal of Geophysical Research*, *117*, A06210. https://doi.org/10.1029/2012JA017670

Carbary, J. F. (2017). Update on Saturn's energetic electron periodicities. *Journal of Geophysical Research: Space Physics*, *122*, 156–165. https://doi.org/10.1002/2016JA023405

Carbary, J. F., Mitchell, D. G., Brandt, P. C., Krimigis, S. M., & Gurnett, D. A. (2011). ENA periodicities and their phase relations to SKR emissions at Saturn. *Geophysical Research Letters*, *38*, L16106. https://doi.org/10.1029/2011GL048418

Chancia, R. O., Hedman, M. M., Cowley, S. W. H., Provan, G., & Ye, S.-Y. (2019). Seasonal structures in Saturn's dusty Roche Division are tied to periodicities in the planet's magnetosphere. *Icarus*, *330*, 230–255. https://doi.org/10.1016/j.icarus.2019.04.012

Clarke, K. E., Andrews, D. J., Arridge, C. S., Coates, A. J., & Cowley, S. W. H. (2010). Magnetopause oscillations near the planetary period at Saturn: Occurrence, phase, and amplitude. *Journal of Geophysical Research*, *115*, A08209. https://doi.org/10.1029/2009JA014745

Clarke, K. E., Andrews, D. J., Coates, A. J., Cowley, S. W. H., & Masters, A. (2010). Magnetospheric period oscillations of Saturn's bow shock. *Journal of Geophysical Research*, *115*, A05202. https://doi.org/10.1029/2009JA015164

Cowley, S. W. H., & Provan, G. (2015). Planetary period oscillations in Saturn's magnetosphere: Comments on the relation between post-equinox periods determined from magnetic field and SKR emission data. *Annales Geophysicae*, *33*, 901–912. https://doi.org/10.5194/angeo-33-901-2015

Cowley, S. W. H., & Provan, G. (2016). Planetary period oscillations in Saturn's magnetosphere: Further comments on the relationship between post-equinox properties deduced from magnetic field and Saturn kilometric radiation measurements. *Icarus*, *272*, 258–276. https://doi.org/10.1016/j.icarus.2016.02.051

Cowley, S. W. H., & Provan, G. (2017). Planetary period modulations of Saturn's magnetotail current sheet during northern spring: Observations and modeling. *Journal of Geophysical Research: Space Physics*, *122*, 6049–6077. https://doi.org/10.1002/2017JA023993

Dougherty, M. K., Achilleos, N., Andre, N., Arridge, C. S., Balogh, A., Bertucci, C., et al. (2005). Cassini Magnetometer Observations During Saturn Orbit Insertion. *Science*, *307*, 1266–1270. https://doi.org/10.1126/science.1106098

Dougherty, M. K., Cao, H., Khurana, K. K., Hunt, G. J., Provan, G., Kellock, S., et al. (2018). Saturn's ssini's Grand Finale. *Science*, *362*, eaat5434. https://doi.org/10.1126/science.aat5434

Espinosa, S. A., & Dougherty, M. K. (2000). Periodic perturbations in Saturn's magnetic field. *Geophysical Research Letters*, *27*(17), 2785–2788. https://doi.org/10.1029/2000GL000048

Fischer, G., Gurnett, D. A., Kurth, W. S., Ye, S.-Y., & Groene, J. B. (2015). Saturn kilometric radiation periodicity after equinox. *Icarus*, *254*, 72–91. https://doi.org/10.1016/j.icarus.2015.03.014

Galand, M., Moore, L., Mueller-Wodarg, I., Mendillo, M., & Miller, S. (2011). Response of Saturn's auroral ionosphere to electron precipitation: Electron density, electron temperature, and electrical conductivity. *Journal of Geophysical Research*, *116*, A09306. https://doi.org/10.1029/2010JA016412

Galopeau, P. H. M., & Lecacheux, A. (2000). Variations of Saturn's radio rotation period measured at kilometer wavelengths. *Journal of Geophysical Research*, *105*(A6), 13,089–13,101. https://doi.org/10.1029/1999JA005089

Gurnett, D. A., Groene, J. B., Averkamp, T. F., Kurth, W. S., Ye, S.-Y., & Fischer, G. (2011). The SLS4 longitude system based on a tracking filter analysis of the rotational modulation of Saturn kilometric radiation. In H. O. Rucker, W. S. Kurth, P. Louarn, & G. Fischer (Eds.), *Planetary Radio Emissions VII*, (pp. 51–64). Vienna: Austrian Acad. Sci. Press.

Gurnett, D. A., Groene, J. B., Persoon, A. M., Menietti, J. D., Ye, S.-Y., Kurth, W. S., et al. (2010). The reversal of the rotational modulation rates of the north and south components of Saturn kilometric radiation near equinox. *Geophysical Research Letters*, *37*, L24101. https://doi.org/10.1029/2010GL045796

Gurnett, D. A., Lecacheux, A., Kurth, W. S., Persoon, A. M., Groene, J. B., Lamy, L., et al. (2009). Discovery of a north-south asymmetry in Saturn's radio rotation period. *Geophysical Research Letters*, *36*, L16102. https://doi.org/10.1029/2009GL039621

Gurnett, D. A., Persoon, A. M., Groene, J. B., Kopf, A. J., Hospodarsky, G. B., & Kurth, W. S. (2009). A north-south difference in the rotation rate of auroral hiss at Saturn: Comparison to Saturn's kilometric radio emission. *Geophysical Research Letters*, *36*, L21108. https://doi.org/10.1029/2009GL040774

Hadid, L. Z., Morooka, M. W., Wahlund, J.-E., Moore, L., Cravens, T. E., Hedman, M. M., et al. (2018). Ring shadowing effects on Saturn's ionosphere: Implications for ring opacity and plasma transport. *Geophysical Research Letters*, *45*, 10,084–10,092. https://doi.org/10.1029/2018GL079150

Hedman, M. M., Burns, J. A., Tiscareno, M. S., & Porco, C. C. (2009). Organizing some very tenuous things: Resonant structures in Saturn's faint rings. *Icarus*, *202*, 260–279. https://doi.org/10.1016/j.icarus.2009.02.016

Hunt, G. J., Cowley, S. W. H., Provan, G., Bunce, E. J., Alexeev, I. I., Belenkaya, E. S., et al. (2014). Field-aligned currents in Saturn's southern nightside magnetosphere: Sub-corotation and planetary period oscillation components. *Journal of Geophysical Research: Space Physics*, *119*, 9847–9899. https://doi.org/10.1002/2014JA020506

Hunt, G. J., Cowley, S. W. H., Provan, G., Bunce, E. J., Alexeev, I. I., Belenkaya, E. S., et al. (2015). Field-aligned currents in Saturn's northern nightside magnetosphere: Evidence for inter-hemispheric current flow associated with planetary period oscillations. *Journal of Geophysical Research: Space Physics*, *120*, 7552–7584. https://doi.org/10.1002/2015JA021454

Hunt, G. J., Cowley, S. W. H., Provan, G., Bunce, E. J., Alexeev, I. I., Belenkaya, E. S., et al. (2016). Field-aligned currents in Saturn's magnetosphere: Local time dependence of southern summer currents in the dawn sector between midnight and noon. *Journal of Geophysical Research: Space Physics*, *121*, 7785–7804. https://doi.org/10.1002/2016JA022712

Hunt, G. J., Provan, G., Bunce, E. J., Cowley, S. W. H., Dougherty, M. K., & Southwood, D. J. (2018). Field-aligned currents in Saturn's magnetosphere: Observations from the F-ring orbits. *Journal of Geophysical Research: Space Physics*, *123*, 3806–3821. https://doi.org/10.1002/2017JA025067

Hunt, G. J., Provan, G., Cowley, S. W. H., Dougherty, M. K., & Southwood, D. J. (2018). Planetary period oscillations during the closest approach of Cassini's ring grazing orbits. *Geophysical Research Letters*, *45*, 4692–4700. https://doi.org/10.1002/2018GL077925

Jackman, C. M., Provan, G., & Cowley, S. W. H. (2016). Reconnection events in Saturn's magnetotail: Dependence of plasmoid occurrence on planetary period oscillation phase. *Journal of Geophysical Research: Space Physics*, *121*, 2922–2934. https://doi.org/10.1002/2015JA021985

Jinks, S. L., Bunce, E. J., Cowley, S. W. H., Provan, G., Yeoman, T. K., Arridge, C. S., et al. (2014). Cassini multi-instrument assessment of Saturn's polar cap boundary. *Journal of Geophysical Research: Space Physics*, *119*, 8161–8177. https://doi.org/10.1002/2014JA020367

Khurana, K. K., Dougherty, M. K., Provan, G., Hunt, G. J., Kivelson, M. G., Cowley, S. W. H., et al. (2018). Discovery of atmospheric-wind-driven electric currents in Saturn's magnetosphere in the gap between Saturn and its rings. *Geophysical Research Letters*, *45*, 10,068–10,074. https://doi.org/10.1002/2018GL078256

Kurth, W. S., Averkamp, T. F., Gurnett, D. A., Groene, J. B., & Lecacheux, A. (2008). An update to a Saturnian longitude system based on kilometric radio emissions. *Journal of Geophysical Research*, *113*, A05222. https://doi.org/10.1029/2007JA012861

Lamy, L. (2011). Variability of southern and northern SKR periodicities. In H. O. Rucker, W. S. Kurth, P. Louarn, & G. Fischer (Eds.), *Planetary Radio Emissions VII*, (pp. 39–50). Vienna: Austrian Acad. Sci. Press.

Lamy, L. (2017). The Saturnian kilometric radiation before the Cassini Grand Finale. In G. Fischer, G. Mann, M. Panchenko, & P. Zarka (Eds.), *Planetary Radio Emissions VIII*, (pp. 171–190). Vienna: Austrian Academy of Science Press.

Lamy, L., Prangé, R., Pryor, W., Gustin, J., Badman, S. V., Melin, H., et al. (2013). Multispectral diagnosis of Saturn's aurorae throughout a planetary rotation. *Journal of Geophysical Research: Space Physics*, *118*, 4817–4843. https://doi.org/10.1002/jgra.50404

Mardia, K. V., & Jupp, P. E. (2000). *Directional Statistics*. Chichester (UK): J. Wiley and Sons Ltd.

Mitchell, C. J., Porco, C. C., Dones, H. L., & Spitale, J. N. (2013). The behavior of spokes in Saturn's B ring. *Icarus*, *225*, 446–474. https://doi.org/10.1016/j.icarus.2013.02.011

Nichols, J. D., Cecconi, B., Clarke, J. T., Cowley, S. W. H., Gérard, J.-C., Grocott, A., et al. (2010). Variation of Saturn's UV aurora with SKR phase. *Geophysical Research Letters*, *37*, L15102. https://doi.org/10.1029/2010GL044057

Nichols, J. D., Cowley, S. W. H., & Lamy, L. (2010). Dawn-dusk oscillation of Saturn's conjugate auroral ovals. *Geophysical Research Letters*, *37*, L24102. https://doi.org/10.1029/2010GL045818

Porco, C. C., & Danielson, G. E. (1982). The periodic variation of spokes in Saturn's rings. *The Astronomical Journal*, *87*, 826–833. https://doi.org/10.1086/113162

Provan, G., Andrews, D. J., Arridge, C. S., Coates, A. J., Cowley, S. W. H., Cox, G., et al. (2012). Dual periodicities in planetary-period magnetic field oscillations in Saturn's tail. *Journal of Geophysical Research*, *117*, A01209. https://doi.org/10.1029/2011JA017104

Provan, G., Andrews, D. J., Arridge, C. S., Cowley, S. W. H., Milan, S. E., Dougherty, M. K., & Wright, D. M. (2009). Polarization and phase of planetary period oscillations on high latitude field lines in Saturn's magnetosphere. *Journal of Geophysical Research*, *114*, A02225. https://doi.org/10.1029/2008JA013782

Provan, G., Andrews, D. J., Cecconi, B., Cowley, S. W. H., Dougherty, M. K., Lamy, L., & Zarka, P. (2011). Magnetospheric period magnetic field oscillations at Saturn: Equatorial phase 'jitter' produced by superposition of southern- and northern-period oscillations. *Journal of Geophysical Research*, *116*, A04225. https://doi.org/10.1029/2010JA016213

Provan, G., Cowley, S. W. H., Bradley, T. J., Bunce, E. J., Hunt, G. J., & Dougherty, M. K. (2018). Planetary period oscillations in Saturn's magnetosphere: Cassini magnetic field observations over the northern summer solstice interval. *Journal of Geophysical Research: Space Physics*, *123*, 3859–3899. https://doi.org/10.1002/2018JA025237

Provan, G., Cowley, S. W. H., Bunce, E. J., Bradley, T. J., Hunt, G. J., Cao, H., & Dougherty, M. K. (2019). Variability of intra-D ring azimuthal magnetic field profiles observed on Cassini's proximal periapsis passes. *Journal of Geophysical Research: Space Physics*, *124*, 379–404. https://doi.org/10.1002/2018JA026121

Provan, G., Cowley, S. W. H., Lamy, L., Bunce, E. J., Hunt, G. J., Zarka, P., & Dougherty, M. K. (2016). Planetary period oscillations in Saturn's magnetosphere: Coalescence and reversal of northern and southern periods in late northern spring. *Journal of Geophysical Research: Space Physics*, *121*, 9829–9862. https://doi.org/10.1002/2016JA023056

Provan, G., Cowley, S. W. H., Sandhu, J., Andrews, D. J., & Dougherty, M. K. (2013). Planetary period magnetic field oscillations in Saturn's magnetosphere: Post-equinox abrupt non-monotonic transitions to northern system dominance. *Journal of Geophysical Research: Space Physics*, *118*, 3243–3264. https://doi.org/10.1002/jgra.50186

Provan, G., Lamy, L., Cowley, S. W. H., & Bunce, E. J. (2019). Planetary period oscillations in Saturn's magnetosphere: Comparison of magnetic and SKR modulation periods and phases during northern summer to the end of the Cassini mission. *Journal of Geophysical Research: Space Physics*, *124*, 1157–1172. https://doi.org/10.1002/2018JA026079

Provan, G., Lamy, L., Cowley, S. W. H., & Dougherty, M. K. (2014). Planetary period oscillations in Saturn's magnetosphere: Comparison of magnetic oscillations and SKR modulations in the post-equinox interval. *Journal of Geophysical Research: Space Physics*, *119*, 7380–7401. https://doi.org/10.1002/2014JA020011

Ramer, K. M., Kivelson, M. G., Sergis, N., Khurana, K. K., & Jia, X. (2017). Spinning, breathing, and flapping: Periodicities in Saturn's middle magnetosphere. *Journal of Geophysical Research: Space Physics*, *122*, 393–416. https://doi.org/10.1002/2016JA023126

Southwood, D. J., & Kivelson, M. G. (2007). Saturn magnetospheric dynamics: Elucidation of a camshaft model. *Journal of Geophysical Research*, *112*, A12222. https://doi.org/10.1029/2007JA012254

Thomsen, M. F., Jackman, C. M., Cowley, S. W. H., Jia, X., Kivelson, M. G., & Provan, G. (2017). Evidence for periodic variations in the thickness of Saturn's nightside plasma sheet. *Journal of Geophysical Research: Space Physics*, *122*, 280–292. https://doi.org/10.1002/2016JA023368

Wolter, K. M. (2007). *Introduction to Variance Estimation*. New York: Springer. https://doi.org/10.1007/978-0-387-35099-8

Xin, L., Gurnett, D. A., Santolik, O., Kurth, W. S., & Hospodarsky, G. B. (2006). Whistler mode auroral hiss emissions observed near Saturn's B ring. *Journal of Geophysical Research*, *111*, A06214. https://doi.org/10.1029/2005JA011432

Ye, S.-Y., Fischer, G., Kurth, W. S., Menietti, J. D., & Gurnett, D. A. (2016). Rotational modulation of Saturn's radio emissions after equinox. *Journal of Geophysical Research: Space Physics*, *121*, 11,714–11,728. https://doi.org/10.1002/2016JA023281

Ye, S.-Y., Gurnett, D. A., Groene, J. B., Wang, Z., & Kurth, W. S. (2010). Dual periodicities in the rotational modulation of Saturn narrowband emissions. *Journal of Geophysical Research*, *115*, A12258. https://doi.org/10.1029/2010JA015780